

Chemical abundances of the Damped Lyman Alpha systems in the XQ-100 survey

T. A. M. Berg¹, S. L. Ellison¹, R. Sánchez-Ramírez^{2,3,4}, J. X. Prochaska⁵, S. Lopez⁶, V. D’Odorico⁷, G. Becker^{8,9}, L. Christensen¹⁰, G. Cupani⁷, K. Denney¹¹, G. Worseck¹²

¹ Department of Physics and Astronomy, University of Victoria, Victoria, British Columbia, V8P 1A1, Canada.

² Unidad Asociada Grupo Ciencias Planetarias (UPV/EHU, IAA-CSIC), Departamento de Física Aplicada I, E.T.S. Ingeniería, Universidad del País Vasco (UPV/EHU), Alameda de Urquijo s/n, E-48013 Bilbao, Spain.

³ Ikerbasque, Basque Foundation for Science, Alameda de Urquijo 36-5, E-48008 Bilbao, Spain.

⁴ Instituto de Astrofísica de Andalucía (IAA-CSIC), Glorieta de la Astronomía s/n, E-18008, Granada, Spain.

⁵ Department of Astronomy and Astrophysics, University of California, Santa Cruz, Santa Cruz, CA, 95064, USA. ⁶ Departamento de Astronomía, Un

⁷ INAF-Osservatorio Astronomico di Trieste, Via Tiepolo 11, I-34143 Trieste, Italy.

⁸ Space Telescope Science Institute, 3700 San Martin Drive, Baltimore, MD 21218, USA.

⁹ Institute of Astronomy and Kavli Institute of Cosmology, Madingley Road, Cambridge CB3 0HA, UK.

¹⁰ Dark Cosmology Centre, Niels Bohr Institute, University of Copenhagen, Juliane Maries Vej 30, DK-2100 Copenhagen, Denmark.

¹¹ Department of Astronomy, The Ohio State University, 140 West 18th Avenue, Columbus, OH 43210, USA.

¹² Max-Planck-Institut für Astronomie, Königstuhl 17, D-69117 Heidelberg, Germany.

11 October 2018

ABSTRACT

The XQ-100 survey has provided high signal-noise spectra of 100 redshift 3–4.5 quasars with the X-Shooter spectrograph. The metal abundances for 13 elements in the 41 damped Ly α systems (DLAs) identified in the XQ-100 sample are presented, and an investigation into abundances of a variety of DLA classes is conducted. The XQ-100 DLA sample contains five DLAs within 5000 km s $^{-1}$ of their host quasar (proximate DLAs; PDLAs) as well as three sightlines which contain two DLAs within 10,000 km s $^{-1}$ of each other along the same line-of-sight (multiple DLAs; MDLAs). Combined with previous observations in the literature, we demonstrate that PDLAs with $\log N(\text{HI}) < 21.0$ show lower [S/H] and [Fe/H] (relative to intervening systems with similar redshift and N(HI)), whilst higher [S/H] and [Si/H] are seen in PDLAs with $\log N(\text{HI}) > 21.0$. These abundance discrepancies are independent of their line-of-sight velocity separation from the host quasar, and the velocity width of the metal lines (v_{90}). Contrary to previous studies, MDLAs show no difference in [α /Fe] relative to single DLAs matched in metallicity and redshift. In addition, we present follow-up UVES data of J0034+1639, a sightline containing three DLAs, including a metal-poor DLA with [Fe/H] = −2.82 (the third lowest [Fe/H] in DLAs identified to date) at $z_{\text{abs}} = 4.25$. Lastly we study the dust-corrected [Zn/Fe], emphasizing that near-IR coverage of X-Shooter provides unprecedented access to MgII, CaII and TiII lines (at redshifts 3–4) to provide additional evidence for subsolar [Zn/Fe] ratio in DLAs.

Key words: galaxies: abundances – galaxies: high redshift – galaxies: ISM – quasars: absorption lines

1 INTRODUCTION

Quasars (QSOs) exist at many different epochs, providing lines of sight through pockets of gas from the epoch of reionization to the present day. One of the classes of intervening absorbers towards QSOs are damped Lyman- α systems (DLAs; Wolfe et al. 2005), defined by their large H I column

densities ($N(\text{HI}) \geq 2 \times 10^{20}$ atoms cm $^{-2}$; Wolfe et al. 1986). DLAs are common probes to study the evolution of neutral gas and metals in the interstellar medium (ISM) of galaxies from $z_{\text{abs}} \sim 5$ to the present day (Wolfe et al. 1995; Pettini et al. 1997; Prochaska & Herbert-Fort 2004; Rao et al. 2006; Rafelski et al. 2014; Sánchez-Ramírez et al. 2016).

2 Berg et al.

A large portion of DLA analyses has been concentrated on detailed abundance analyses of the host galaxies (e.g. Pettini et al. 1994; Lu et al. 1998; Centurión et al. 2000; Wolfe et al. 2003; Cooke et al. 2011; Zafar et al. 2014a; Berg et al. 2015a). As elements have unique physical properties and nucleosynthetic origins (Woosley & Weaver 1995; McWilliam 1997; Nomoto et al. 2013), different abundance ratios have been used to understand the star formation history and dust content of DLAs (Ledoux et al. 2002; Prochaska & Wolfe 2002; Vladilo et al. 2011). The most common ratio to probe enrichment histories is $[\alpha/\text{Fe}]$, which traces the star formation history due to the time-delayed contributions of Type II and Ia supernovae (Tinsley 1979; McWilliam 1997; Venn et al. 2004; Tolstoy et al. 2009). However elements such as Fe, Ni, and Cr are heavily depleted onto dust (Savage & Sembach 1996), leading to overestimates of the measured gas-phase $[\alpha/\text{Fe}]$ in DLAs. These overestimates in $[\alpha/\text{Fe}]$ have led to the use of other undepleted elements that trace Fe (such as Zn) to better estimate the intrinsic $[\alpha/\text{Fe}]$ ratio (Pettini et al. 1997; Vladilo 2002b). In the case of Zn, care must be taken as Zn does not necessarily trace Fe in all environments and metallicities (Prochaska et al. 2000; Chen et al. 2004; Nissen et al. 2007; Rafelski et al. 2012; Berg et al. 2015a).

The physical nature of DLAs also influences their gas phase abundances, including the role of ionizing sources (D'Odorico 2007; Ellison et al. 2010; Zafar et al. 2014b) or the amount of dust (e.g. Pettini et al. 1994; Kulkarni et al. 1997; Akerman et al. 2005; Krogager et al. 2016). There are many sub-classes of DLAs that provide opportunities to probe these differing physical environments. Proximate DLAs (PDLAs) are DLAs defined to be within $\Delta v \leq 5000 \text{ km s}^{-1}$ of the host QSO, and more frequently seen than intervening systems (Ellison et al. 2002; Russell et al. 2006; Prochaska et al. 2008b). PDLAs have shown increasing metal abundances with increasing N(HI) , in particular both $[\text{S/H}]$ and $[\text{Si/H}]$ are $\sim 3\times$ larger in four PDLAs with $\log\text{N(HI)} > 21.0$ (Ellison et al. 2010, 2011). Multiple DLAs (MDLAs) along the same line of sight within $500 \leq \Delta v \leq 10000 \text{ km s}^{-1}$ of each other have also shown different metallicity effects, with a low $[\alpha/\text{Fe}]$ relative to the typical DLA (Ellison & Lopez 2001; Lopez & Ellison 2003); an effect attributed to truncated star formation from environmental effects. However, the analyses of Lopez & Ellison (2003) and Ellison et al. (2010) suffer from low numbers of MDLAs (seven absorbers) and PDLAs (16 absorbers).

Recently there has been a significant effort to identify the first stars and galaxies (Cayrel et al. 2004; Beers & Christlieb 2005; Suda et al. 2008; Spite et al. 2011; Frebel & Bromm 2012; Norris et al. 2013; Frebel & Norris 2015) to constrain Population III nucleosynthesis (Umeda & Nomoto 2002; Greif et al. 2007; Heger & Woosley 2010; Cooke et al. 2013). In tandem with the search for metal-poor stars in the Galaxy and its nearby companions (e.g. Jacobson et al. 2015; Skúladóttir et al. 2015), work at higher redshifts focused the identification and measurement of abundances in the most metal-poor DLAs (MPDLAs; $[\text{Fe}/\text{H}] \leq -2.5$; Penprase et al. 2010; Cooke et al. 2011; Becker et al. 2012; Cooke & Madau 2014). As the explosion mechanism of the supernovae models is very uncertain, chemical abundances in these metal-poor regimes are required to constrain the models of Population III nucleosynthesis. In particular the supernovae ex-

plosion energy influences the mass cut of the supernovae, and thus which elements escape into the ISM (Umeda & Nomoto 2002; Nomoto et al. 2013). To date, abundances in the most MPDLAs reflect first generation stars that have undergone moderate to low energy core-collapse supernovae (Cooke et al. 2011, 2013), but remains to be tested for a large sample of DLAs with $[\text{Fe}/\text{H}] \leq -3$.

The XQ-100 Large Programme survey (PI: S. Lopez, ESO ID 189.A-0424; López et al. 2016) has observed 100 QSOs at $z = 3.5\text{--}4.5$ with the X-Shooter (Vernet et al. 2011) spectrograph on the Very Large Telescope (VLT). As the survey was primarily designed to study active galactic nuclei, the inter-galactic medium, and the Ly α forest; XQ-100 provides a near-random sample of intervening DLAs as the QSOs were selected without consideration of intervening absorbers. In this paper, we present the metal column densities for 14 species (O_{I} , C_{II} , Mg_{I} , Mg_{II} , Ca_{II} , S_{III} , P_{II} , S_{II} , T_{II} , Cr_{II} , Mn_{II} , Fe_{II} , Ni_{II} , Zn_{II}) in the DLAs recently identified by Sánchez-Ramírez et al. (2016) in the XQ-100 survey. By combining the XQ-100 DLAs with a sample of DLA abundances in the literature (Berg et al. 2015a), we investigate the elemental abundances of the XQ-100 sample and demonstrate the prospects of using X-Shooter to study absorption lines in the near infrared (NIR).

2 DATA

In this section we present the DLA abundances derived in this work. The spectra used come from the XQ-100 survey (López et al. 2016), as well as follow-up observations with VLT/UVES for one sightline (J0034+1639).

2.1 XQ-100 abundances

The XQ-100 dataset consists of 100 QSOs observed with X-Shooter towards QSO sightlines at redshift $z_{\text{em}} \sim 3.5\text{--}4.5$. The per-arm exposures were either ~ 0.5 or ~ 1 hour in length (depending whether the QSO was classified as ‘bright’ or ‘faint’; respectively), providing signal-noise ratios (snr) of $\sim 20 \text{ pixel}^{-1}$ (median $\sim 30 \text{ pixel}^{-1}$) at resolution $R \sim 5000\text{--}9000$ from the near UV (3150Å) to the NIR (25000 Å). The spectra were reduced using an internal IDL package. For more details, see López et al. (2016).

The DLAs were identified and HI column densities determined in Sánchez-Ramírez et al. (2016). Table 1 summarizes the DLAs identified in the XQ-100 survey, along with their redshifts¹, $\log\text{N(HI)}$ and line-of-sight velocity separations from the QSO (Δv). In Sánchez-Ramírez et al. (2016), the HI column densities were determined by simultaneously fitting the Lyman series (up to Ly ϵ). Redshifts were primarily determined from the HI fits, but in some cases were guided by the metal lines.

The XQ-100 spectra are released with two options for continuum fits. One option uses a power-law with select emission lines incorporated to fit each spectrum, providing

¹ For J0034+1639, the redshifts of the DLAs have been tweaked based on the metal lines in the UVES spectra presented in Section 2.2.

Table 1. XQ-100 DLA sample

QSO	z_{em}	z_{abs}	$\log N(\text{H}\alpha)$	Δv (km s $^{-1}$)
J0003–2603	4.125	3.390	21.40 ± 0.10	46040
J0006–6208	4.440	3.203	20.90 ± 0.15	75670
		3.775	21.00 ± 0.20	38870
J0034+1639	4.292	3.752	20.40 ± 0.15	32110
		4.251	20.60 ± 0.10	2349 ^{PM}
		4.283	21.00 ± 0.10	522 ^{PM}
J0113–2803	4.314	3.106	21.20 ± 0.10	75650
J0124+0044	3.837	2.261	20.70 ± 0.15	112400
J0132+1341	4.152	3.936	20.40 ± 0.15	12830
J0134+0400	4.185	3.692	20.70 ± 0.10	29850 ^M
		3.772	20.70 ± 0.10	24800 ^M
J0234–1806	4.305	3.693	20.40 ± 0.15	36570
J0255+0048	4.003	3.256	20.90 ± 0.10	48100
		3.914	21.50 ± 0.10	5350
J0307–4945	4.716	3.591	20.50 ± 0.15	64680
		4.466	20.60 ± 0.10	13370
J0415–4357	4.073	3.808	20.50 ± 0.20	16070
J0424–2209	4.329	2.982	21.40 ± 0.15	84930
J0529–3552	4.172	3.684	20.40 ± 0.15	29620
J0747+2739	4.133	3.424	20.90 ± 0.10	44270
		3.901	20.60 ± 0.15	13860
J0800+1920	3.948	3.946	20.40 ± 0.10	91 ^P
J0818+0958	3.656	3.306	21.00 ± 0.10	23380
J0835+0650	4.007	3.955	20.40 ± 0.10	3099 ^P
J0920+0725	3.646	2.238	20.90 ± 0.15	103800
J0955–0130	4.418	4.024	20.70 ± 0.15	22560
J1020+0922	3.640	2.592	21.50 ± 0.10	75120
J1024+1819	3.524	2.298	21.30 ± 0.10	91730
J1057+1910	4.128	3.373	20.30 ± 0.10	47310
J1058+1245	4.341	3.432	20.60 ± 0.10	55320
J1108+1209	3.679	3.397	20.70 ± 0.10	18650
		3.546	20.80 ± 0.15	8643
J1312+0841	3.731	2.660	20.50 ± 0.10	75300
J1421–0643	3.688	3.449	20.30 ± 0.15	15670
J1517+0511	3.555	2.688	21.40 ± 0.10	62340
J1552+1005	3.722	3.601	21.10 ± 0.10	7781 ^M
		3.667	20.70 ± 0.10	3544 ^{PM}
J1633+1411	4.365	2.882	20.30 ± 0.15	93750
J1723+2243	4.531	3.698	20.50 ± 0.10	48510
J2239–0552	4.557	4.080	20.60 ± 0.10	26800
J2344+0342	4.248	3.220	21.30 ± 0.10	64340

^P – Proximate DLA^M – Multiple DLA

complete wavelength coverage. However this power-law continuum does not provide a good fit around missing QSO emission lines, and therefore cannot be used for accurate DLA abundances in some cases. In this paper we use the alternative option, a by-hand fit to the continuum using a cubic spline², similar to the approach of Sánchez-Ramírez et al. (2016). The error spectra were normalized by the same continuum fit.

Metal Column Densities

Column densities were derived using the Apparent Optical Depth Method (AODM) presented in Savage & Sembach (1991). In brief, this method sums the optical depth of an

unsaturated absorption feature (at wavelength λ with oscillator strength f ; taken from Morton 2003), converting the total optical depth into a column density using

$$N = \frac{m_e c}{\pi e^2 f \lambda} \int_{v_{\min}}^{v_{\max}} \tau dv. \quad (1)$$

The integration limits v_{\min} and v_{\max} are selected such that the associated metal absorption profile are bounded by these velocity limits. We attempted to use the same velocity limits for all metal lines for a given DLA, however the velocity limits were sometimes adjusted on a line-by-line basis to exclude regions of contamination outside the metal absorption feature. If the weaker components of a shallow line are undetected, the velocity limits are purposefully made narrow to only contain associated absorption, and exclude flux contribution from the continuum. When the column density is derived using multiple clean lines for the same ion, we adopt the average value ($\log N_{\text{adopt}}$) and the standard error (with a minimum error of 0.05 dex). For features that exhibited obvious blending or saturation, we measure the AODM column density as a limit to the true value, adopting the most constraining limit as the final value. For cases where the absorption feature is severely blended, we do not consider adopting the measured column density.

The limiting spectral resolution of X-Shooter (R=5100, 8800, and 5300 for the UV, visible, and NIR arms; respectively) implies that there are cases where we cannot determine the presence of unseen contamination or saturation visually. Cases of hidden contamination or saturation were flagged when multiple lines are measured for a given species and resulted in significantly inconsistent column densities. Using multiple SiII and FeII lines, we have noted that these cases of hidden saturation tend to occur when the strongest absorption reaches a relative flux of ~ 0.3 –0.5 (similar to the ~ 0.25 seen in the UVB arm by Krogager et al. 2016). Lines with absorption stronger than ~ 0.5 (in units of relative flux) were inspected for inconsistent column densities with other lines. Unless the derived column density is consistent with weaker lines, any discrepant column densities were flagged as saturated. We note that all of the lines with a peak absorption at ~ 0.5 had additional lines to constrain potential saturation. However, there may still be cases with unresolved saturation or blending unaccounted for.

When weak lines are not detected and the spectrum is uncontaminated, we measure 3σ upper limits based on the ability to detect the strongest absorption feature within the signal-noise ratio of the spectrum using

$$N = \frac{3m_e c \text{ FWHM}}{\pi e^2 f \lambda^2 (1 + z_{\text{abs}}) \text{ snr}} \quad (2)$$

where FWHM is the full-width at half-maximum of the strongest absorption feature. As the components of the absorption profile are likely limited by the resolution of the instrument ($\Delta v \sim 55$ km s $^{-1}$) rather than the DLA kinematics ($\Delta v \sim 10$ km s $^{-1}$; e.g. Dessauges-Zavadsky et al. 2004; Jorgenson et al. 2010; Tumlinson et al. 2010; Cooke & Madau 2014), we assume that the FWHM of this strongest absorption feature to be equal to the resolution limit of X-Shooter in the setup with a slit width of $\sim 1''$. The signal-noise ratio for the 3σ upper-limits was computed within the bounds of the AODM limits.

² Code available at <https://github.com/trystynb/ContFit>.

Table 2. XQ-100 DLA Column Densities

QSO	z_{abs}	$\log N(\text{H})$	[M/H] (ion)	$\log N(\text{CII})$	$\log N(\text{OI})$	$\log N(\text{MgI})$	$\log N(\text{MgII})$	$\log N(\text{SiII})$	$\log N(\text{PII})$	$\log N(\text{SII})$	$\log N(\text{CaII})$	$\log N(\text{SIII})$	$\log N(\text{TiII})$
J0003–2603	3.390	21.40 ± 0.10	-1.93 ± 0.11 (ZnII)	11.85 ± 0.05	> 13.91	...	< 13.73	...	< 11.81	< 12.2	< 12.38
J0006–6208	3.203	20.90 ± 0.15	-2.20 ± 0.15 (FeII)	< 12.39	13.33 ± 0.05	...	< 14.49	< 12.3
J0006–6208	3.775	21.00 ± 0.20	-0.94 ± 0.20 (ZnII)	> 14.72	> 15.02	...	> 14.01	...	< 13.63	13.71 ± 0.05	< 14.70	13.65 ± 0.05	< 12.3
J0034+1639	4.251	20.40 ± 0.15	-1.89 ± 0.15 (FeII)	> 14.24	14.78 ± 0.05	...	> 13.20	13.71 ± 0.05	< 13.66	14.56 ± 0.05	< 12.3
J0034+1639	4.283	21.00 ± 0.10	-2.10 ± 0.13 (SiII)	> 14.83	> 15.29	12.13 ± 0.05	...	> 14.83	15.60 ± 0.05	< 11.94	13.25 ± 0.05
J0113–2803	3.106	21.20 ± 0.10	-1.11 ± 0.10 (SiII)	12.60 ± 0.05	> 14.42	15.36 ± 0.05	< 11.94	13.25 ± 0.05	< 12.6
J0124+0044	2.261	20.70 ± 0.15	-0.85 ± 0.15 (SiII)	> 14.39	> 14.77	12.50 ± 0.05	> 14.31	13.87 ± 0.05	< 13.98	< 12.3
J0132+1341	3.936	20.40 ± 0.15	-2.04 ± 0.15 (SiII)	> 14.39	> 14.18	< 14.36	< 13.75	< 11.9
J0134+0400	3.682	20.70 ± 0.10	-2.41 ± 0.10 (FeII)	> 15.21	> 13.49	14.38	< 13.94	15.30 ± 0.05	< 12.4
J0134+0400	3.772	20.70 ± 0.10	-0.91 ± 0.10 (SiII)	12.67 ± 0.05	> 14.30	15.38 ± 0.05	< 12.37	14.05 ± 0.05	< 12.37
J0234–1806	3.693	20.40 ± 0.15	-1.31 ± 0.15 (FeII)	> 14.41	15.38 ± 0.05	< 14.05	15.02 ± 0.05	< 14.20	14.73 ± 0.05	< 12.3
J0255+0048	3.256	20.90 ± 0.10	-1.08 ± 0.10 (SiII)	> 14.55	> 14.95	12.21 ± 0.05	> 14.26	14.39 ± 0.05	< 14.03	...	< 12.3
J0255+0048	3.914	21.50 ± 0.10	-1.92 ± 0.10 (SiII)	> 14.55	> 15.13	11.81 ± 0.05	> 14.18	14.39 ± 0.05	< 14.03	...	< 11.9
J0307–4945	3.591	20.50 ± 0.15	-1.48 ± 0.15 (FeII)	> 15.01	> 15.13	11.81 ± 0.05	< 14.20	13.95	< 12.2
J0415–4357	3.808	20.50 ± 0.20	-1.52 ± 0.10 (SiII)	> 14.98	> 15.50	...	> 15.30	13.62	< 12.07
J0424–2209	2.982	21.40 ± 0.15	-0.28 ± 0.20 (ZnII)	> 13.62	13.53 ± 0.05	< 12.7
J0529–3552	3.684	20.40 ± 0.15	-2.38 ± 0.15 (ZnII)	> 14.13	14.08 ± 0.05	< 14.23	14.08 ± 0.05	< 12.3
J0747+2739	3.424	20.90 ± 0.10	-1.58 ± 0.10 (FeII)	< 11.85	< 12.3
J0747+2739	3.901	20.60 ± 0.15	-2.03 ± 0.15 (SiII)	14.31 ± 0.05	> 14.90	...	> 15.06	12.21 ± 0.05	> 14.26	14.04 ± 0.05	< 13.59	< 13.77	< 12.0
J0800+1920	3.946	20.40 ± 0.10	-1.87 ± 0.10 (SiII)	> 14.58	> 14.12	15.00 ± 0.05	< 14.05	15.00 ± 0.05	< 14.05	14.04 ± 0.05	< 11.9
J0818+0958	3.306	21.00 ± 0.10	-1.51 ± 0.10 (SiII)	> 14.88	> 15.02	14.10 ± 0.05	< 12.2
J0835+0650	3.955	20.40 ± 0.10	-1.81 ± 0.10 (SiII)	> 14.68	> 14.93	14.10 ± 0.05	> 14.68	14.26 ± 0.05	< 12.7
J0920+0725	2.238	20.90 ± 0.15	-1.55 ± 0.15 (FeII)	> 15.18	> 14.68	14.26 ± 0.05	< 12.2
J0955–0130	4.024	20.70 ± 0.15	-1.54 ± 0.15 (FeII)	> 14.98	15.36 ± 0.05	< 12.3
J1020+0922	2.592	21.50 ± 0.10	-1.75 ± 0.10 (SiII)	> 14.98	13.88	< 12.6
J1024+1819	2.298	21.30 ± 0.10	-1.45 ± 0.10 (SiII)	> 15.06	14.26 ± 0.05	< 12.3
J1057+1910	3.373	20.30 ± 0.10	-1.25 ± 0.11 (FeII)	> 14.04	14.94 ± 0.05	< 13.77	14.32	< 12.0
J1058+1245	3.432	20.60 ± 0.10	-7.85 ± 0.10 (SiII)	> 14.88	> 14.04	14.26 ± 0.05	< 13.59	14.05	< 12.0
J1108+1209	3.397	20.70 ± 0.10	-2.49 ± 0.10 (FeII)	> 13.98	14.64 ± 0.05	11.94 ± 0.05	< 13.77	14.25	< 12.0
J1108+1209	3.546	20.80 ± 0.15	-1.15 ± 0.15 (SiII)	> 15.06	> 15.46	12.28 ± 0.05	< 11.67	13.82	< 12.0
J1312+0841	2.660	20.50 ± 0.10	-1.50 ± 0.10 (FeII)	> 14.68	> 14.97	...	< 11.72	13.85	< 12.2
J1421–0643	3.449	20.30 ± 0.15	-1.40 ± 0.15 (FeII)	> 14.17	14.85 ± 0.05	< 14.01	14.01	< 12.3
J1517+0611	2.688	21.40 ± 0.10	-2.06 ± 0.10 (SiII)	> 15.12	14.04 ± 0.05	< 14.12	14.50 ± 0.05	< 12.6
J1552+1005	3.601	21.10 ± 0.10	-1.75 ± 0.11 (SiII)	> 14.77	> 15.18	...	> 13.96	13.99	< 12.5
J1552+1005	3.667	20.70 ± 0.10	-1.61 ± 0.10 (FeII)	> 14.87	< 11.60	13.27	< 14.45	14.57	< 11.51
J1633+1411	2.882	20.30 ± 0.15	-1.78 ± 0.15 (FeII)	> 14.57	14.16 ± 0.05	< 12.1
J1723+2243	3.698	20.50 ± 0.10	-1.03 ± 0.10 (FeII)	> 14.80	> 14.18	> 14.85	< 11.6
J2239–0552	4.080	20.60 ± 0.10	-1.95 ± 0.10 (SiII)	12.56 ± 0.05	> 14.18	< 11.78
J2344+0342	3.220	21.30 ± 0.10	-1.70 ± 0.32 (ZnII)	> 14.18	< 11.78

As an example of data quality and coverage, Figure 1 shows the velocity profile for all the observed lines of the DLA in the spectrum of J0003–2603 ($z_{\text{abs}} = 3.39$). The vertical dashed lines show the velocity limits used to integrate the spectrum for the AODM column density determinations. The column densities for all the measured lines for the DLA towards J0003–2603 are given in Table 3. Table 3 displays the wavelength and oscillator strength of the absorption line (Morton 2003), the velocity integration bounds of the absorption feature used (v_{\min} and v_{\max}), the measured column density $\log N(X)$ of the metal line, and whether the derived column density was included for the final computation of the adopted column density ($\log N_{\text{adopt}}$). The adopted $\log N_{\text{adopt}}$ is given for each species in the last row for the species. Appendix A1 contains the velocity profiles (Figures A1–A21) and abundances (Tables A1–A21) for the remaining DLAs. If the adopted column density for a given species is best constrained by an upper and lower limit, the range of possible values is provided in Tables A1–A21. A summary of the final adopted column densities for all DLAs is listed in Table 2³.

v_{90} parameter

Following the analysis techniques described in Prochaska & Wolfe (1997), we have assessed the kinematic characteristics of the XQ-100 DLA sample. In particular, we have measured the velocity width v_{90} corresponding to 90% of the integrated optical depth using one low-ion transition per DLA (listed in Table 4). We selected transitions according to the spectral S/N, avoiding saturated or weak absorption profiles. The optical depth per pixel was calculated from the normalized flux values and then smoothed by a boxcar with width of 22 km s^{-1} as in Prochaska & Wolfe (1997). From these smoothed optical depth arrays, we calculate the velocity width comprising 90% of the integrated optical depth between the AODM integration bounds.

Adopting the results of Prochaska et al. (2008a) who also analysed a set of echelle observations ($R \approx 8,000$), we have reduced the raw v_{90} values to correct for instrumental broadening. Specifically, we lower the raw v_{90} measurements by 30, 17, and 25 km/s for the UVB, VIS, and NIR arms respectively. These corrections correspond to $\approx 40\%$ of the FWHM of the instrumental line-spread-function for our X-Shooter configuration. The final, reported v_{90} values are presented in Table 4.

Comparison to literature measurements

Of the DLAs studied in XQ-100, 15 DLAs have previously been observed in the literature sample of Berg et al. (2015a, further referred to as the literature sample). The literature sample includes abundance determinations for a variety of elements⁴ using high resolution spectrographs (predominantly VLT/UVES, Keck/HIRES, and Keck/ESI) for 341 DLAs between $z_{\text{abs}} \sim 0$ and 5.

³ The adopted column densities in Table 2 for the DLAs towards J0034+1639 are preferentially adopted from the UVES data presented in Section 2.2.

⁴ The elements are: N, O, Mg, Al, Si, S, Ca, Ti, Cr, Mn, Fe, Co, Ni, and Zn.

Table 4. v_{90} measurements for the XQ-100 DLA sample

QSO	z_{abs}	Transition	v_{90} km s^{-1}
J0003–2603	3.390	CrII 2066	32
J0006–6208	3.203	FeII 1608	32
J0006–6208	3.775	FeII 1608	54
J0034+1639	3.755	FeII 2586	32
J0034+1639	4.251	SIII 1526	43
J0034+1639	4.283	FeII 1608	109
J0113–2803	3.106	SIII 1808	219
J0124+0044	2.261	SIII 1808	142
J0132+1341	3.936	FeII 1608	32
J0134+0400	3.692	FeII 1608	10
J0134+0400	3.772	SIII 1808	109
J0234–1806	3.693	FeII 2344	203
J0255+0048	3.256	FeII 1608	208
J0255+0048	3.914	SII 1253	21
J0307–4945	3.591	FeII 2586	51
J0307–4945	4.466	SIII 1304	219
J0415–4357	3.808	SIII 1526	131
J0424–2209	2.982	FeII 2600	13
J0529–3552	3.684	SIII 1526	21
J0747+2739	3.424	FeII 1608	120
J0747+2739	3.901	SIII 1526	153
J0800+1920	3.946	SIII 1304	43
J0818+0958	3.306	SIII 1808	76
J0835+0650	3.955	SIII 1304	21
J0920+0725	2.238	FeII 2374	98
J0955–0130	4.024	FeII 2600	336
J1020+0922	2.592	SIII 1808	76
J1024+1819	2.298	SIII 1808	54
J1057+1910	3.373	FeII 1608	307
J1058+1245	3.432	MgII 2803	127
J1108+1209	3.397	CII 1334	32
J1108+1209	3.546	FeII 2374	70
J1312+0841	2.660	FeII 2344	153
J1421–0643	3.449	FeII 1608	43
J1517+0511	2.688	FeII 1608	43
J1552+1005	3.601	SII 1253	21
J1552+1005	3.667	SIII 1304	230
J1633+1411	2.882	MgII 2803	13
J1723+2243	3.698	FeII 2586	374
J2239–0552	4.080	SIII 1526	131
J2344+0342	3.220	CrII 2056	54

Similar to the comparison of $N(\text{H}\alpha)$ to the literature in Sánchez-Ramírez et al. (2016), Table 5 compares the metal column densities for the 15 DLAs common between the literature and XQ-100. $\Delta N(X)$ represents the difference in column density between the value determined in this work and the value in the literature sample (where a positive difference implies the XQ-100 column density is larger than what is in the literature). When both the literature and XQ-100 measurements yield a clean detection, we compare difference in column densities ($\Delta N(X)_{\text{det.}}$) to the combined column density errors. Consistent values of $\Delta N(X)_{\text{det.}}$ should be of the order of the combined error, although the quoted errors in metal column densities do not generally account for sources of error other than photon noise (e.g. continuum fitting) and can be larger. For most of the detections, we see consistent values between XQ-100 and the high-resolution literature (to within 0.05 dex). The discrepant cases (the

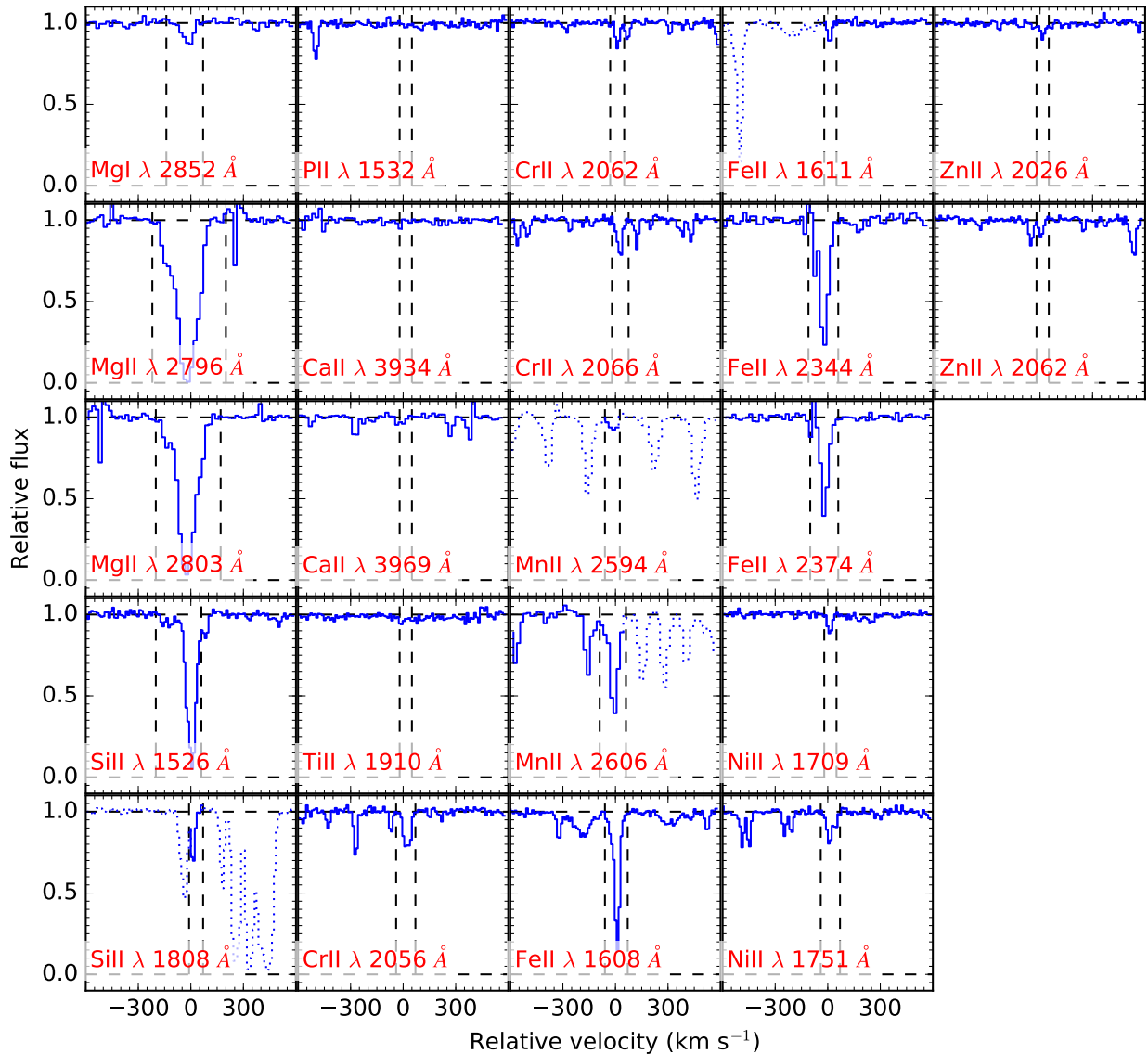


Figure 1. Velocity profile of the XQ-100 spectrum towards J0003-2603 ($z_{\text{abs}}=3.390$). The vertical dashed lines indicated the AODM velocity bounds. Regions of the spectrum that are contaminated by strong, unassociated absorption are flagged as dotted lines.

bolded ionic species in Table 5) are discussed in Appendix B. In all cases, the column densities derived in this work are adopted as they are consistent with the literature values (see Appendix B for justification of discrepant cases).

For cases where both the XQ-100 and literature measurements are upper limits ($\Delta N(X)_{\text{lim.}}$; positive values indicate that the XQ-100 limit is higher than the literature), 4 of 10 XQ-100 upper limits are more constraining than the literature column density derived from Keck/ESI data with comparable resolution. Naturally, the higher-resolution instruments provide more constraining upper limits due to

their ability to resolve narrower features within the fluctuations of the continuum. For all cases where the literature provides better limits (or detections, as in the case for NiII and ZnII in J2344+0342 at $z_{\text{abs}}=3.22$), we adopt the literature values.

Continuum-fitting errors

As a baseline for comparison, the spline continuum-fitting was done two times to assess the random errors of the continuum fit. The median difference in column density for all lines

Table 3. X-Shooter metal column densities for J0003–2603 ($z_{\text{abs}}=3.390$)

Ion	Line	λ Å	f	v_{min} km s $^{-1}$	v_{max} km s $^{-1}$	logN(X)	Included	logN $_{\text{adopt}}$
MgI	2852	2852.964	1.81E+00	-140	70	11.85 ± 0.03	Y	—
MgI								11.85 ± 0.05
MgII	2796	2796.352	6.12E-01	-220	200	> 13.91	Y	—
MgII	2803	2803.531	3.05E-01	-200	170	> 14.04	Y	—
MgII								> 14.04
SiII	1526	1526.707	1.27E-01	-200	60	> 14.37	Y	—
SiII	1808	1808.013	2.19E-03	-10	70	< 14.98	Y	—
SiII								14.36–14.98
PII	1532	1532.533	7.61E-03	-20	50	< 13.73	Y	—
PII								< 13.73
CaII	3934	3934.777	6.50E-01	-20	50	< 11.81	Y	—
CaII	3969	3969.591	3.22E-01	-20	50	< 11.82	N	—
CaII								< 11.81
TiII	1910	1910.750	2.02E-01	-20	50	< 12.24	Y	—
TiII								< 12.24
CrII	2056	2056.254	1.05E-01	-40	70	< 13.34	N	—
CrII	2062	2062.234	7.80E-02	-30	50	13.07 ± 0.04	Y	—
CrII	2066	2066.161	5.15E-02	-20	75	< 13.49	N	—
CrII								13.07 ± 0.05
MnII	2594	2594.499	2.71E-01	-60	25	< 12.39	Y	—
MnII	2606	2606.462	1.93E-01	-90	60	< 13.57	N	—
MnII								< 12.39
FeII	1608	1608.451	5.80E-02	-60	70	> 14.35	N	—
FeII	1611	1611.200	1.36E-03	-20	50	14.75 ± 0.04	Y	—
FeII	2344	2344.214	1.14E-01	-110	60	> 14.02	N	—
FeII	2374	2374.461	3.13E-02	-100	60	> 14.34	N	—
FeII								14.75 ± 0.05
NiII	1709	1709.604	3.24E-02	-20	50	13.42 ± 0.04	Y	—
NiII	1751	1751.916	2.77E-02	-40	70	< 13.88	N	—
NiII								13.42 ± 0.05
ZnII	2026	2026.136	4.89E-01	-20	50	12.10 ± 0.05	Y	—
ZnII	2062	2062.664	2.56E-01	-20	50	< 12.35	N	—
ZnII								12.10 ± 0.05

in the two iterations is 0.0 dex, with an interquartile range of 0.02 dex and 67% of column densities being within ± 0.01 dex. Although the 3σ upper limits are not included in this calculation, it is worth noting that derived column densities for these limits are sensitive to the continuum placement.

2.2 UVES data for J0034+1639

The X-Shooter spectrum of the $z_{\text{abs}}=4.25$ DLA (Figure A4) towards J0034+1639 suggests a very low metallicity system ($[\text{Fe}/\text{H}]=-2.82 \pm 0.11$, third lowest $[\text{Fe}/\text{H}]$ to date; Cooke et al. 2015, see Table A5). The sightline also contains two other DLAs, as well as a number of other H I absorbers (which will be discussed in a future paper).

To confirm the column densities of this metal-poor DLA are free of undetected contamination and saturation, as well as attempting to measure Fe-peak elements such as NiII to pinpoint the underlying supernovae population (Cooke et al.

2013), we obtained VLT/UVES (Dekker et al. 2000) data towards the sightline J0034+1639. The observing programme (PI: T. Berg; Programme number 094.A-0223A) was organized in five observing blocks (OBs) of 48 min each for a total of 4 hours of on-target integration to obtain a signal-noise of $20\text{--}25$ pixel $^{-1}$. We used the dichroic DIC-2 at the standard setting of 437+760 to obtain wavelength coverage between 6000Å and 9000Å (slit width 0.8''; $R \sim 80000$). The data were reduced using the standard UVES data-reduction software in REFLEX⁵. After correcting for the heliocentric velocity, the five OBs were median combined with IRAF's SCOMBINE, whilst the error spectra were combined in quadrature. The combined spectrum was then continuum normalized using the cubic spline software presented in Section 2.1.

Metal column densities for the three DLAs along the sightline (see Table 1) were derived using the AODM, as

⁵ <http://www.eso.org/sci/software/reflex/>

Table 5. N(X) comparison between XQ-100 and literature

QSO sightline	z_{abs}	Ion	$\log N(X)_{\text{XQ100}}$	$\log N(X)_{\text{Lit.}}$	$\Delta N(X)_{\text{det.}}$	$\Delta N(X)_{\text{lim.}}$	Lit. Instrument(s)	Ref.
J0003-2603	3.390	CriI	13.07 ± 0.05	13.09 ± 0.03	-0.02 ± 0.06	–	UVES,HIRES	1,2
	–	FeII	14.75 ± 0.05	14.87 ± 0.03	-0.12 ± 0.06	–	UVES,HIRES	1,2
	–	NiIII	13.42 ± 0.05	13.39 ± 0.03	$+0.03 \pm 0.06$	–	UVES,HIRES	1,2
	–	ZnIII	12.10 ± 0.05	12.01 ± 0.05	$+0.09 \pm 0.07$	–	UVES,HIRES	1,2
J0134+0400	3.692	SiiI	< 14.36	> 14.26	–	–	ESI,UVES	3,4
	–	FeII	13.44 ± 0.05	13.51 ± 0.07	-0.07 ± 0.09	–	ESI,UVES	3,4
J0134+0400	3.772	SiIII	15.30 ± 0.05	15.46 ± 0.02	-0.16 ± 0.05	–	ESI,UVES	3,5
	–	CriI	< 12.83	< 13.24	–	-0.41	ESI,UVES	3,5
	–	FeII	14.97 ± 0.05	> 14.87	–	–	ESI,UVES	3,5
	–	NiIII	13.84 ± 0.05	13.98 ± 0.03	-0.14 ± 0.06	–	ESI,UVES	3,5
	–	ZnIII	12.88 ± 0.05	< 13.10	–	–	ESI,UVES	3,5
J0255+0048	3.256	SiiI	15.33 ± 0.05	15.32 ± 0.04	$+0.01 \pm 0.06$	–	HIRES	2
	–	FeII	> 14.75	14.76 ± 0.01	–	–	HIRES	2
	–	NiIII	< 13.44	13.61 ± 0.07	–	–	HIRES	2
J0255+0048	3.914	SiiI	15.02 ± 0.05	> 14.19	–	–	HIRES	2
	–	SiiI	14.73 ± 0.05	14.72 ± 0.01	0.01 ± 0.05	–	HIRES	2
	–	NiIII	13.50 ± 0.05	13.27 ± 0.04	$+0.23 \pm 0.06$	–	HIRES	2
J0307-4945	4.466	SiiI	14.59 ± 0.05	14.68 ± 0.07	-0.09 ± 0.09	–	UVES	6
	–	FeII	14.11 ± 0.05	14.21 ± 0.17	-0.10 ± 0.18	–	UVES	6
	–	NiIII	< 13.43	< 12.60	–	0.83	UVES	6
J0424-2209	2.982	CriI	< 13.01	< 12.90	–	$+0.11$	ESI	3
	–	NiIII	< 13.47	< 13.37	–	0.10	ESI	3
	–	ZnIII	< 12.28	< 12.17	–	0.11	ESI	3
J0747+2739	3.424	FeII	14.47 ± 0.05	> 14.43	–	–	ESI	3
	–	NiIII	< 13.46	< 13.27	–	0.19	ESI	3
J0747+2739	3.901	SiiI	14.08 ± 0.05	14.03 ± 0.01	$+0.05 \pm 0.05$	–	ESI	3
	–	FeII	14.03 ± 0.05	< 13.80	–	–	ESI	3
	–	NiIII	< 13.45	< 13.11	–	0.34	ESI	3
J0955-0130	4.024	FeII	14.31 ± 0.05	14.19 ± 0.08	$+0.12 \pm 0.09$	–	HIRES,ESI	2,7,8
	–	NiIII	< 13.41	< 13.44	–	-0.03	HIRES,ESI	2,7,8
J1108+1209	3.397	SiiI	< 13.77	> 13.63	–	–	ESI	9
	–	FeII	13.36 ± 0.05	< 13.72	–	–	ESI	9
J1421-0643	3.449	CriI	< 12.84	< 12.71	–	0.13	UVES	5,10
	–	FeII	14.05 ± 0.05	14.14 ± 0.02	-0.09 ± 0.05	–	UVES	5,10
	–	ZnIII	< 13.25	< 11.98	–	1.19	UVES	5,10
J1723+2243	3.698	FeII	14.62 ± 0.05	> 14.57	–	–	ESI	3
	–	NiIII	< 13.63	< 13.95	–	-0.32	ESI	3
J2239-0552	4.080	FeII	14.00 ± 0.05	13.88 ± 0.12	$+0.12 \pm 0.13$	–	HIRES,ESI,UVES	8,11,12
	–	NiIII	< 13.02	< 13.17	–	-0.15	HIRES,ESI,UVES	8,11,12
J2344+0342	3.220	CriI	13.38 ± 0.05	13.34 ± 0.10	$+0.04 \pm 0.11$	–	UVES,ESI	3,13
	–	NiIII	< 13.58	13.59 ± 0.11	–	–	UVES,ESI	3,13
	–	ZnIII	< 12.85	12.23 ± 0.30	–	–	UVES,ESI	3,13

Bolded species indicate cases of column density discrepancies between XQ-100 and the literature, and are discussed in Section B.

$\Delta N(X)$ is positive when the XQ-100 column density is larger than the literature value.

REFERENCES – (1) Molaro et al. (2000). (2) Prochaska et al. (2001). (3) Prochaska et al. (2003). (4) Petitjean et al. (2008). (5) Noterdaeme et al. (2008). (6) Dessauges-Zavadsky et al. (2001). (7) Prochaska & Wolfe (2000). (8) Songaila & Cowie (2002). (9) Penprase et al. (2010). (10) Akerman et al. (2005). (11) Lu et al. (1996). (12) Henry & Prochaska (2007). (13) Dessauges-Zavadsky et al. (unpublished).

in Section 2.1. As UVES can resolve down to the kinematic structure of the DLA clouds, we use the measured FWHM of the strongest component of an unsaturated metal line profile as the minimum equivalent width observable. This FWHM is used in Equation 2 to determine the 3σ limits in the absorber. The signal-noise ratio for the 3σ upper-limits was computed within the bounds of the AODM limits. Figure 2 and Table 6 present the velocity profiles of the absorption lines towards the MPDLA and the corresponding column densities. The data for the other absorbers are presented in the same format in Appendix A2.

In general, we preferentially adopt the UVES column density as the higher resolution provides an accurate determination of the absorption profile and the data has a similar or higher signal-noise ratio. The one exception where we adopt the XQ-100 value is due to a lack of strong, uncontaminated FeII lines covered in the UVES spectrum required to derive an accurate column density. We note that the absorption in the NIII 1741 Å panel of Figure 2 is likely contaminated as it does not produce a consistent measurement with the derived column density limits for the NIII 1709Å and 1751Å lines.

2.3 XQ-100 sample properties

To briefly highlight the properties of the 41 DLAs observed in the XQ-100 survey, Figures 3 and 4 show the $\log N(HI)$ and metallicity-redshift distribution (respectively) of the XQ-100 sample relative to the DLA literature sample compiled in Berg et al. (2015a). The metallicities ([M/H]; see Table 2) were derived following a similar scheme outlined in Rafelski et al. (2012), where they choose (in order of decreasing preference) S, Si, Zn, and Fe as the metallicity tracer. They add a +0.3 dex correction to Fe to account for the difference in observed $[\alpha/Fe]$. We adopt the Asplund et al. (2009) solar scale for all metallicity calculations. The $\log N(HI)$ distribution shows no significant deviation from what is probed by the literature DLAs; a Kolmogorov-Smirnov (KS) test of the two distributions rejects the null hypothesis at 99.2% confidence.

Figure 4 shows the metallicity distribution of the XQ-100 sample (solid red line; top panel) and the metallicity distribution as a function of redshift (bottom panel). Figure 4 emphasizes that the XQ-100 DLAs are predominantly between redshifts $z_{abs}=3-4.5$, and as a result appear more metal-poor than the literature (which includes the lower redshift and thus higher metallicity DLAs; Rafelski et al. 2012). A KS test rejects the null hypothesis that the metallicity distributions of the literature and XQ-100 DLA samples are drawn from the same distribution at 0.3% confidence. However, when both the literature and XQ-100 samples are restricted to $z_{abs}=3-4.5$, the KS test rejects the null hypothesis at 90.6% confidence.

Using the measured z_{abs} and v_{90} for the XQ-100 DLAs, we compared the derived metallicities from the $[M/H]-z_{abs}-v_{90}$ relation in Neeleman et al. (2013) to our directly-measured [M/H]. We find good agreement between the two metallicities (mean difference of 0.02 dex), with a root-mean-squared scatter between the two metallicities (0.32 dex) that is consistent with the scatter observed in Neeleman et al. (2013, 0.37 dex).

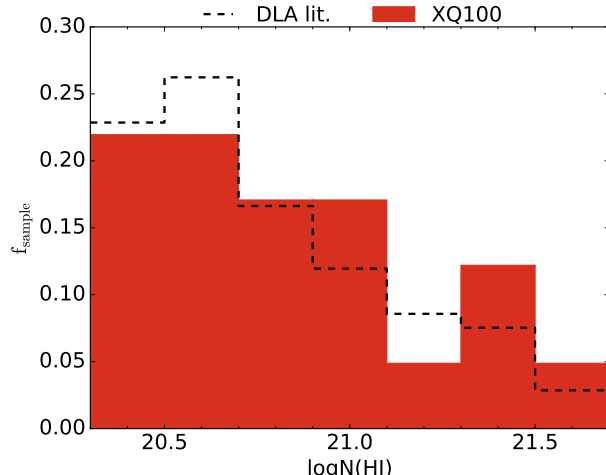


Figure 3. The normalized $\log N(HI)$ distribution of the XQ-100 (red bars) and literature DLA (Berg et al. 2015a, black dashed line) samples.

3 DISCUSSION

3.1 The metal-poor DLA towards J0034+1639

Within the XQ-100 sample, we identified a MPDLA candidate towards J0034+1639 ($z_{abs}=4.2507$), for which we followed up with higher resolution observations with VLT/UVES to confirm the derived metal column densities are free from contamination (see Section 2.2 for details on observations). The column densities for this MPDLA are presented in Table 6. It is interesting to note that, although the $[Fe/H]$ abundance (-2.82 ± 0.11) is the third lowest observed to date in a DLA (Cooke et al. 2015, and references therein), its metallicity using the Rafelski et al. (2012) scheme is much higher ($[M/H]=-2.40 \pm 0.11$; 23rd lowest).

Table 7 shows the abundances for the metal-poor DLA towards J0034+1639, compared to the mean abundance derived from the metal-poor DLAs ($\langle[X/O]_{MPDLA}\rangle$) from the MPDLA sample in Cooke et al. (2011). The abundance ratios (relative to O) of C, Si, and Fe are consistent⁶ with the typical MPDLA abundance pattern (although we note that $[Si/O]$ is almost 0.2 dex larger than the typical MPDLA measurement), implying consistency with yields from low-energy supernovae (Heger & Woosley 2010; Cooke et al. 2011). Unfortunately, we are unable to place strong constraints on Ni and other Fe-peak abundances ($[Ni/Fe]<1.26$), which Cooke et al. (2013, and references therein) have demonstrated to be a key discriminator of the supernovae energy.

3.2 Multiple DLAs

Previous work by Lopez & Ellison (2003) on three MDLA systems found a slight deficit of $[\alpha/Fe]$ relative to the typically observed DLA. They suggested that the low $[\alpha/Fe]$

⁶ We suspect the $[C/O]$ ratio is likely consistent with the typical MPDLA values, as the CII absorption is mildly saturated (see Figure 2).

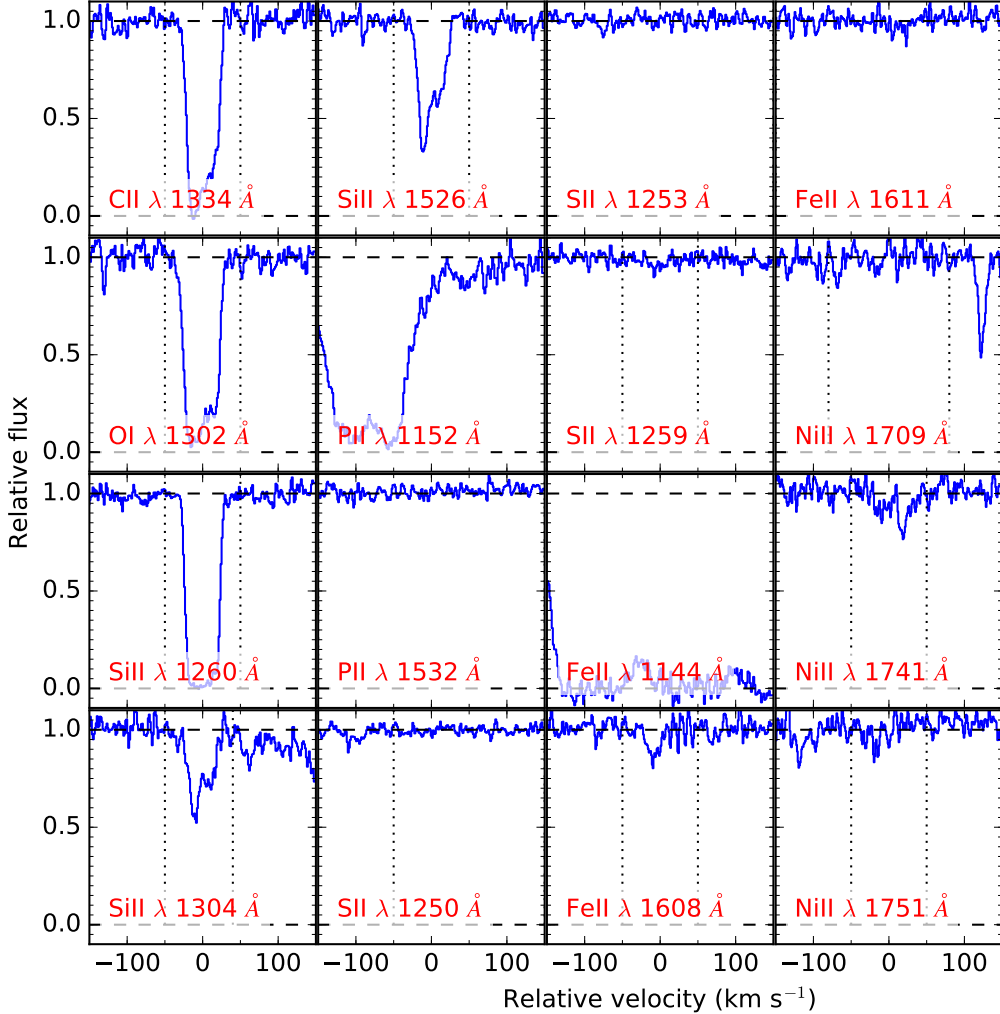


Figure 2. Velocity profiles of the UVES spectrum towards J0034+1639 ($z_{\text{abs}} = 4.25$). Vertical dashed lines represent the velocity limits of the AODM integration.

Table 7. J0034+1639 MPDLA ($z_{\text{abs}} = 4.25$) abundances

Element	[X/H]	[X/O]	$\langle [\text{X}/\text{O}]_{\text{MPDLA}} \rangle^1$
O	-2.51 ± 0.12	—	—
C	> -2.79	> -0.28	-0.28 ± 0.12
Si	-2.40 ± 0.11	0.11 ± 0.16	-0.08 ± 0.10
Fe	-2.82 ± 0.11	-0.31 ± 0.16	-0.39 ± 0.12

¹Mean MPDLA abundance from Cooke et al. (2011).

is due to environmental effects truncating star formation. With the large increase in DLA abundance measurements over the past decade, the robustness of these results can be tested. Following Lopez & Ellison (2003), we identified MDLAs in the XQ-100 and in the Berg et al. (2015a) literature DLA samples as systems of two or more absorbers

within $500 \text{ km s}^{-1} \leq \Delta v \leq 10,000 \text{ km s}^{-1}$ of each other. 6 and 21 MDLAs from the XQ-100 and the literature samples (respectively) were identified (Table 1). Using the measured $[\alpha/\text{Fe}]$ from literature and XQ-100 DLAs, we tested the potential enhancement by comparing each MDLA galaxy with a control-matched sample of intervening DLAs from the literature sample. The control matching technique accounts for the intrinsic evolution of similar DLAs, allowing a comparative test of different environments.

The control matching was completed for each MDLA by selecting all DLAs within the pool of literature DLAs with a redshifts and metallicity identical to the MDLA, within a prescribed tolerance. We impose that the DLA control pool are not classified as MDLAs or PDLAs ($\Delta v < 5000 \text{ km s}^{-1}$). The matching tolerance for metallicity was set by the error in the MDLA's metallicity. The matching tolerance for

Table 6. UVES metal column densities for J0034+1639 ($z_{\text{abs}}=4.251$)

Ion	Line	λ Å	f	v_{min} km s $^{-1}$	v_{max} km s $^{-1}$	logN(X)	Included	logN _{adopt}
CII	1334	1334.532	1.28E-01	-50	50	> 14.24	Y	–
CII								> 14.24
OI	1302	1302.168	4.89E-02	-50	50	14.78 ± 0.02	Y	–
OI								14.78 ± 0.05
SiII	1260	1260.422	1.01E+00	-50	50	> 13.68	N	–
SiII	1304	1304.370	9.40E-02	-50	40	13.71 ± 0.02	Y	–
SiII	1526	1526.707	1.27E-01	-50	50	13.71 ± 0.01	Y	–
SiII								13.71 ± 0.05
PII	1532	1532.533	7.61E-03	-80	80	< 13.66	Y	–
PII								< 13.66
SII	1250	1250.584	5.43E-03	-80	80	< 13.79	N	–
SII	1253	1253.811	1.09E-02	-80	80	< 13.64	N	–
SII	1259	1259.519	1.66E-02	-80	80	13.65 ± 0.08	Y	–
SII								13.65 ± 0.08
FeII	1608	1608.451	5.80E-02	-50	50	13.23 ± 0.06	Y	–
FeII	1611	1611.200	1.36E-03	-80	80	< 14.56	N	–
FeII								13.23 ± 0.06
NiII	1709	1709.604	3.24E-02	-80	80	< 13.33	N	–
NiII	1741	1741.553	4.27E-02	-50	50	< 13.48	N	–
NiII	1751	1751.916	2.77E-02	-50	50	< 13.24	Y	–
NiII								< 13.24

redshift was adopted based on the known redshift evolution of mean metallicity ($[M/H] \propto -0.2 z_{\text{abs}}$; Pettini et al. 1997; Rafelski et al. 2012, 2014). The error in metallicity provides a relative spread in redshifts for a DLA to have undergone a similar metal-enrichment history. Using the slope of the redshift-metallicity evolution, we calculate the redshift tolerance (δz_{abs}) using $\delta z_{\text{abs}} = \frac{\delta[M/H]}{0.2}$, where $\delta[M/H]$ is the error in the metallicity of the MDLA.

To ensure a representative control-matched sample, we required that each MDLA had at least five matched control DLAs. Each of the matched control DLAs must have at least five detections of both Si and Fe to compute $[\alpha/\text{Fe}]$. If these criteria were not met within the initial tolerances, the size of the two matching criteria are repeatedly increased in small increments until a sufficient number of control matched DLAs were obtained. The metallicity bin grew by ± 0.025 dex increments (15–25% of the typical error in metallicity), while the redshift criteria grew by ± 0.125 ($\sim 20\%$ of the associated error due to metallicity evolution). However, expansions were stopped after 10 iterations to ensure that the control-matched sample still resembles the MDLA, effectively matching within $\sim 3\sigma$ of z_{abs} and $[M/\text{H}]$. These criteria result in controls samples being identified for all MDLAs, with only three MDLAs requiring more than two expansions. The median number of matched control DLAs is 14 per MDLA, with 25% of MDLAs having 19 or more (up to 37) control DLAs matched.

The left panel of Figure 5 shows the relative change of $[\alpha/\text{Fe}]$ ($\Delta[\alpha/\text{Fe}]$) in MDLAs compared to their control-matched counterparts, as a function of $N(\text{H})$. $\Delta[\alpha/\text{Fe}]$ is computed as the difference in $[\text{Si}/\text{Fe}]$ between the MDLA absorber and median $[\text{Si}/\text{Fe}]$ of the control-matched DLAs,

such that a positive $\Delta[\alpha/\text{Fe}]$ implies that the MDLA has a higher $[\alpha/\text{Fe}]$ than its control sample. Note that, although all MDLAs are matched, only 14 of the 27 MDLAs have measured $\Delta[\alpha/\text{Fe}]$ due to lack of Si and Fe column densities. Although Fe is depleted onto dust, the relative comparison of $[\alpha/\text{Fe}]$ of MDLAs and control DLAs at a fixed metallicity should remove the effects of dust depletion, as the depletion of refractory elements appears to scale with metallicity in DLAs (e.g. Pettini et al. 1997; Ledoux et al. 2002; Prochaska & Wolfe 2002; Berg et al. 2015a). For reference, the MDLAs from Lopez & Ellison (2003) are shown as large squares, and are included in the analysis. The grey points are the measured $\Delta[\alpha/\text{Fe}]$ from repeating the matching procedure on all control DLAs. The errors on the MDLA points were derived from the spread in the $[\alpha/\text{Fe}]$ of the control sample using the jackknife technique;

$$\sigma_{\text{jack}} = \sqrt{\sum_{i=1}^N \left(\frac{N-1}{N} (\text{med}(N) - \text{med}(N-1))^2 \right)} \quad (3)$$

where N is the number of DLAs, $\text{med}(N)$ is the median of the entire sample, and $\text{med}(N-1)$ is the median of the sample with the i^{th} DLA removed. The colour of the MDLA points indicates the velocity separation of the MDLAs from their counterpart (Table 1). The median $\Delta[\alpha/\text{Fe}]$ (and σ_{jack}) for the MDLAs and control sample are 0.06 ± 0.01 dex and -0.01 ± 0.00^7 dex (respectively).

The right panel of Figure 5 shows the distribution of

⁷ σ_{jack} is much smaller than 0.01 dex, and is thus quoted to be 0 dex.

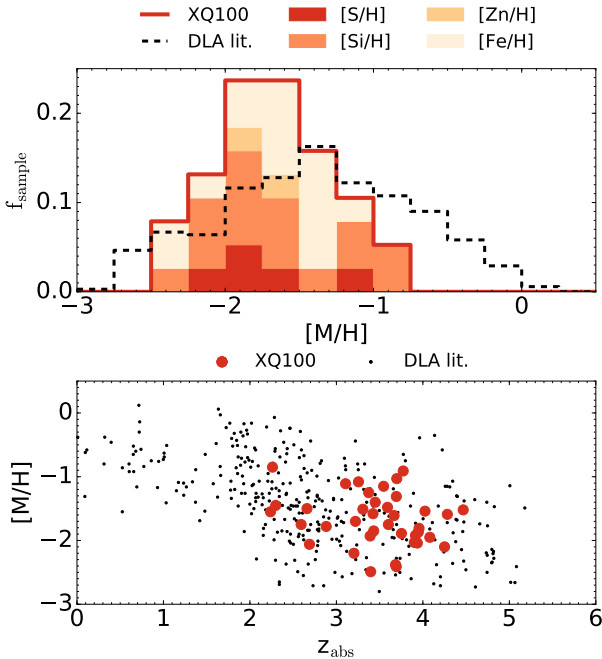


Figure 4. *Top Panel:* The metallicity distribution of the XQ-100 DLAs. The solid red line outlines the total metallicity distribution of the XQ-100 sample, whereas the shaded regions within each bin show the distribution of elements used as the metallicity indicator for the DLAs. The metallicity distribution of the literature DLA sample is shown by the black dashed line. *Bottom Panel:* The distribution of the XQ-100 (red circles) and literature DLAs (black points) in metallicity-redshift space.

$\Delta[\alpha/\text{Fe}]$ for both the MDLA and control samples. The p-value from the Anderson-Darling (AD) test (p_{AD})⁸ rejects the null hypothesis that the two samples are drawn from the same parent sample at $\sim 31\%$ confidence, suggesting MDLAs likely do not show any deficit (or enhancement) in $[\alpha/\text{Fe}]$ relative to the typical DLA.

We note that the Berg et al. (2015a) literature sample includes surveys that have purposefully observed DLAs of specific properties and may have a biased representation of these properties, such as high or low metallicity. As a test of robustness of these results, we limited the control-matched samples to DLAs from the relatively unbiased Rafelski et al. (2012) literature sample, and re-computed $\Delta[\alpha/\text{Fe}]$. Only 6 of the 27 MDLAs were matched, and still showed no deficit in $[\alpha/\text{Fe}]$ ($p_{\text{AD}} \sim 0.86$).

We note that the upper velocity limit of MDLAs defined in Lopez & Ellison (2003, 10000 km s^{-1}) is much larger than the typical galaxy cluster velocity dispersion (values are typically smaller than 2000 km s^{-1} ; Ruel et al. 2014). Reducing the definition of an MDLA to a separation of 2000 km s^{-1} limits the sample to one MDLA system, which shows a $\Delta[\alpha/\text{Fe}]$ of $\sim +0.2 \text{ dex}$. Unfortunately more MDLAs are required to further test if a smaller velocity separation does have an impact on the MDLA abundances.

⁸ We preferentially use the AD test over a KS test as the AD test is independent of the shape of the distribution, and is more sensitive to discrepancies in the tails of the distribution.

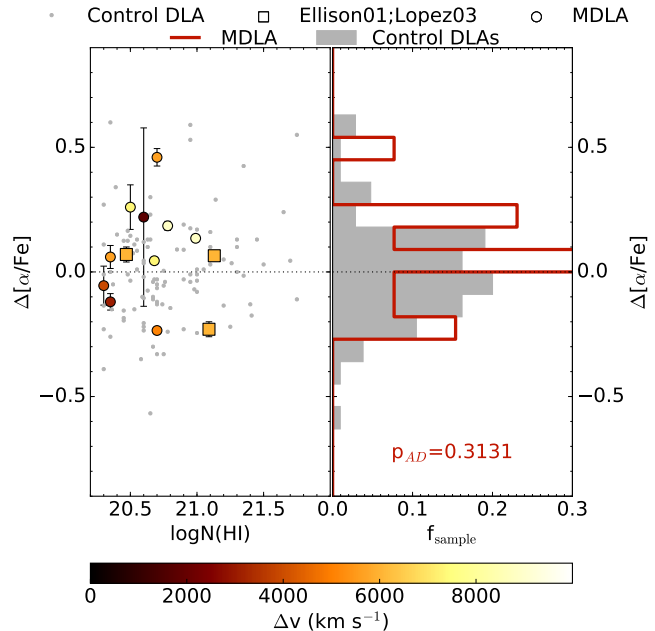


Figure 5. The relative change in $[\alpha/\text{Fe}]$ for MDLAs ($\Delta[\alpha/\text{Fe}]$) as a function of $\log N(\text{HI})$. The left panel shows $\Delta[\alpha/\text{Fe}]$ in MDLA sightlines compared to the control-matched sample (small grey points). For reference, the MDLAs observed in Lopez & Ellison (2003) are shown as large squares. The colour of the MDLA points represent the velocity separation of the DLAs along the sightline. The right panel shows the distribution of $\Delta[\alpha/\text{Fe}]$ for the MDLA (red) and control (grey) samples. The p-value from the Anderson-Darling test for the two MDLA samples relative to the control sample is displayed; suggesting that the MDLA and control DLAs are likely drawn from the same parent sample.

3.3 Proximate DLAs

The XQ-100 DLA catalogue from Sánchez-Ramírez et al. (2016) showed that five DLAs are PDLAs ($\Delta v \leq 5000 \text{ km s}^{-1}$ from the host QSO). The properties of the complete set of associated absorbers in XQ-100, not just limited to DLAs, can be found in Perrotta et al. (2016). With the addition of 41 PDLAs in the literature sample (Berg et al. 2015a), we test the effect of proximity of a DLA to its host QSO for 46 absorbers. Improving upon the analysis of 16 PDLAs in Ellison et al. (2010), we compare the relative abundance of a given PDLA to a control-matched sample of intervening DLAs.

The control matching was undertaken in an identical manner as for the MDLAs, with the exception that DLAs were matched by $\log N(\text{HI})$ and redshift. In addition, we require the control sample to have at least five measured abundances for each of the following elements: S, Si, Fe, and Zn⁹. The tolerance for the $\log N(\text{HI})$ match was set by the error in the PDLA's $\log N(\text{HI})$. If required, the $\log N(\text{HI})$ selection

⁹ The requirement of having five abundances for each element is the most restrictive criterion; but is required to ensure that DLAs are compared to the same control pool for each element. Without this criterion, all matching is completed within at most four expansions.

tolerance grew by ± 0.025 dex increments (15–25% of the typical error). The same criteria for redshift used for the MDLAs was imposed for the PDLAs as well. This matching procedure resulted in successful matches for all 46 PDLAs, with 25 PDLAs being matched within three expansions, and six PDLAs requiring 9 expansions. Each PDLA had at least 12 control matches. The median number of matched controls is 35.5 per PDLA, with 25% of PDLAs having 52 or more controls matches.

The main science result from the control-matching analysis for PDLAs is presented in Figure 6. We define $\Delta[X/H]$ as the difference in the PDLA abundance $[X/H]$ relative to the median abundance of control-matched sample; such that a negative $\Delta[X/H]$ would imply that the PDLA has a lower $[X/H]$ than the control-matched sample. The left-most panels of Figure 6 show $\Delta[X/H]$ as a function of $\log N(HI)$ for elements (in order from top to bottom rows) S, Si, Fe, and Zn. The error bars represent σ_{jack} of the control-matched sample. The colour of the points indicate the velocity separation (Δv ; km s^{-1}) from the host QSO. PDLAs from Ellison et al. (2010) are shown as large squares, and are included in the analysis. For comparison to the DLAs in the control pool, the smaller grey points are the $\Delta[X/H]$ obtained from repeating the control match on all control DLAs. The left panels of Figure 6 visually hint at a possible deficit of $[X/H]$ for PDLAs with $\log N(HI) \lesssim 21.0$, and an enhanced $[X/H]$ at $\log N(HI) \gtrsim 21.0$ (the enhancement was first identified for $[S/H]$ and $[Si/H]$ in Ellison et al. 2010).

To quantitatively test the possibility of a correlation between $\Delta[X/H]$ and $\log N(HI)$ in PDLAs, we performed the Pearson-r test. However, the test did not show any significant correlation of $\Delta[X/H]$ with $\log N(HI)$ ($r = 0.33, 0.18, 0.08, 0.00$ for S, Si, Fe, and Zn; respectively). Despite the lack of correlation, the AD statistic will additionally constrain whether the PDLAs are drawn from a different distribution of $\Delta[X/H]$ compared to the intervening control DLAs. The AD test was performed in three regimes: all $\log N(HI)$, $\log N(HI) < 21.0$, and $\log N(HI) > 21.0$. The distributions of $\Delta[X/H]$ (along with the associated p_{AD}) for each regime is displayed in the second, third, and fourth column of Figure 6 (respectively). The p_{AD} measurements suggest that PDLAs are likely drawn from a different distribution than the control DLAs for $[S/H]$ (null hypothesis rejected at $\sim 6\%$ confidence) and $[Fe/H]$ ($\sim 32\%$ confidence) for $\log N(HI) < 21.0$, as well as $[S/H]$ ($\sim 14\%$ confidence) and $[Si/H]$ ($\sim 26\%$ confidence) for $\log N(HI) > 21.0$.

As with the MDLAs, we attempted to assess the potential biases of using the Berg et al. (2015a) literature DLAs by only adopting control DLAs from the Rafelski et al. (2012) sample. Unfortunately only two PDLAs were matched at $\log N(HI) > 21.0$, and are unable to test how robust the results are. Similarly for $\log N(HI) < 21.0$, only seven PDLAs had measured $\Delta[S/H]$, six of which had $\Delta[S/H] \leq 0$. Again, we note that by matching $\log N(HI)$ should remove any effects caused by HI selection of control sample DLAs; whilst taking the median value of the control sample should remove any outlaying DLAs. A larger unbiased sample of DLAs is required to further evaluate the robustness of our results.

To test whether the $\Delta[X/H]$ offsets seen in PDLAs could occur by chance in a sample of this modest size, we ran a Monte Carlo simulation with 10 000 iterations, drawing

a random sample of control DLAs¹⁰ of the same size as the PDLAs sample for each element and $\log N(HI)$ cut. At each iteration, we computed the obtained median $\Delta[X/H]$ for each $\log N(HI)$ criteria. The distribution of obtained medians is shown in Figure 7. To understand the likelihood of observing such an offset by chance, we calculated the frequency of observing a median $\Delta[X/H]$ that is identical or further offset from zero than the median $\Delta[X/H]$ observed for the PDLAs. Table 8 provides the median $\Delta[X/H]$ of the PDLA sample, and summarizes the frequencies of this simulation for all four elements¹¹. The deficit of $[S/H]$ and $[Fe/H]$ for $\log N(HI) < 21.0$ was seen 3.2% and 5.4% of the time (respectively), suggesting it is unlikely the deficit in the observations is observed by random chance. The excess of $[S/H]$ at $\log N(HI) > 21.0$ is also unlikely to be caused by random chance, since *none* of the iterations demonstrated a similar median of $\Delta[S/H]$. The excess of $[Si/H]$ is seen slightly frequently 9.7% of the time. Therefore there is observational evidence that PDLAs exhibit different abundances than intervening DLAs.

We now consider the possible source of distinct abundances between PDLAs and intervening systems. The deficit of S and Fe in PDLA abundances at low $\log N(HI)$ might arise from ionization effects as the hard ionizing spectrum of the quasar is more likely to penetrate the self-shielding effect of DLAs at low $\log N(HI)$. A natural assumption might be that PDLAs closer to the QSO ($\Delta v \leq 1500 \text{ km s}^{-1}$ Ellison et al. 2010) may be more influenced by the higher radiation field. The mean and scatter in $\Delta[S/H]$ and $\Delta[Si/H]$ for $\log N(HI) < 21.0$ is the same across all Δv , suggesting that the velocity separation of a PDLA has little effect.

It is worth noting that the uncertainty in QSO's systemic z_{em} can be large (depending on which emission lines are used, e.g. Gaskell 1982; Tytler & Fan 1992), leading to a scatter in Δv determinations from tens to a couple of hundred km s^{-1} (for QSOs identified with the Sloan Digital Sky Survey; see Ellison et al. 2010; Hewett & Wild 2010; Pâris et al. 2011). In addition, the error in z_{abs} for the DLAs will also contribute to the precision of the Δv measurements. For the XQ-100 sample, the scatter in z_{abs} derived from HI absorption (Table 1) and the metal lines is $\pm 47 \text{ km s}^{-1}$. However, the lack of a strong correlation between $\Delta[X/H]$ and Δv suggests that higher precision measurements Δv are not required.

To further test ionization effects at $\log N(HI) < 21.0$, the observed $\Delta[X/H]$ were compared to abundance discrepancies observed in QSO-like radiation models from the literature. Both Vladilo et al. (2001) and Rix et al. (2007) modelled the effect of radiation fields (for a variety of ionization strengths U) on abundances in DLAs; with their ionization abundance corrections shown in Table 9 (where positive corrections imply the observed abundances are underestimated relative to the true value). As a reference, the soft stellar-like ionizing spectrum (denoted by S in Table 9) from Vladilo et al. (2001)

¹⁰ The randomly generated sample in each iteration does not contain the same DLA more than once; however the same DLA can appear in the samples of other iterations.

¹¹ To estimate the uncertainty on the simulation, we recomputed the frequencies of observing a $\Delta[X/H]$, taking into account the σ_{jack} of the PDLA $\Delta[X/H]$ to make the offset weaker. These recomputed frequencies are provided in parentheses in Table 8.

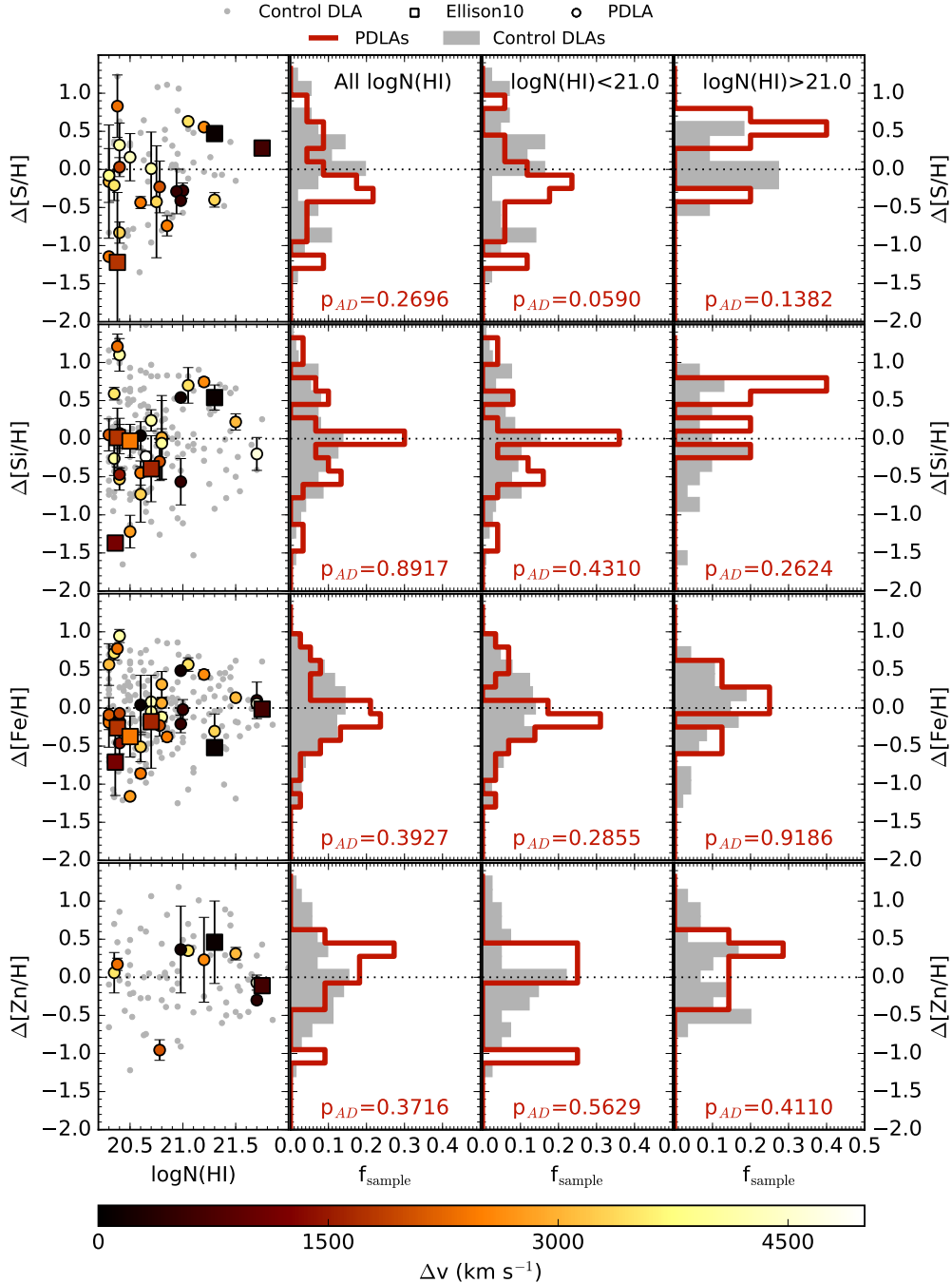


Figure 6. *First column:* The relative change in PDLA abundance compared to a sample of DLAs matched in redshift and $\log N(\text{HI})$ ($\Delta[\text{X}/\text{H}]$) as a function of $\log N(\text{HI})$. Each row is $\Delta[\text{X}/\text{H}]$ for S, Si, Fe, and Zn (top to bottom). The notation is the same as Figure 5. In all panels, we highlight the data from Ellison et al. (2010) as large squares for comparison. *Second column:* The fractional distribution of $\Delta[\text{X}/\text{H}]$ for each element in PDLAs (red line) and the control sample (grey shaded region). *Third column:* The fractional distribution of $\Delta[\text{X}/\text{H}]$ for each element, restricting both samples to DLAs with only $\log N(\text{HI}) < 21.0$. *Fourth column:* The fractional distribution of $\Delta[\text{X}/\text{H}]$ for each element, restricting both samples to DLAs with $\log N(\text{HI}) > 21.0$. All PDLA distributions are compared to the control-sample distribution using the Anderson-Darling test, showing the p-value (p_{AD}) that the two distributions are drawn from the same parent sample.

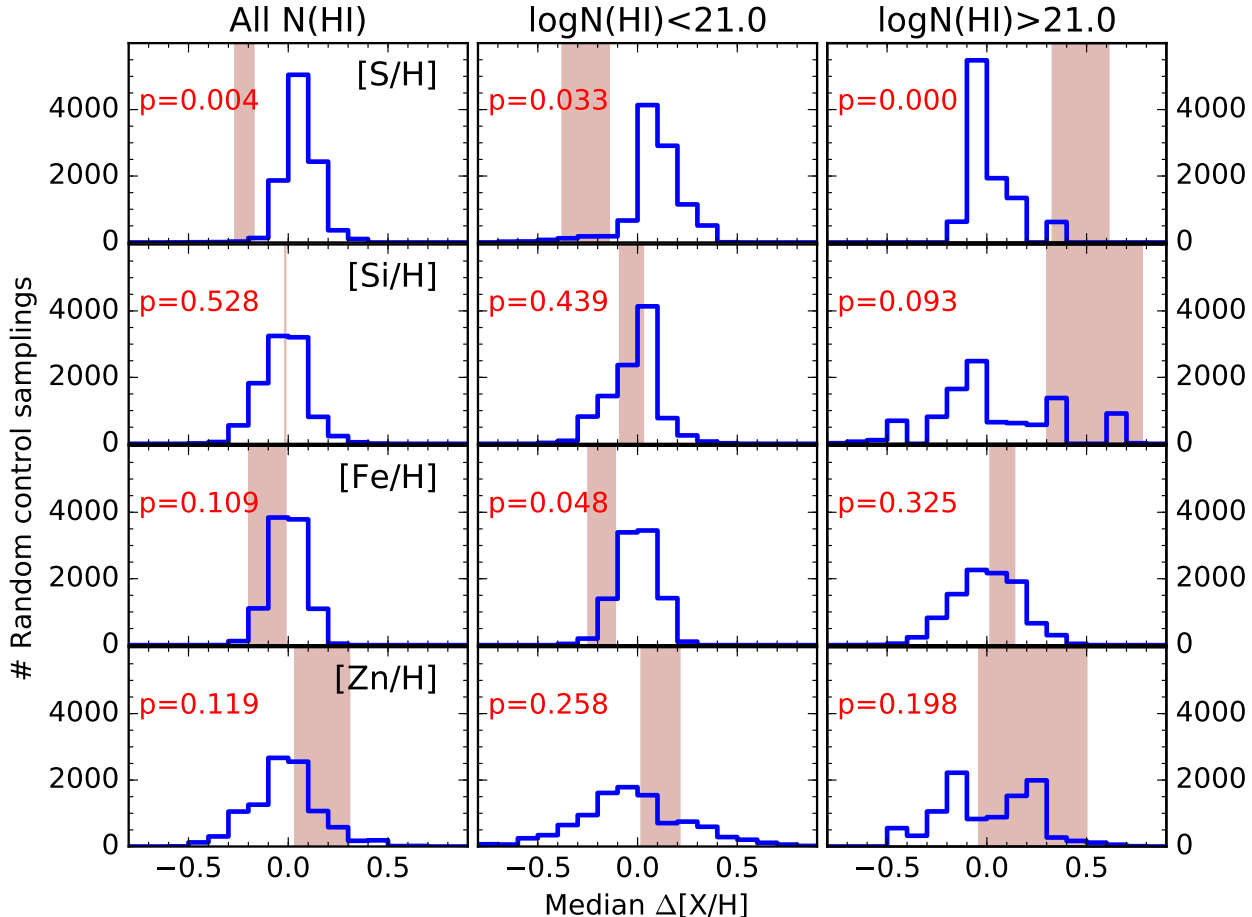


Figure 7. The frequency (of 10 000 iterations) of observing a median $\Delta[X/H]$ in a randomly-selected control sample of the same size as the PDLA sample. Each row is for the elements S, Si, Fe, and Zn (top to bottom; respectively), while each column is the $\log N(\text{HI})$ cut on the sample (all $N(\text{HI})$, $\log N(\text{HI}) < 21.0$, and $\log N(\text{HI}) > 21.0$; left to right, respectively). The red band indicates the median $\Delta[X/H]$ of the PDLA sample, whose half-width is given by σ_{jack} of the PDLA $\Delta[X/H]$. The probability (p) of observing a median $\Delta[X/H]$ of the same magnitude (or further offset from 0) as the PDLA median $\Delta[X/H]$ is displayed.

Table 8. Frequencies of obtaining median PDLA $\Delta[X/H]$ from control DLA resampling.

X	All $N(\text{HI})$		$\log N(\text{HI}) < 21.0$		$\log N(\text{HI}) > 21.0$	
	Median $\Delta[X/H]$	Freq. (%)	Median $\Delta[X/H]$	Freq. (%)	Median $\Delta[X/H]$	Freq. (%)
[S/H]	-0.22 ± 0.05	0.4 (0.5) ¹	-0.26 ± 0.12	3.3 (5.8) ¹	0.47 ± 0.14	0.0 (6.2) ¹
[Si/H]	-0.02 ± 0.00	52.8 (53.0) ¹	-0.03 ± 0.06	43.9 (62.4) ¹	0.54 ± 0.24	9.3 (23.1) ¹
[Fe/H]	-0.10 ± 0.09	10.9 (43.6) ¹	-0.18 ± 0.07	4.8 (14.0) ¹	0.08 ± 0.06	32.5 (47.6) ¹
[Zn/H]	0.17 ± 0.14	11.9 (38.4) ¹	0.12 ± 0.10	25.8 (39.6) ¹	0.23 ± 0.27	19.8 (58.5) ¹

¹Frequency including PDLA σ_{jack} in median $\Delta[X/H]$.

is also included. For a hard, QSO-like ionizing field (flagged by $^{\text{H}}$ in Table 9); Vladilo et al. (2001) found that [Fe/H] is *over-predicted* by a factor of 0.01–0.04 dex; whereas we are finding that [Fe/H] is *underestimated* in PDLAs. The corrections for the single PDLA modelled by Rix et al. (2007) are qualitatively similar. Both sets of models suggest that the deficit of [Fe/H] in PDLAs *cannot* be explained by ionization; and we rule out ionization as a possible explanation.

However, the deficit for [S/H] could be explained by ionization corrections for $\log N(\text{HI}) < 21.0$; but not for the excess seen at $\log N(\text{HI}) > 21.0$ (Ellison et al. 2010).

A suggestion in Ellison et al. (2010) is that PDLAs are typically probing more massive galaxies (relative to intervening systems). To test this explanation for the metallicity effect we are seeing, we checked whether the v_{90} parameter (a proxy for mass in DLAs; Prochaska & Wolfe 1997;

Table 9. Literature PDLA ionization corrections

[X/H]	logN(HI)= 20.35 ¹			logN(HI)= 20.75 ¹			logN(HI)= 20.8 ²	
	$U = -4.2^H$ (dex)	$U = -2.2^S$ (dex)	$U = -1.7^S$ (dex)	$U = -4.8^H$ (dex)	$U = -2.2^S$ (dex)	$U = -1.7^S$ (dex)	$U = -4.0^H$ (dex)	$U = -2.0^H$ (dex)
[Si/H]	-0.04	-0.09	-0.16	-0.01	-0.03	-0.07	-0.02	-0.09
[S/H]	+0.15	-0.20	-0.15	+0.09	-0.07	-0.09	+0.03	+0.26
[Fe/H]	-0.04	-0.02	-0.02	-0.01	-0.01	-0.01	-0.01	-0.05
[Zn/H]	+0.32	-0.35	-0.73	+0.16	-0.17	-0.44	+0.15	+0.58

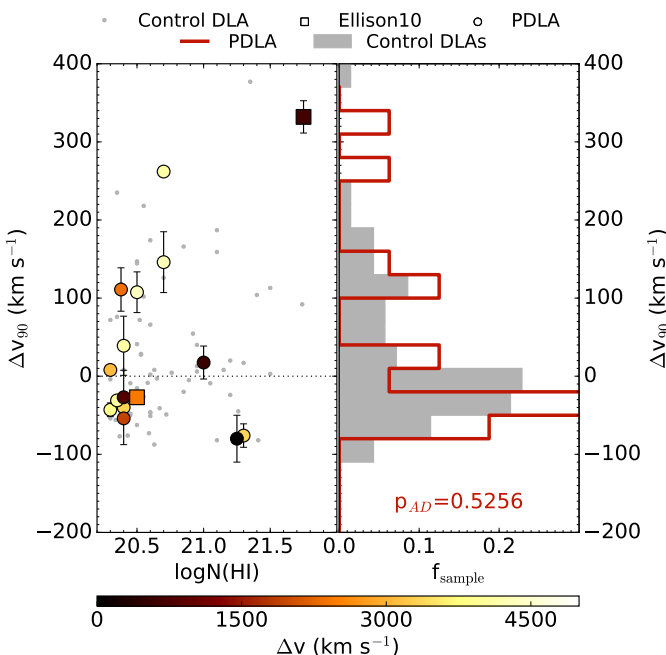
¹Vladilo et al. (2001).²Rix et al. (2007).^SSoft, stellar-type ionization spectrum.^HHard, QSO-like ionization spectrum.

Figure 8. Left Panel: The difference in v_{90} between a given PDLA and control-matched sample (Δv_{90}), as a function of $\log(N\text{HI})$. The notation is the same as Figure 5. Right Panel: distributions of Δv_{90} for the PDLA sample (red line) compared to the control sample (grey bars). The Anderson-Darling p -value is shown for the comparison of the two distributions.

Ledoux et al. 2006; Møller et al. 2013; Neeleman et al. 2013) is substantially larger in PDLAs than in the control sample. In addition to the v_{90} measurements of the XQ-100 sample (Table 4), we also adopt the 139 v_{90} measurements from HIRES data for DLAs in the literature (Neeleman et al. 2013; Berg et al. 2015b) for the control-matched sample.

Figure 8 shows the difference in v_{90} for a PDLA relative to its control matched sample (Δv_{90} ; a positive value implying the PDLA has a large v_{90} than the matched controls). Again, the smaller grey points show the scatter within the control sample. There is no significant discrepancy between the v_{90} in PDLAs relative to the control, suggesting no dependence on mass; assuming v_{90} is a good proxy for mass.

3.4 [Zn/Fe] and dust depletion

Dust depletion plagues DLA abundance analysis work, making it difficult to disentangle nucleosynthetic patterns from dust depletion effects. In particular, a dust-free Fe peak tracer is necessary to measure the intrinsic $[\alpha/\text{Fe}]$ ratio, an important tracer of star formation history (Tinsley 1979; Venn et al. 2004; Tolstoy et al. 2009). In general, the community has either used elements that are relatively unaffected by depletion (such as S and Zn; e.g. Pettini et al. 1997; Centurión et al. 2000; Vladilo et al. 2011) or modelled dust depletions based on chemical evolution assumptions (e.g. Vladilo et al. 2011). One of the most prominent assumptions is that Zn is a dust-free proxy of the Fe peak (Pettini et al. 1994, 1997; Vladilo 2002a,b). The assumption that Zn traces Fe was motivated by early observations of Galactic stellar abundances showing $[\text{Zn}/\text{Fe}] \sim 0$ over a range of metallicities (Sneden & Crocker 1988; Sneden et al. 1991; Chen et al. 2004; Nissen et al. 2004).

However, with the search for metal-poor stars extending to lower metallicities (e.g. Prochaska et al. 2000; Nissen et al. 2007), stellar $[\text{Zn}/\text{Fe}]$ showed deviations from solar suggesting that Zn does not necessarily trace Fe; leading some authors to question whether Zn traces Fe in DLAs (such as Prochaska & Wolfe 2000; Nissen & Schuster 2011; Rafelski et al. 2012). Recently, Berg et al. (2015a) compared $[\text{Zn}/\text{Fe}]$ in stars in the Milky Way and local dwarf spheroidal (dSph) galaxies, finding a large scatter of $[\text{Zn}/\text{Fe}]$ at $-2.0 < [\text{Zn}/\text{H}] < -0.5$. In particular, many (but not all) Local Group dwarf galaxy stars exhibit subsolar $[\text{Zn}/\text{Fe}]$ indicating that Zn is not necessarily a nucleosynthetic tracer of the Fe-peak elements at $[\text{Zn}/\text{H}] \geq -1.5$. In order to investigate the possibility of intrinsically non-solar $[\text{Zn}/\text{Fe}]$ ratios, Berg et al. (2015a) infer the dust-corrected values of $[\text{Zn}/\text{Fe}]$ using a novel method. Rather than using modelled corrections which require assumptions about the nature of DLAs (such as Vladilo et al. 2011), Berg et al. (2015a) assume that all α -elements trace each other in DLAs, and that the measured ratio of two α -elements may be a tracer of dust depletion. Using the relative depletions seen towards Galactic ISM sightlines (Savage & Sembach 1996), they suggest that $[\text{Si}/\text{Ti}]$ should have the same depletion correction as $[\text{Zn}/\text{Fe}]$, and can be used to correct the $[\text{Zn}/\text{Fe}]$ abundance for depletion to within 0.1 dex.

Although the Berg et al. (2015a) analysis of dust corrected $[\text{Zn}/\text{Fe}]$ is strongly suggestive of sub-solar ratios in DLAs, their analysis was limited to the 43 systems (of which

only 10 were detections) for which Ti measurements are available. This limitation is driven by typically only covering the weak Ti_{III} 1910 Å line in optical spectra for the majority of the DLA sample. Previous surveys of Mg_{II} abundances with high resolution spectroscopy have been limited to $z_{\text{abs}} \sim 2\text{--}3$ DLAs (e.g. Prochaska et al. 2003; Dessauges-Zavadsky et al. 2006; Prochaska et al. 2007; Noterdaeme et al. 2008). With the additional IR coverage that X-Shooter provides, we have unprecedented access to absorption lines of α -elements that are not typically observed in the optical; particularly in absorbers at redshifts 3–4. These lines include: Mg, Ca, as well as stronger Ti lines (relative to Ti_{III} 1910Å; Ti_{III} λ 3073Å, 3242Å, and 3384Å).

With the XQ-100 DLA sample we are thus able to further test the intrinsic [Zn/Fe] ratio of DLAs, by using the new Ti_{III} abundances, as well as other α -elements ratios ([Mg/Si] and [Ca/Si]) as additional dust-depletion proxies. Figure 9 shows the DLA dust-corrected [Zn/Fe] abundances (coloured circles) as a function of metallicity using [Si/Ca] (left panel), [Si/Mg] (middle panel), and [Si/Ti] (right panel). For reference, the Galactic (grey points) and dSph (grey squares) stellar trends of [Zn/Fe] are shown in each panel.

The difficulty of using Mg_{II} and Ca_{II} is that the differential depletion of [Si/Ca] and [Si/Mg] is much different than [Zn/Fe] (differences of +0.8 and −1.4 dex in Galactic ISM sightlines, respectively Savage & Sembach 1996). The two horizontal dashed lines in each panel constrain the region where the dust-corrected [Zn/Fe] could be consistent with solar [Zn/Fe] based on the differential depletion of $[\alpha/\text{Si}] - [\text{Zn}/\text{Fe}]$ in the Milky Way; where DLA points below the lowest line are consistent with intrinsically subsolar [Zn/Fe], and DLA above the higher line likely have supersolar [Zn/Fe].

The addition of Ti abundances from the XQ-100 DLA sample (red circles) does not provide any additional information on the intrinsic nature of [Zn/Fe] in DLAs previously identified by Berg et al. (2015a) (blue circles). One of the XQ-100 DLAs has a dust-corrected [Zn/Fe] ~ 0.3 dex. Although supersolar, this one system is consistent with both Milky Way and dSphs stellar [Zn/Fe] abundances (Berg et al. 2015a). Although the Ti_{III} lines accessible in the NIR are nominally stronger than those in the optical, the typical detection limits of Ti_{III} from the lower resolution X-Shooter spectra are not as sensitive as the measurements available from UVES or HIRES. It is worth noting that of the 38 cases Ti_{III} abundances were measured in the XQ-100 DLAs, 28 abundances were preferentially adopted based on the Ti_{III} lines in the NIR arm rather than the Ti_{III} λ 1910Å line. Therefore the use of X-Shooter to observe lines in the NIR can be a useful tool to obtain (more constraining) Ti_{III} abundances.

The additional five Ca_{II} robust upper limits (to the single detection in the literature) in the left panel of Figure 9 further support that DLAs span the same range of [Zn/Fe] as dSphs seen by Berg et al. (2015a), suggesting that DLAs share a similar nucleosynthetic history as Galactic dSphs. However, we note that Ca_{II} (excitation potential of 11.87eV) is not the dominant ionization state of Ca in DLAs (e.g. Wild et al. 2006), suggesting that the measured N(Ca_{II}) may require significant ionization corrections.

4 SUMMARY AND CONCLUSIONS

The sample of XQ-100 DLAs provides coverage of the relatively moderately-sampled redshift range $z_{\text{abs}} = 3\text{--}4$. We have computed the column densities for a variety of metals in the 41 DLAs in the XQ-100 sample. The additional coverage from the NIR arm of X-Shooter provides coverage of rarely detected lines at redshifts 3–4 in abundance studies such as Mg_{II}, Ca_{II}, and strong Ti_{III} lines. With the addition of dust-depleted α -elements, we are able to test the dust-corrected [Zn/Fe] to see if [Zn/Fe] is solar in DLAs. We have shown in Section 3.4 that [Zn/Fe] is not necessarily solar in DLAs, and that [Zn/Fe] shows the same range of values as seen in the dSphs of the Local Group (in agreement with Berg et al. 2015a).

In combination with a sample of DLAs drawn from the literature, we have provided a statistical analysis of PDLAs (within $\Delta v \leq 5000 \text{ km s}^{-1}$ of the host QSO) and MDLAs (two or more DLAs separated by $500 \leq \Delta v \leq 10000 \text{ km s}^{-1}$) by comparing to a control-matched sample of individual, intervening absorbers. We do not find any suppression in $[\alpha/\text{Fe}]$ in MDLAs, suggesting that there is no evidence for truncated star formation between nearby DLAs on their abundance. Relative to a control sample of DLAs, we note a mildly elevated [S/H] and [Si/H] for high $\log N(\text{H}_I) > 21.0$ PDLAs at (AD test rejects the null hypothesis at 14% and 26% confidence; respectively), as previously seen by Ellison et al. (2010); however, we also detect a deficit in [S/H] and [Fe/H] (null hypothesis rejected at 6% and 32% confidence, respectively) for PDLAs with $\log N(\text{H}_I) < 21.0$. These abundance discrepancies appear to be independent of velocity separation of the host QSO and the mass proxy v_{90} . It is possible to explain the deficit of [S/H] at low $\log N(\text{H}_I)$ through ionization corrections, but not the deficit of [Fe/H].

We have also presented UVES observations of three DLAs towards J0034+1639 in order to investigate an MPDLA candidate at $z_{\text{abs}} \sim 4.25$ with a $[\text{Fe}/\text{H}] = -2.82 \pm 0.11$. This MPDLA is consistent with abundances in the typical MPDLA (Cooke et al. 2011). MPDLAs such as the one towards J0034+1639 prime targets for easily detecting Ni and other discriminating elements in future follow-up observations with 30-m class telescopes.

ACKNOWLEDGEMENTS

We thank the anonymous referee for their useful comments that clarified the text. TAMB is grateful for Ryan Cooke's assistance with developing a science case for the UVES observations of the MPDLA, and discussing the results. SLE acknowledges the receipt of an NSERC Discovery Grant which supported this research. JXP is supported by NSF grant AST-1109447. SL has been supported by FONDECYT grant number 1140838 and partially by PFB-06 CATA. KDD is supported by an NSF AAPF fellowship awarded under NSF grant AST-1302093.

REFERENCES

- Akerman C. J., 2005, PhD thesis, University of Cambridge
- Akerman C. J., Ellison S. L., Pettini M., Steidel C. C., 2005, A&A, 440, 499

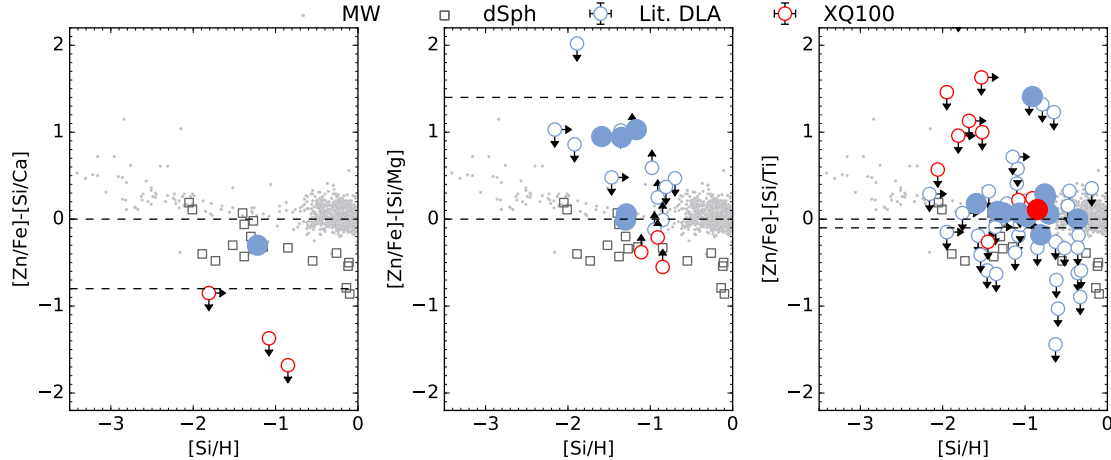


Figure 9. Dust-corrected $[Zn/Fe]$ DLA abundances (XQ-100 are in red, literature DLAs in blue) relative to stellar $[Zn/Fe]$ (grey points are the Milky Way, dark grey squares are dSphs) from Berg et al. (2015a). Larger, filled DLA circles represent detections, whereas the unfilled circles are limits. The dust correction is determined by subtracting the ratio of two α -elements of different relative dust depletions ($[Si/Ca]$ left panel; $[Si/Mg]$ middle panel; $[Si/Ti]$ right panel). The two dashed lines bound the region where $[Zn/Fe]$ may be consistent with solar, such that measurements below the line are consistent with subsolar $[Zn/Fe]$. In addition to $[Si/Ti]$, $[Si/Ca]$ can also constrain the intrinsic $[Zn/Fe]$ in DLAs. Both of these ratios indicate that DLAs are consistent with the subsolar values seen in dSphs (Berg et al. 2015a). This subsolar $[Zn/Fe]$ is likely nucleosynthetic in origin.

- Asplund M., Grevesse N., Sauval A. J., Scott P., 2009, *ARA&A*, 47, 481
 Becker G. D., Sargent W. L. W., Rauch M., Carswell R. F., 2012, *ApJ*, 744, 91
 Beers T. C., Christlieb N., 2005, *ARA&A*, 43, 531
 Berg T. A. M., Ellison S. L., Prochaska J. X., Venn K. A., Dessauges-Zavadsky M., 2015a, *MNRAS*, 452, 4326
 Berg T. A. M., Neeleman M., Prochaska J. X., Ellison S. L., Wolfe A. M., 2015b, *PASP*, 127, 167
 Cayrel R. et al., 2004, *A&A*, 416, 1117
 Centurión M., Bonifacio P., Molaro P., Vladilo G., 2000, *ApJ*, 536, 540
 Chen Y. Q., Nissen P. E., Zhao G., 2004, *A&A*, 425, 697
 Cooke R., Pettini M., Jorgenson R. A., Murphy M. T., Rudie G. C., Steidel C. C., 2013, *MNRAS*, 431, 1625
 Cooke R., Pettini M., Steidel C. C., Rudie G. C., Nissen P. E., 2011, *MNRAS*, 417, 1534
 Cooke R. J., Madau P., 2014, *ApJ*, 791, 116
 Cooke R. J., Pettini M., Jorgenson R. A., 2015, *ApJ*, 800, 12
 Dekker H., D'Odorico S., Kaufer A., Delabre B., Kotzlowski H., 2000, in Society of Photo-Optical Instrumentation Engineers (SPIE) Conference Series, Vol. 4008, Optical and IR Telescope Instrumentation and Detectors, Iye M., Moorwood A. F., eds., pp. 534–545
 Dessauges-Zavadsky M., Calura F., Prochaska J. X., D'Odorico S., Matteucci F., 2004, *A&A*, 416, 79
 Dessauges-Zavadsky M., D'Odorico S., McMahon R. G., Molaro P., Ledoux C., Péroux C., Storrie-Lombardi L. J., 2001, *A&A*, 370, 426
 Dessauges-Zavadsky M., Prochaska J. X., D'Odorico S., Calura F., Matteucci F., 2006, *A&A*, 445, 93
 D'Odorico V., 2007, *A&A*, 470, 523
 Ellison S. L., Lopez S., 2001, *A&A*, 380, 117
 Ellison S. L., Prochaska J. X., Hennawi J., Lopez S., Usher C., Wolfe A. M., Russell D. M., Benn C. R., 2010, *MNRAS*, 406, 1435
 Ellison S. L., Prochaska J. X., Mendel J. T., 2011, *MNRAS*, 412, 448
 Ellison S. L., Yan L., Hook I. M., Pettini M., Wall J. V., Shaver P., 2002, *A&A*, 383, 91
 Frebel A., Bromm V., 2012, *ApJ*, 759, 115
 Frebel A., Norris J. E., 2015, *ARA&A*, 53, 631
 Gaskell C. M., 1982, *ApJ*, 263, 79
 Greif T. H., Johnson J. L., Bromm V., Klessen R. S., 2007, *ApJ*, 670, 1
 Heger A., Woosley S. E., 2010, *ApJ*, 724, 341
 Henry R. B. C., Prochaska J. X., 2007, *PASP*, 119, 962
 Hewett P. C., Wild V., 2010, *MNRAS*, 405, 2302
 Jacobson H. R. et al., 2015, *ApJ*, 807, 171
 Jenkins E. B., Tripp T. M., 2006, *ApJ*, 637, 548
 Jorgenson R. A., Wolfe A. M., Prochaska J. X., 2010, *ApJ*, 722, 460
 Krogager J.-K., Fynbo J. P. U., Noterdaeme P., Zafar T., Møller P., Ledoux C., Krühler T., Stockton A., 2016, *MNRAS*, 455, 2698
 Kulkarni V. P., Fall S. M., Truran J. W., 1997, *ApJL*, 484, L7
 Ledoux C., Bergeron J., Petitjean P., 2002, *A&A*, 385, 802
 Ledoux C., Petitjean P., Fynbo J. P. U., Møller P., Srianand R., 2006, *A&A*, 457, 71
 Lopez S., Ellison S. L., 2003, *A&A*, 403, 573
 López S., et al., 2016, Accepted to *A&A*. DOI: 10.1051/0004-6361/201628161
 Lu L., Sargent W. L. W., Barlow T. A., 1998, *AJ*, 115, 55
 Lu L., Sargent W. L. W., Barlow T. A., Churchill C. W., Vogt S. S., 1996, *ApJS*, 107, 475
 McWilliam A., 1997, *ARA&A*, 35, 503
 Molaro P., Bonifacio P., Centurión M., D'Odorico S., Vladilo G., Santin P., Di Marcantonio P., 2000, *ApJ*, 541, 54
 Møller P., Fynbo J. P. U., Ledoux C., Nilsson K. K., 2013,

- MNRAS, 430, 2680
Morton D. C., 2003, ApJS, 149, 205
Neeleman M., Wolfe A. M., Prochaska J. X., Rafelski M., 2013, ApJ, 769, 54
Nissen P. E., Akerman C., Asplund M., Fabbian D., Kerber F., Kaufl H. U., Pettini M., 2007, A&A, 469, 319
Nissen P. E., Chen Y. Q., Asplund M., Pettini M., 2004, A&A, 415, 993
Nissen P. E., Schuster W. J., 2011, A&A, 530, A15
Nomoto K., Kobayashi C., Tominaga N., 2013, ARA&A, 51, 457
Norris J. E. et al., 2013, ApJ, 762, 25
Noterdaeme P., Ledoux C., Petitjean P., Srianand R., 2008, A&A, 481, 327
Páris I. et al., 2011, A&A, 530, A50
Penprase B. E., Prochaska J. X., Sargent W. L. W., Toromartinez I., Beeler D. J., 2010, ApJ, 721, 1
Perrotta S. et al., 2016, MNRAS, 462, 3285
Petitjean P., Ledoux C., Srianand R., 2008, A&A, 480, 349
Pettini M., Smith L. J., Hunstead R. W., King D. L., 1994, ApJ, 426, 79
Pettini M., Smith L. J., King D. L., Hunstead R. W., 1997, ApJ, 486, 665
Prochaska J. X., Chen H.-W., Wolfe A. M., Dessauges-Zavadsky M., Bloom J. S., 2008a, ApJ, 672, 59
Prochaska J. X., Gawiser E., Wolfe A. M., Cooke J., Gelino D., 2003, ApJS, 147, 227
Prochaska J. X., Hennawi J. F., Herbert-Fort S., 2008b, ApJ, 675, 1002
Prochaska J. X., Herbert-Fort S., 2004, PASP, 116, 622
Prochaska J. X., Naumov S. O., Carney B. W., McWilliam A., Wolfe A. M., 2000, AJ, 120, 2513
Prochaska J. X., Wolfe A. M., 1997, ApJ, 487, 73
Prochaska J. X., Wolfe A. M., 2000, ApJL, 533, L5
Prochaska J. X., Wolfe A. M., 2002, ApJ, 566, 68
Prochaska J. X., Wolfe A. M., Howk J. C., Gawiser E., Burles S. M., Cooke J., 2007, ApJS, 171, 29
Prochaska J. X. et al., 2001, ApJS, 137, 21
Rafelski M., Neeleman M., Fumagalli M., Wolfe A. M., Prochaska J. X., 2014, ApJL, 782, L29
Rafelski M., Wolfe A. M., Prochaska J. X., Neeleman M., Mendez A. J., 2012, ApJ, 755, 89
Rao S. M., Turnshek D. A., Nestor D. B., 2006, ApJ, 636, 610
Rix S. A., Pettini M., Steidel C. C., Reddy N. A., Adelberger K. L., Erb D. K., Shapley A. E., 2007, ApJ, 670, 15
Ruel J. et al., 2014, ApJ, 792, 45
Russell D. M., Ellison S. L., Benn C. R., 2006, MNRAS, 367, 412
Sánchez-Ramírez R. et al., 2016, MNRAS, 456, 4488
Savage B. D., Sembach K. R., 1991, ApJ, 379, 245
Savage B. D., Sembach K. R., 1996, ARA&A, 34, 279
Skúladóttir Á., Tolstoy E., Salvadori S., Hill V., Pettini M., Shetrone M. D., Starkenburg E., 2015, A&A, 574, A129
Sneden C., Crocker D. A., 1988, ApJ, 335, 406
Sneden C., Gratton R. G., Crocker D. A., 1991, A&A, 246, 354
Songaila A., Cowie L. L., 2002, AJ, 123, 2183
Spite M. et al., 2011, A&A, 528, A9
Suda T. et al., 2008, PASJ, 60, 1159
Tinsley B. M., 1979, ApJ, 229, 1046
Tolstoy E., Hill V., Tosi M., 2009, ARA&A, 47, 371
Tumlinson J. et al., 2010, ApJL, 718, L156
Tytler D., Fan X.-M., 1992, ApJS, 79, 1
Umeda H., Nomoto K., 2002, ApJ, 565, 385
Venn K. A., Irwin M., Shetrone M. D., Tout C. A., Hill V., Tolstoy E., 2004, AJ, 128, 1177
Vernet J. et al., 2011, A&A, 536, A105
Vladilo G., 2002a, ApJ, 569, 295
Vladilo G., 2002b, A&A, 391, 407
Vladilo G., Abate C., Yin J., Cescutti G., Matteucci F., 2011, A&A, 530, A33
Vladilo G., Centurión M., Bonifacio P., Howk J. C., 2001, ApJ, 557, 1007
Wild V., Hewett P. C., Pettini M., 2006, MNRAS, 367, 211
Wolfe A. M., Gawiser E., Prochaska J. X., 2005, ARA&A, 43, 861
Wolfe A. M., Lanzetta K. M., Foltz C. B., Chaffee F. H., 1995, ApJ, 454, 698
Wolfe A. M., Prochaska J. X., Gawiser E., 2003, ApJ, 593, 215
Wolfe A. M., Turnshek D. A., Smith H. E., Cohen R. D., 1986, ApJS, 61, 249
Woosley S. E., Weaver T. A., 1995, ApJS, 101, 181
Zafar T., Centurión M., Péroux C., Molaro P., D'Odorico V., Vladilo G., Popping A., 2014a, MNRAS, 444, 744
Zafar T., Vladilo G., Péroux C., Molaro P., Centurión M., D'Odorico V., Abbas K., Popping A., 2014b, MNRAS, 445, 2093

APPENDIX A: VELOCITY PROFILES AND AODM TABLES

A1 XQ-100 sample

Table A1. X-Shooter metal column densities for J0006–6208 ($z_{\text{abs}}=3.203$)

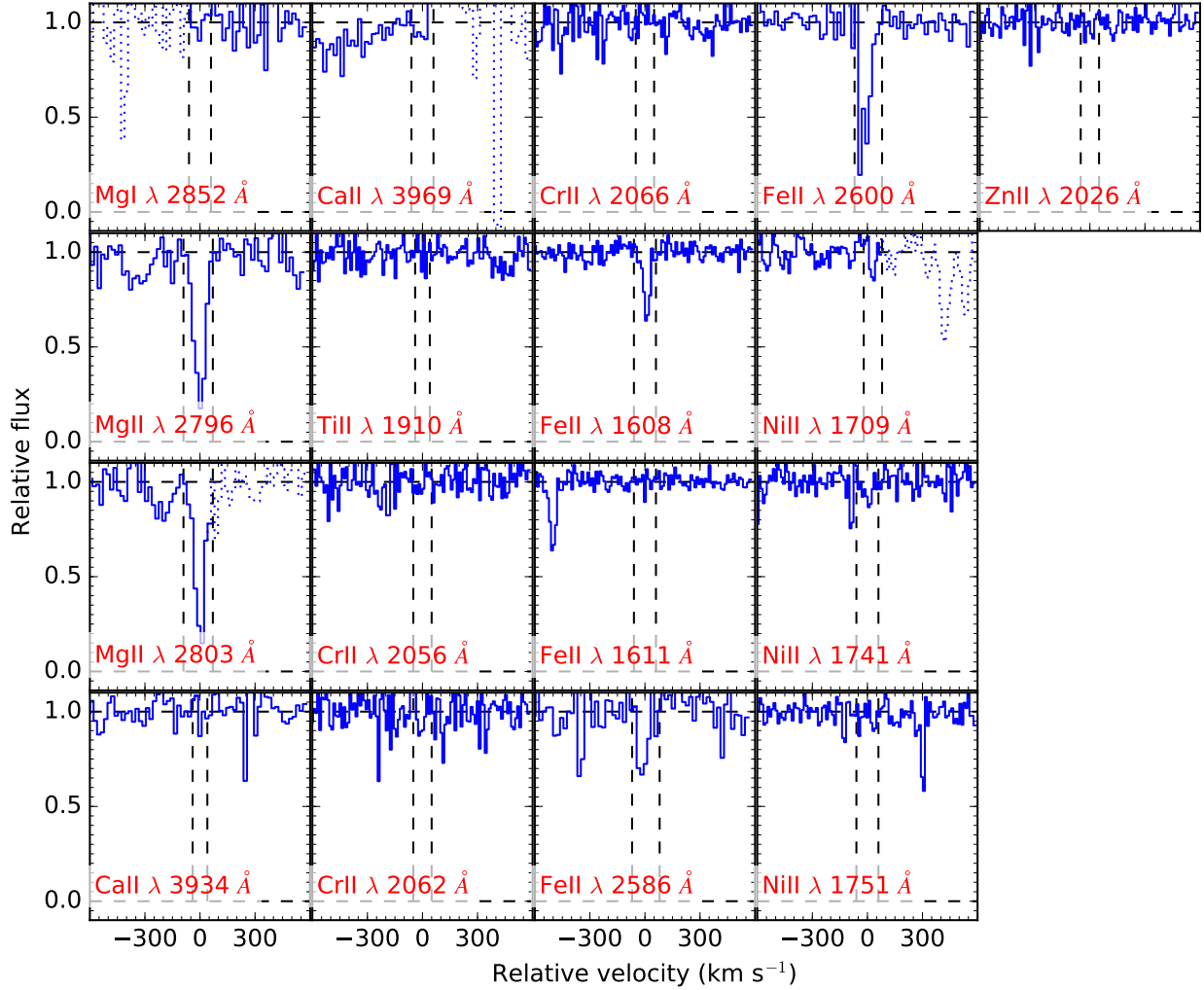


Figure A1. Velocity profile of the XQ100 spectrum towards J0006-6208 ($z_{\text{abs}}=3.203$).

Table A2. X-Shooter metal column densities for J0006–6208 ($z_{\text{abs}}=3.775$)

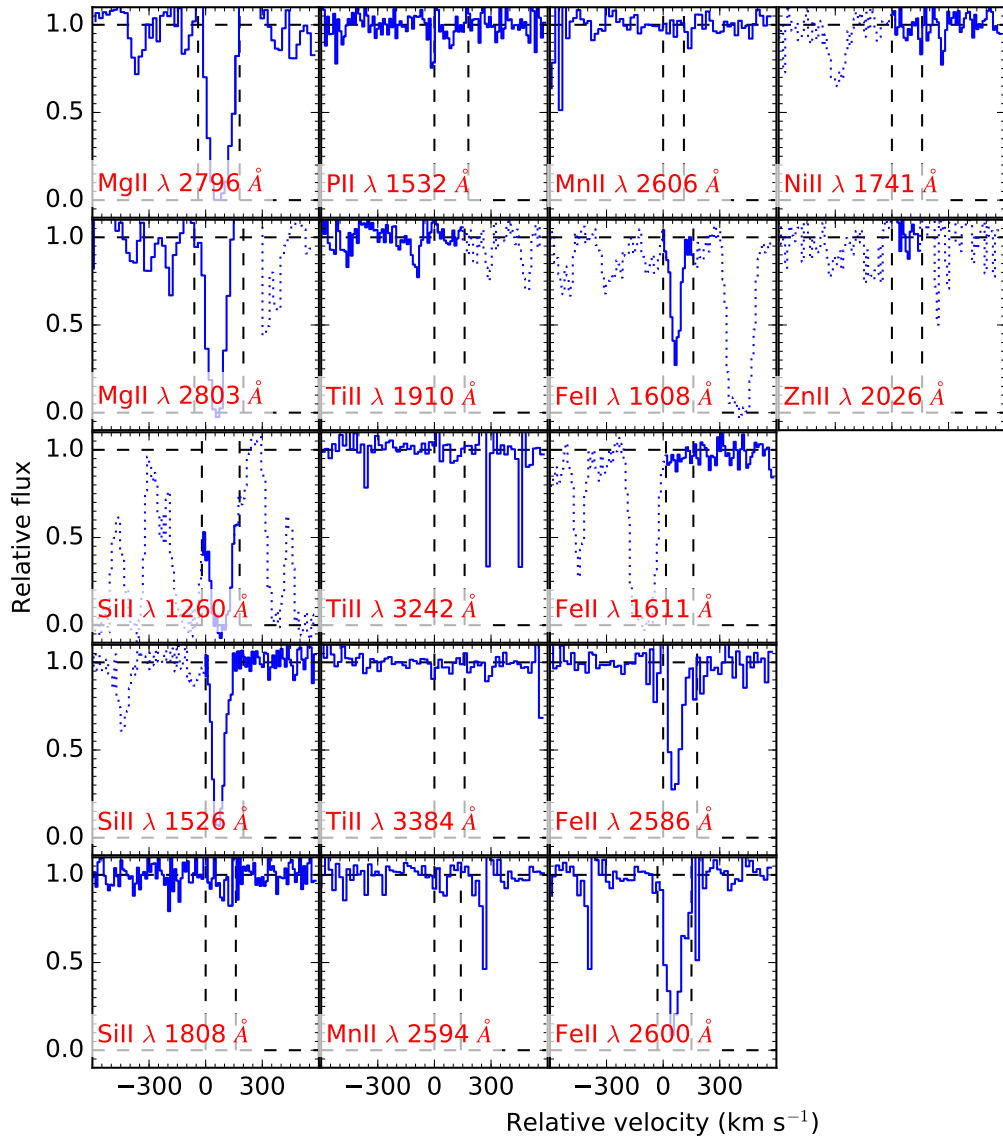


Figure A2. Velocity profile of the XQ100 spectrum towards J0006-6208 ($z_{\text{abs}}=3.775$).

Table A3. X-Shooter metal column densities for J0034+1639 ($z_{\text{abs}}=3.755$)

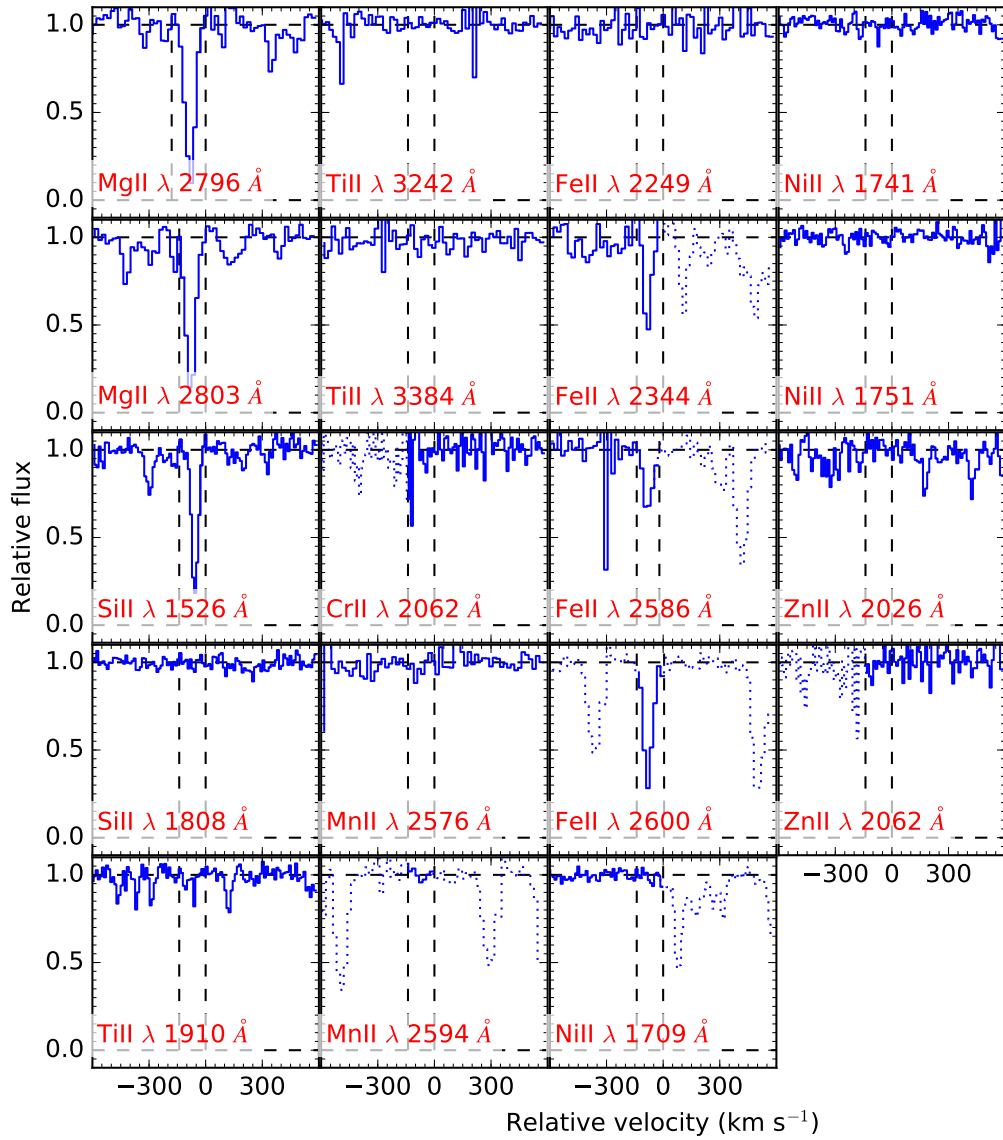


Figure A3. Velocity profile of the XQ100 spectrum towards J0034+1639 ($z_{\text{abs}}=3.755$).

Table A4. X-Shooter metal column densities for J0034+1639 ($z_{\text{abs}}=4.284$)

Table A5. X-Shooter metal column densities for J0034+1639 ($z_{\text{abs}}=4.252$)

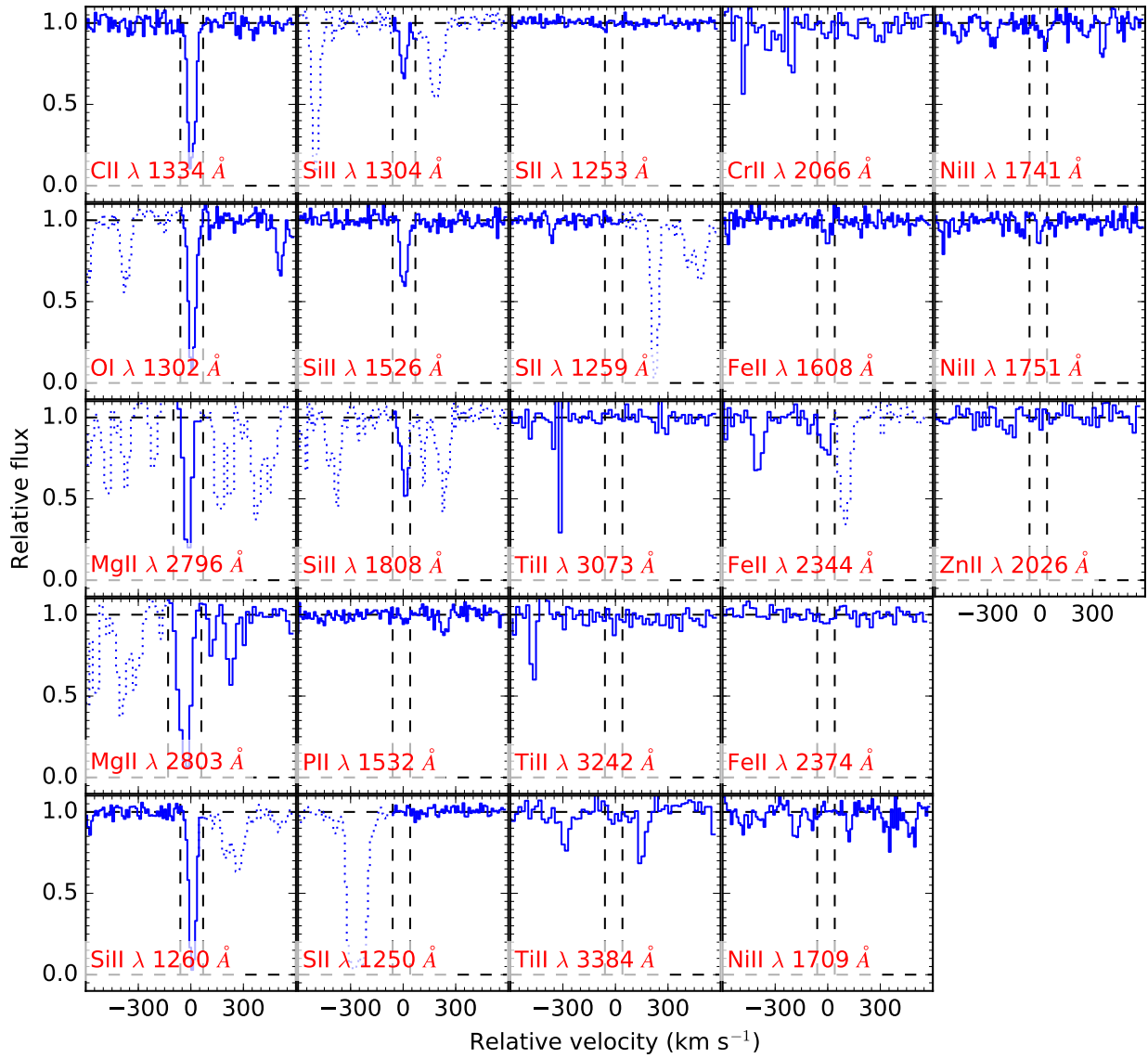


Figure A4. Velocity profile of the XQ100 spectrum towards J0034+1639 ($z_{\text{abs}}=4.251$).

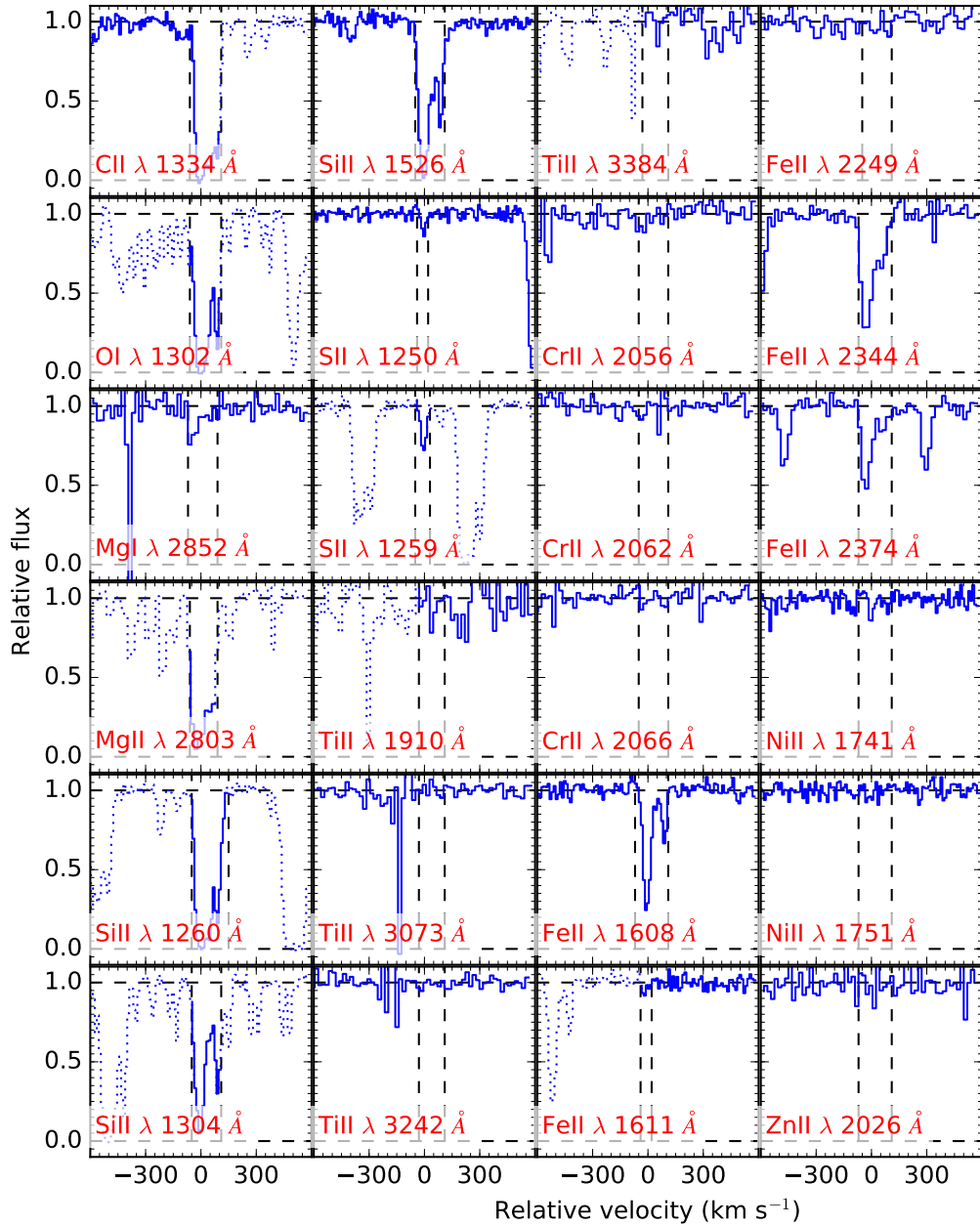


Figure A5. Velocity profile of the XQ100 spectrum towards J0034+1639 ($z_{\text{abs}}=4.283$).

Table A6. X-Shooter metal column densities for J0113–2803 ($z_{\text{abs}}=3.106$)

Ion	Line	λ Å	f	v_{min} km s $^{-1}$	v_{max} km s $^{-1}$	logN(X)	Included	logN $_{\text{adopt}}$
MgI	2852	2852.964	1.81E+00	-400	110	12.60 ± 0.06	Y	—
MgI								12.60 ± 0.06
MgII	2796	2796.352	6.12E-01	-550	110	> 14.42	Y	—
MgII	2803	2803.531	3.05E-01	-500	130	> 14.55	Y	—
MgII								> 14.55
SiII	1808	1808.013	2.19E-03	-400	110	15.60 ± 0.02	Y	—
SiII								15.60 ± 0.05
CaII	3934	3934.777	6.50E-01	-400	95	< 11.94	Y	—
CaII	3969	3969.591	3.22E-01	-400	95	< 12.35	N	—
CaII								< 11.94
TiII	1910	1910.750	2.02E-01	-400	90	< 12.61	Y	—
TiII	3073	3073.877	1.09E-01	-400	95	< 13.30	N	—
TiII	3242	3242.929	2.32E-01	-400	95	< 12.98	N	—
TiII								< 12.61
CrII	2056	2056.254	1.05E-01	-400	110	13.62 ± 0.04	Y	—
CrII	2062	2062.234	7.80E-02	-400	110	13.72 ± 0.06	Y	—
CrII	2066	2066.161	5.15E-02	-400	110	13.77 ± 0.06	Y	—
CrII								13.69 ± 0.09
MnII	2576	2576.877	3.51E-01	-400	110	13.00 ± 0.07	N	—
MnII	2594	2594.499	2.71E-01	-400	110	< 12.63	Y	—
MnII	2606	2606.462	1.93E-01	-400	110	13.21 ± 0.09	N	—
MnII								< 12.63
FeII	1608	1608.451	5.80E-02	-400	110	> 15.08	N	—
FeII	1611	1611.200	1.36E-03	-350	110	15.27 ± 0.06	N	—
FeII	2249	2249.877	1.82E-03	-400	110	15.29 ± 0.05	Y	—
FeII	2344	2344.214	1.14E-01	-400	110	> 14.91	N	—
FeII	2374	2374.461	3.13E-02	-400	110	> 15.06	N	—
FeII	2586	2586.650	6.91E-02	-400	110	> 14.92	N	—
FeII	2600	2600.173	2.39E-01	-400	110	> 14.42	N	—
FeII								15.29 ± 0.05
NiII	1709	1709.604	3.24E-02	-400	110	< 14.37	N	—
NiII	1741	1741.553	4.27E-02	-400	110	13.99 ± 0.04	Y	—
NiII	1751	1751.916	2.77E-02	-400	110	< 14.33	N	—
NiII								13.99 ± 0.05
ZnII	2026	2026.136	4.89E-01	-400	110	12.69 ± 0.05	Y	—
ZnII	2062	2062.664	2.56E-01	-400	110	13.21 ± 0.06	N	—
ZnII								12.69 ± 0.05

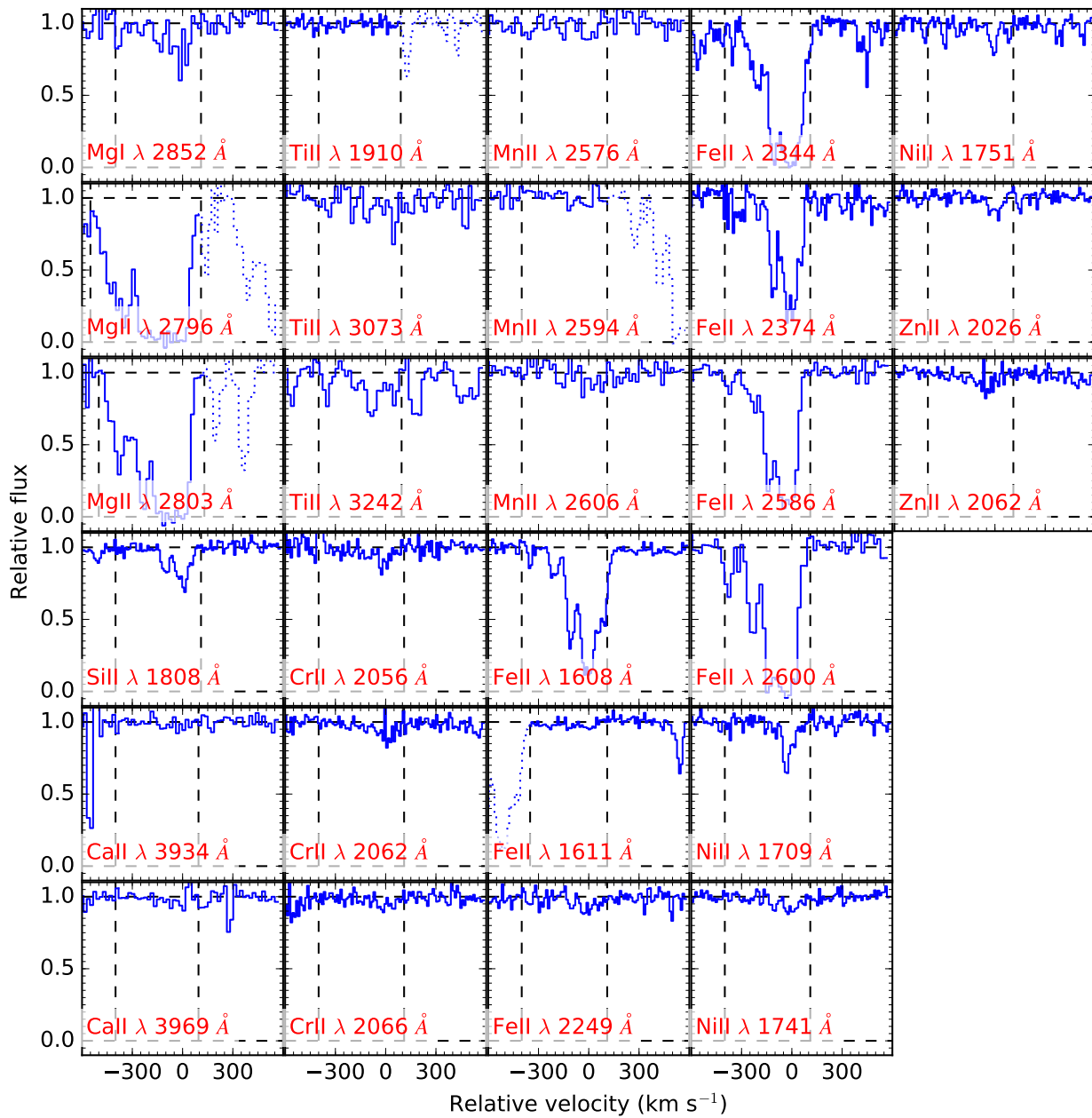


Figure A6. Velocity profile of the XQ100 spectrum towards J0113-2803 ($z_{\text{abs}}=3.106$).

Table A7. X-Shooter metal column densities for J0124+0044 ($z_{\text{abs}}=2.261$)

Ion	Line	λ Å	f	v_{min} km s $^{-1}$	v_{max} km s $^{-1}$	logN(X)	Included	logN _{adopt}
MgI	2852	2852.964	1.81E+00	-80	190	12.50 ± 0.02	Y	—
MgI								12.50 ± 0.05
MgII	2796	2796.352	6.12E-01	-80	190	> 14.00	N	—
MgII	2803	2803.531	3.05E-01	-80	190	> 14.31	Y	—
MgII								> 14.31
SiII	1808	1808.013	2.19E-03	-80	190	15.36 ± 0.02	Y	—
SiII								15.36 ± 0.05
CaII	3934	3934.777	6.50E-01	-80	190	< 11.94	Y	—
CaII	3969	3969.591	3.22E-01	-80	190	< 12.29	N	—
CaII								< 11.94
TiII	1910	1910.750	2.02E-01	-80	190	< 12.74	N	—
TiII	3242	3242.929	2.32E-01	-80	190	< 12.58	N	—
TiII	3384	3384.740	3.58E-01	-80	100	12.35 ± 0.08	Y	—
TiII								12.35 ± 0.08
CrII	2056	2056.254	1.05E-01	-80	190	13.38 ± 0.04	Y	—
CrII	2062	2062.234	7.80E-02	-80	190	13.39 ± 0.05	Y	—
CrII	2066	2066.161	5.15E-02	-80	190	13.44 ± 0.07	Y	—
CrII								13.40 ± 0.09
MnII	2576	2576.877	3.51E-01	-80	190	12.70 ± 0.05	Y	—
MnII	2594	2594.499	2.71E-01	-80	190	12.80 ± 0.06	Y	—
MnII	2606	2606.462	1.93E-01	-80	190	12.83 ± 0.07	Y	—
MnII								12.77 ± 0.11
FeII	2249	2249.877	1.82E-03	-80	190	14.96 ± 0.05	Y	—
FeII	2374	2374.461	3.13E-02	-80	190	> 14.77	N	—
FeII	2586	2586.650	6.91E-02	-80	190	> 14.56	N	—
FeII	2600	2600.173	2.39E-01	-100	190	> 14.11	N	—
FeII								14.96 ± 0.05
ZnII	2026	2026.136	4.89E-01	-80	190	12.66 ± 0.05	Y	—
ZnII	2062	2062.664	2.56E-01	-80	190	< 12.91	N	—
ZnII								12.66 ± 0.05

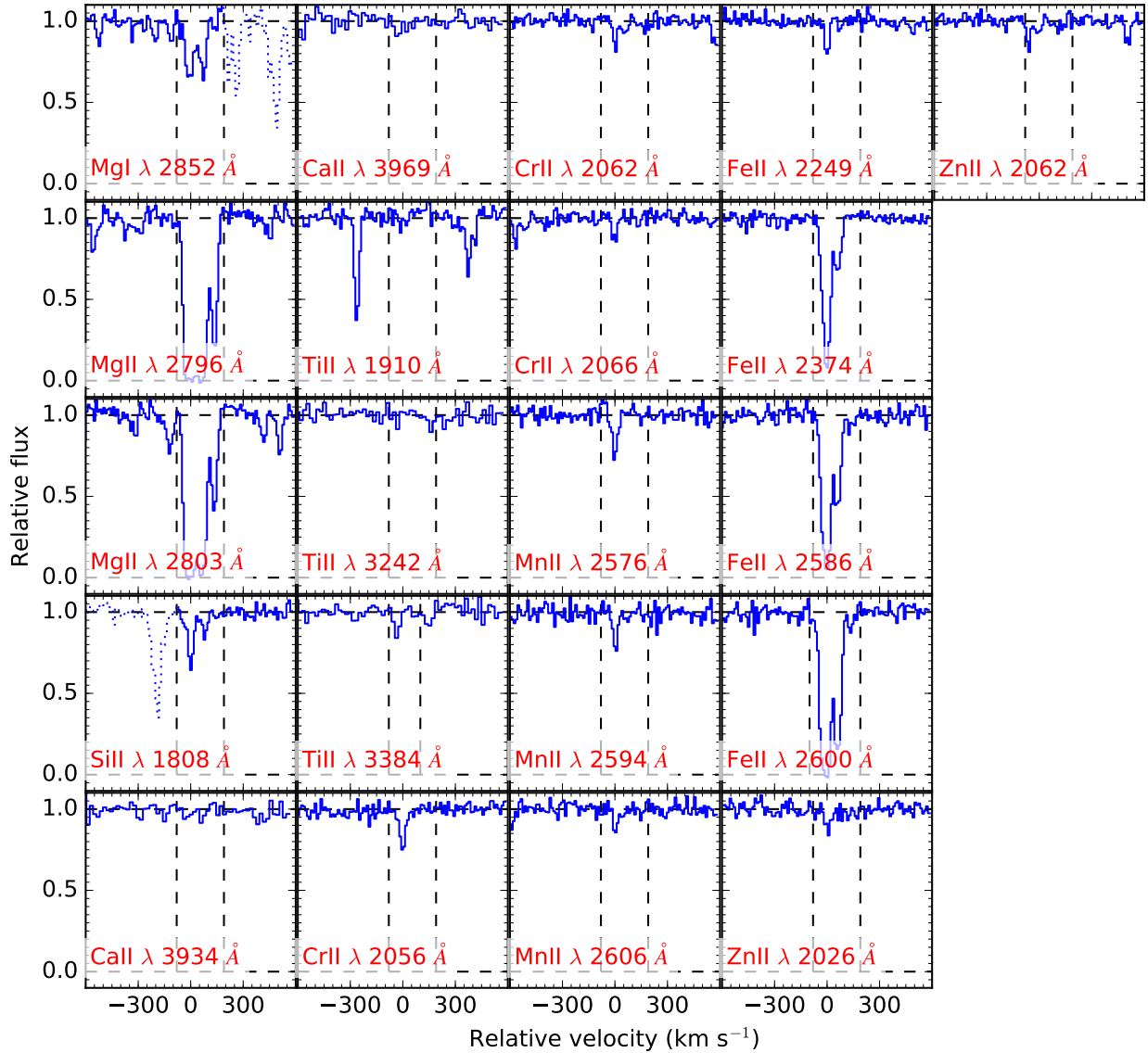


Figure A7. Velocity profile of the XQ100 spectrum towards J0124+0044 ($z_{\text{abs}}=2.261$).

Table A8. X-Shooter metal column densities for J0132+1341 ($z_{\text{abs}}=3.936$)

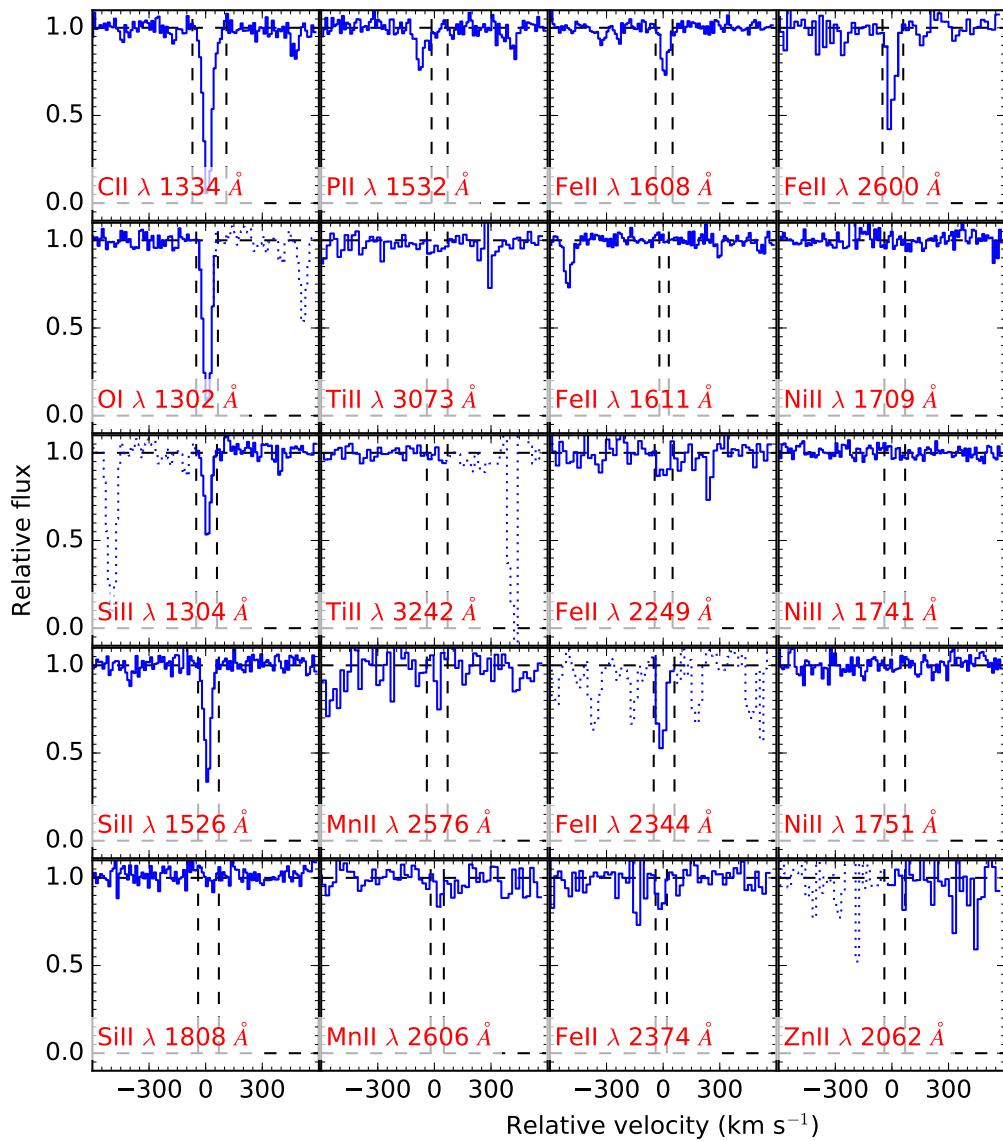


Figure A8. Velocity profile of the XQ100 spectrum towards J0132+1341 ($z_{\text{abs}}=3.936$).

Table A9. X-Shooter metal column densities for J0134+0400 ($z_{\text{abs}}=3.692$)

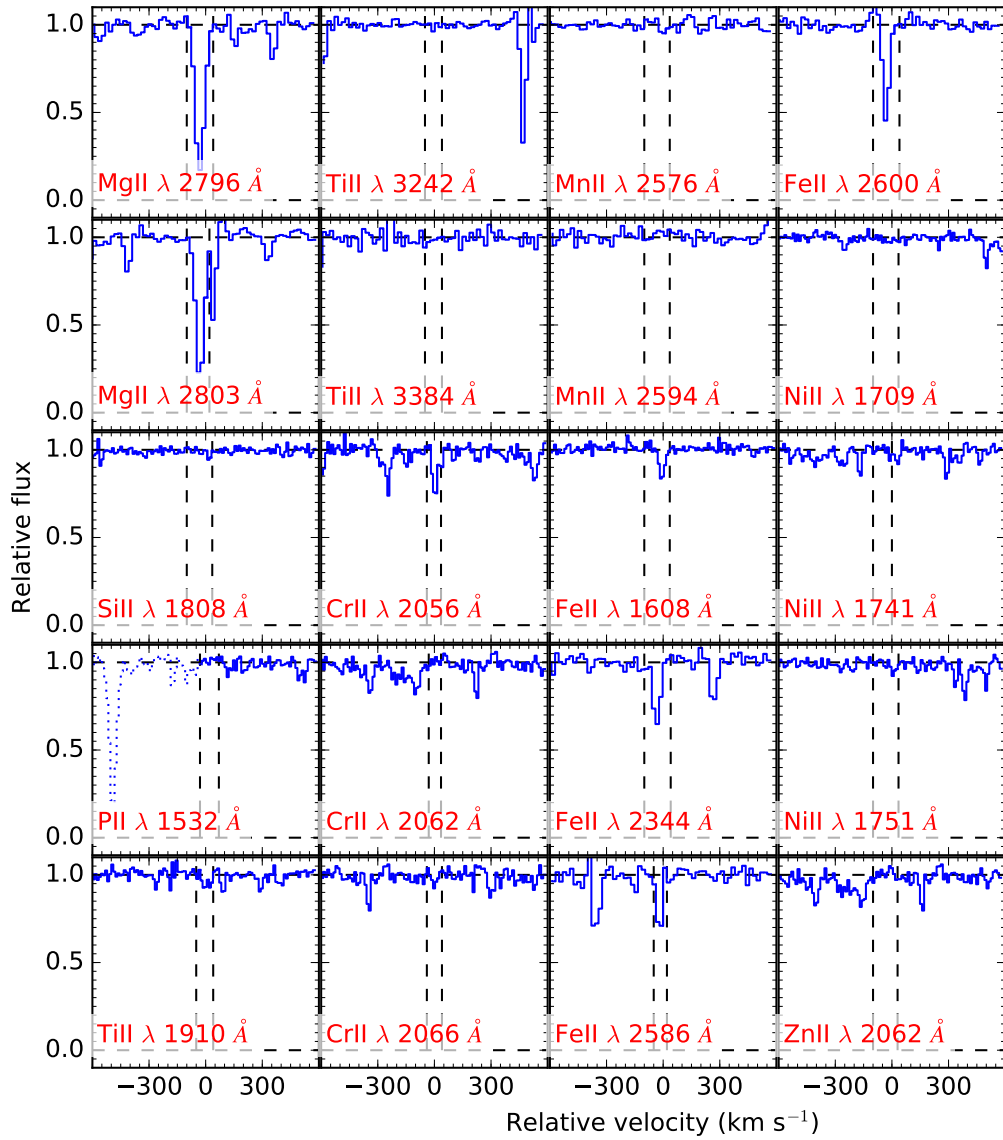


Figure A9. Velocity profile of the XQ100 spectrum towards J0134+0400 ($z_{\text{abs}}=3.692$).

Table A10. X-Shooter metal column densities for J0134+0400 ($z_{\text{abs}}=3.772$)

Ion	Line	λ Å	f	v_{min} km s $^{-1}$	v_{max} km s $^{-1}$	logN(X)	Included	logN _{adopt}
CII	1334	1334.532	1.28E-01	-160	150	> 15.21	Y	—
CII								> 15.21
MgII	2796	2796.352	6.12E-01	-170	230	> 14.15	N	—
MgII	2803	2803.531	3.05E-01	-200	230	> 14.38	Y	—
MgII								> 14.38
SiII	1526	1526.707	1.27E-01	-170	230	> 14.95	N	—
SiII	1808	1808.013	2.19E-03	-90	230	15.30 ± 0.02	Y	—
SiII								15.30 ± 0.05
PII	1532	1532.533	7.61E-03	-90	230	< 13.94	Y	—
PII								< 13.94
TiIII	3242	3242.929	2.32E-01	-100	230	< 12.33	N	—
TiIII	3384	3384.740	3.58E-01	-100	230	< 12.21	Y	—
TiIII								< 12.21
CrII	2056	2056.254	1.05E-01	-90	25	< 12.83	Y	—
CrII								< 12.83
MnII	2576	2576.877	3.51E-01	-100	230	< 12.39	Y	—
MnII	2594	2594.499	2.71E-01	-100	230	< 12.50	Y	—
MnII	2606	2606.462	1.93E-01	-100	230	< 12.59	Y	—
MnII								< 12.39
FeII	1608	1608.451	5.80E-02	-70	230	> 14.93	N	—
FeII	1611	1611.200	1.36E-03	-90	230	< 15.57	N	—
FeII	2249	2249.877	1.82E-03	-90	230	14.97 ± 0.07	Y	—
FeII	2374	2374.461	3.13E-02	-160	230	> 15.04	N	—
FeII	2586	2586.650	6.91E-02	-160	230	> 14.75	N	—
FeII	2600	2600.173	2.39E-01	-160	230	> 14.55	N	—
FeII								14.97 ± 0.07
NiIII	1709	1709.604	3.24E-02	-100	230	13.99 ± 0.03	N	—
NiIII	1741	1741.553	4.27E-02	-100	230	13.85 ± 0.03	Y	—
NiIII	1751	1751.916	2.77E-02	-100	230	13.80 ± 0.05	Y	—
NiIII								13.84 ± 0.06
ZnII	2026	2026.136	4.89E-01	-100	230	12.88 ± 0.04	Y	—
ZnII								12.88 ± 0.05

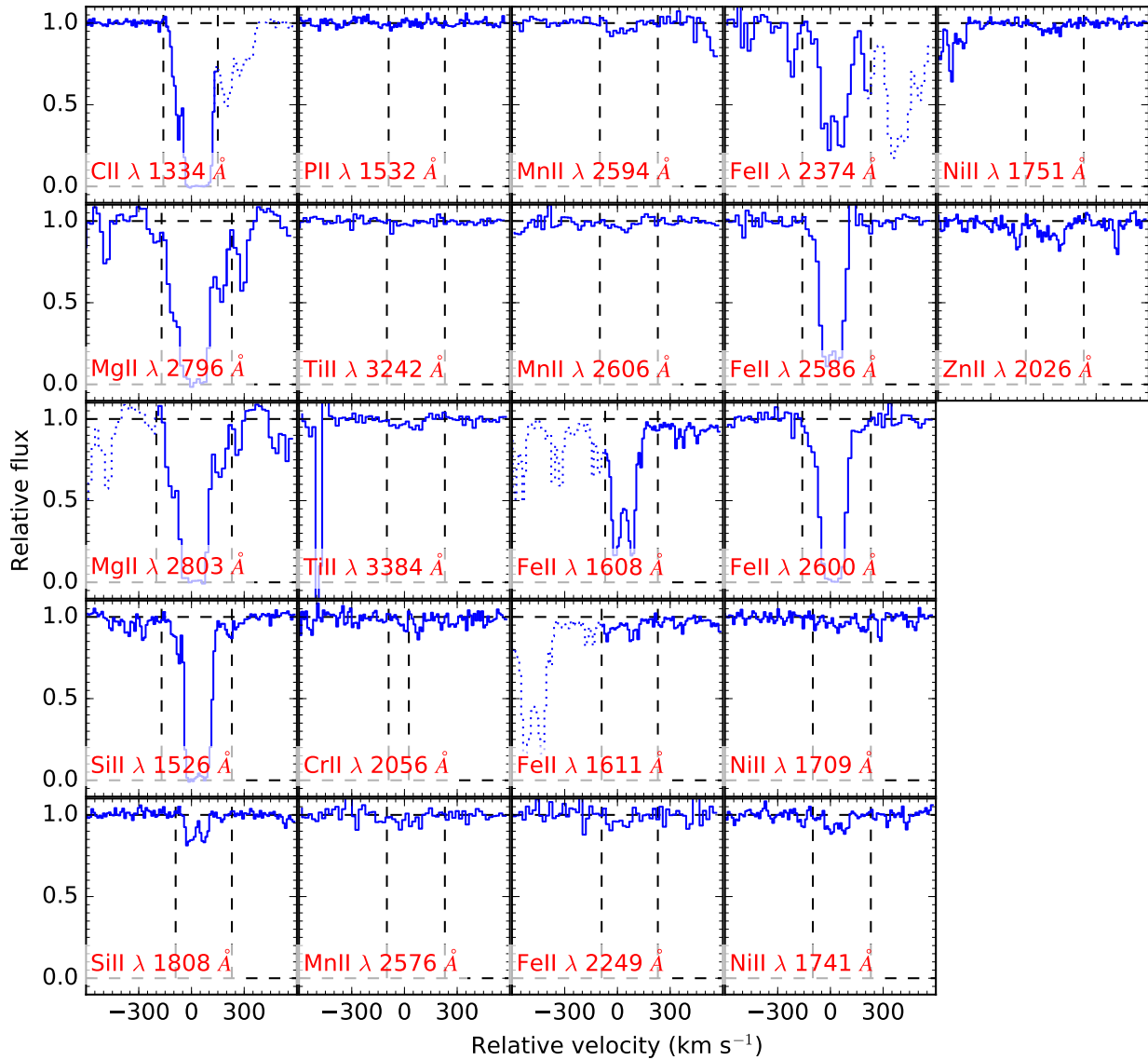


Figure A10. Velocity profile of the XQ100 spectrum towards J0134+0400 ($z_{\text{abs}}=3.772$).

Table A11. X-Shooter metal column densities for J0234–1806 ($z_{\text{abs}}=3.693$)

Ion	Line	λ Å	f	v_{min} km s $^{-1}$	v_{max} km s $^{-1}$	logN(X)	Included	logN _{adopt}
MgI	2852	2852.964	1.81E+00	-200	200	12.67 ± 0.02	Y	—
MgI								12.67 ± 0.05
MgII	2796	2796.352	6.12E-01	-200	330	> 14.04	N	—
MgII	2803	2803.531	3.05E-01	-175	330	> 14.30	Y	—
MgII								> 14.30
SiII	1526	1526.707	1.27E-01	-200	330	> 14.55	Y	—
SiII	1808	1808.013	2.19E-03	-200	330	< 14.62	Y	—
SiII								14.54–14.64
TiII	3242	3242.929	2.32E-01	-200	330	< 12.47	N	—
TiII	3384	3384.740	3.58E-01	-200	330	< 12.44	Y	—
TiII								< 12.44
CrII	2056	2056.254	1.05E-01	0	330	< 13.11	Y	—
CrII	2062	2062.234	7.80E-02	-150	90	< 13.20	N	—
CrII	2066	2066.161	5.15E-02	-200	330	< 14.35	N	—
CrII								< 13.11
MnII	2576	2576.877	3.51E-01	-200	330	< 12.62	Y	—
MnII	2594	2594.499	2.71E-01	-130	330	< 12.81	N	—
MnII								< 12.62
FeII	1608	1608.451	5.80E-02	-200	330	14.27 ± 0.02	Y	—
FeII	1611	1611.200	1.36E-03	-200	330	15.24 ± 0.09	N	—
FeII	2249	2249.877	1.82E-03	-200	330	14.97 ± 0.14	N	—
FeII	2344	2344.214	1.14E-01	-200	330	14.18 ± 0.03	Y	—
FeII	2600	2600.173	2.39E-01	-200	330	> 14.03	N	—
FeII								14.24 ± 0.05
NiII	1709	1709.604	3.24E-02	-200	330	< 13.59	Y	—
NiII	1751	1751.916	2.77E-02	-200	100	< 13.62	N	—
NiII								< 13.59

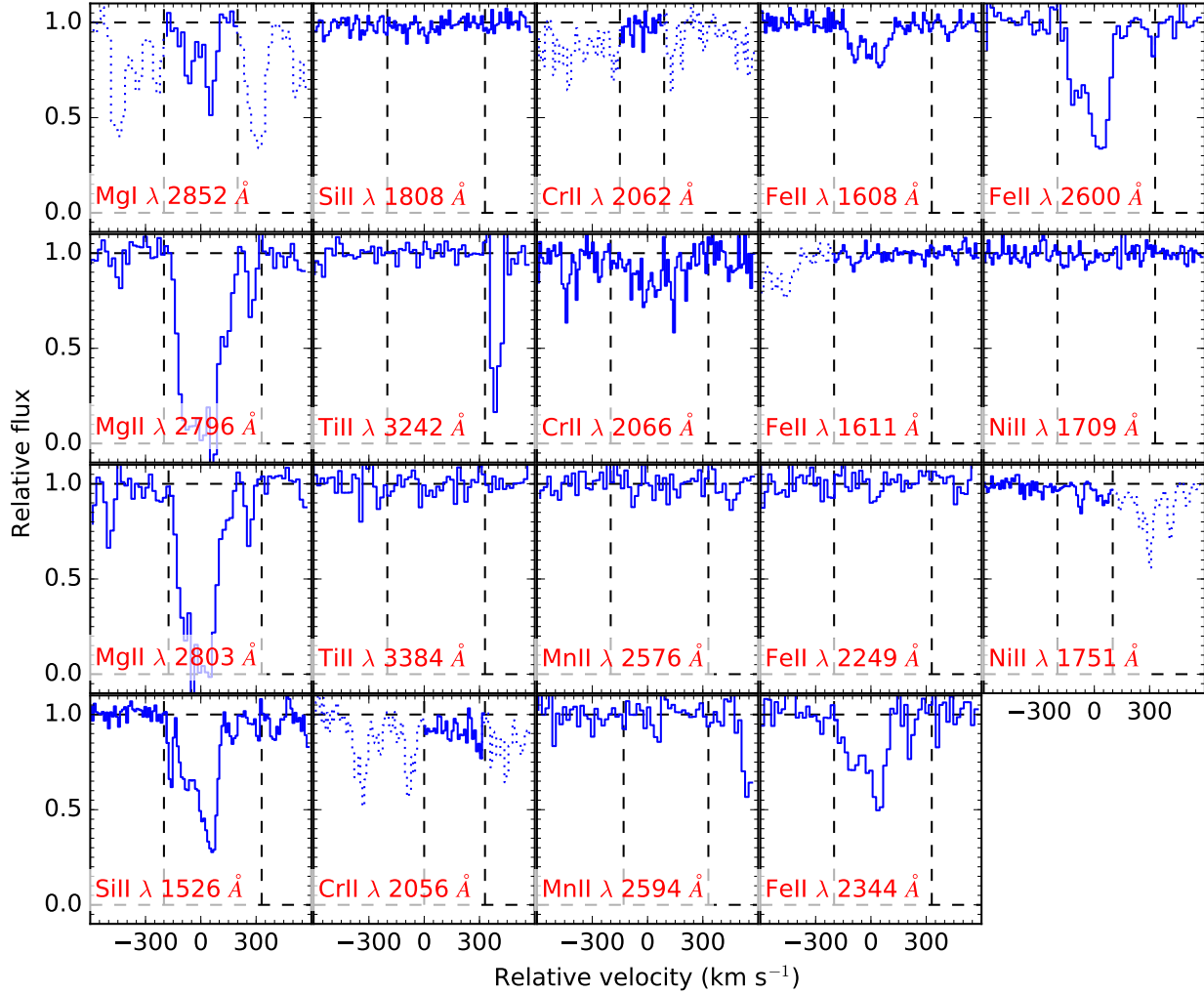


Figure A11. Velocity profile of the XQ100 spectrum towards J0234-1806 ($z_{\text{abs}}=3.693$).

Table A12. X-Shooter metal column densities for J0255+0048 ($z_{\text{abs}} = 3.256$)

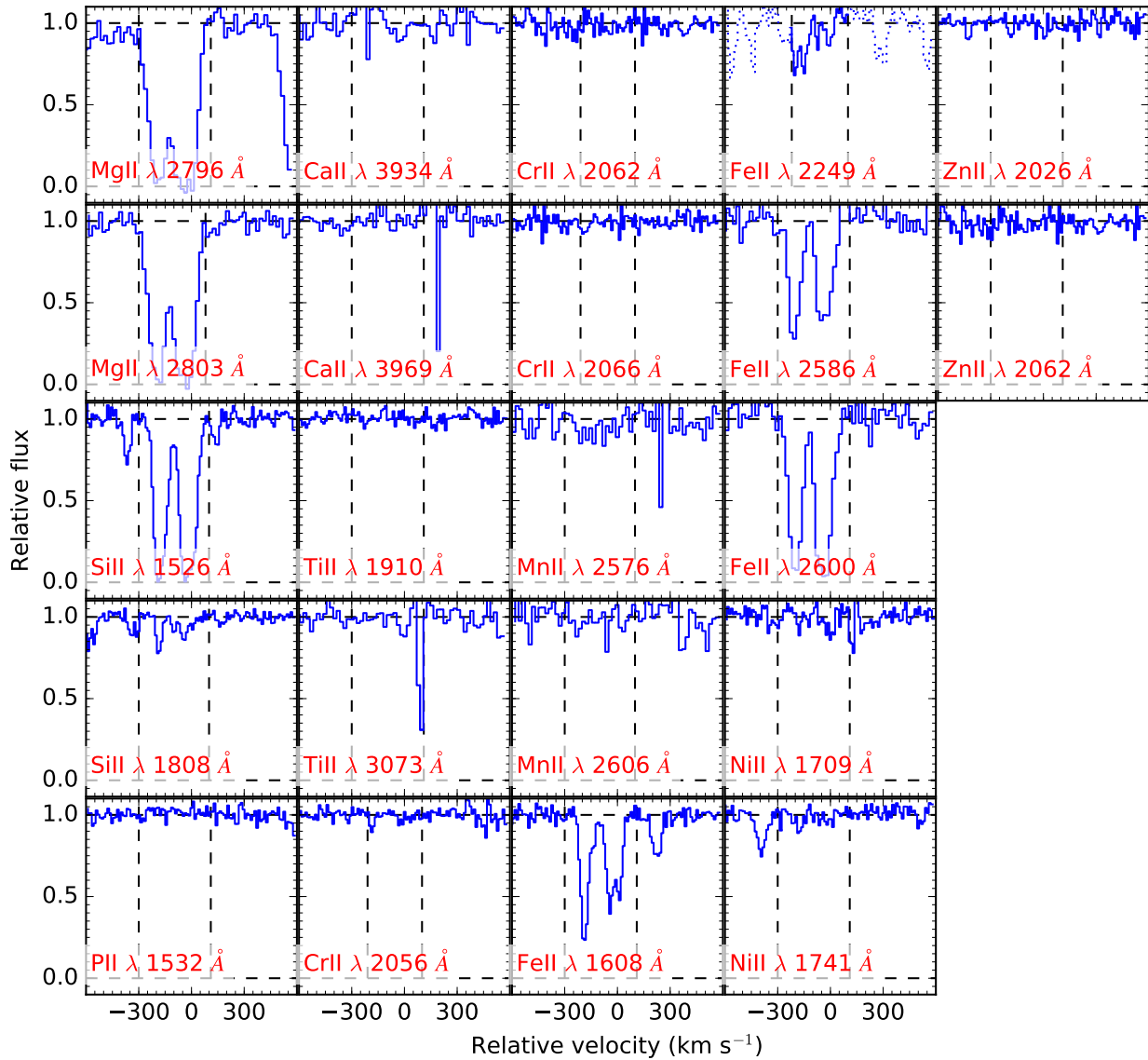


Figure A12. Velocity profile of the XQ100 spectrum towards J0255+0048 ($z_{\text{abs}}=3.256$).

Table A13. X-Shooter metal column densities for J0255+0048 ($z_{\text{abs}}=3.914$)

Ion	Line	λ Å	f	v_{min} km s $^{-1}$	v_{max} km s $^{-1}$	logN(X)	Included	logN $_{\text{adopt}}$
CII	1334	1334.532	1.28E-01	-70	70	> 14.55	Y	—
CII								> 14.55
OI	1302	1302.168	4.89E-02	-70	70	> 14.95	Y	—
OI								> 14.95
SiII	1260	1260.422	1.01E+00	-70	90	> 13.61	N	—
SiII	1304	1304.370	9.40E-02	-70	90	> 14.58	N	—
SiII	1526	1526.707	1.27E-01	-70	90	> 14.51	N	—
SiII	1808	1808.013	2.19E-03	-70	45	15.02 ± 0.05	Y	—
SiII								15.02 ± 0.05
PII	1532	1532.533	7.61E-03	-70	90	< 14.20	Y	—
PII								< 14.20
SII	1250	1250.584	5.43E-03	-70	70	14.87 ± 0.03	Y	—
SII	1253	1253.811	1.09E-02	-70	90	14.66 ± 0.03	Y	—
SII	1259	1259.519	1.66E-02	-70	90	14.70 ± 0.02	Y	—
SII								14.73 ± 0.05
TiII	1910	1910.750	2.02E-01	-70	90	< 13.51	N	—
TiII	3073	3073.877	1.09E-01	-70	90	< 12.91	N	—
TiII	3242	3242.929	2.32E-01	-70	90	< 12.33	Y	—
TiII	3384	3384.740	3.58E-01	-70	90	< 12.40	N	—
TiII								< 12.33
MnII	2576	2576.877	3.51E-01	-70	90	< 12.80	Y	—
MnII	2594	2594.499	2.71E-01	-70	90	< 13.13	N	—
MnII								< 12.80
FeII	1144	1144.938	1.06E-01	-70	90	> 14.49	N	—
FeII	1608	1608.451	5.80E-02	-70	90	> 14.51	Y	—
FeII	1611	1611.200	1.36E-03	-70	90	< 14.83	Y	—
FeII	2249	2249.877	1.82E-03	-70	90	< 16.19	N	—
FeII	2344	2344.214	1.14E-01	-70	90	> 14.15	N	—
FeII	2374	2374.461	3.13E-02	-70	90	> 14.50	Y	—
FeII	2586	2586.650	6.91E-02	-70	90	> 14.30	N	—
FeII	2600	2600.173	2.39E-01	-70	90	> 13.65	N	—
FeII								14.51–14.83
NiII	1709	1709.604	3.24E-02	-70	90	< 13.89	N	—
NiII	1741	1741.553	4.27E-02	-70	90	13.52 ± 0.08	Y	—
NiII	1751	1751.916	2.77E-02	-70	90	13.46 ± 0.12	Y	—
NiII								13.50 ± 0.14

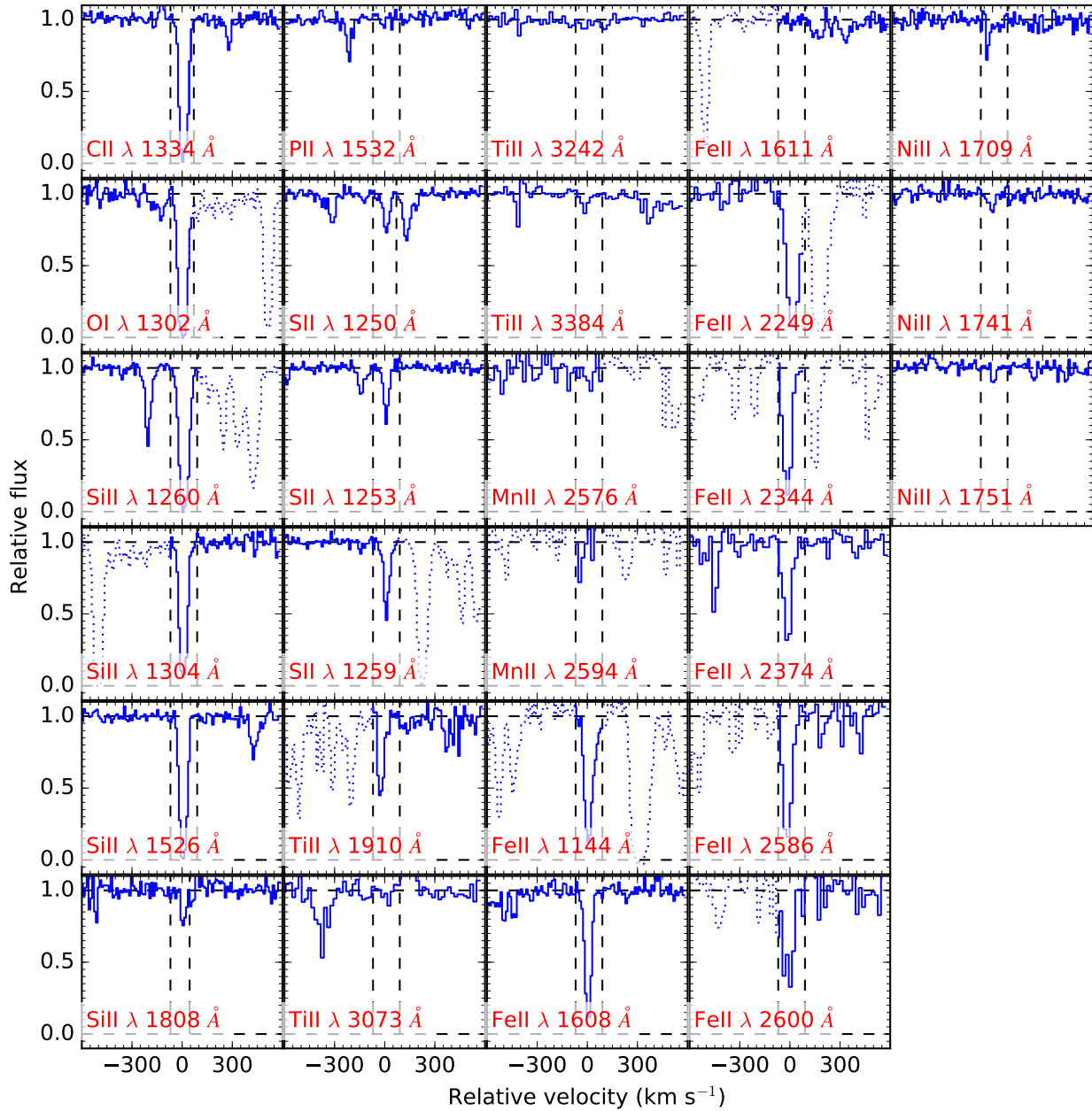


Figure A13. Velocity profile of the XQ100 spectrum towards J0255+0048 ($z_{\text{abs}}=3.914$).

Table A14. X-Shooter metal column densities for J0307-4945 ($z_{\text{abs}}=3.591$)

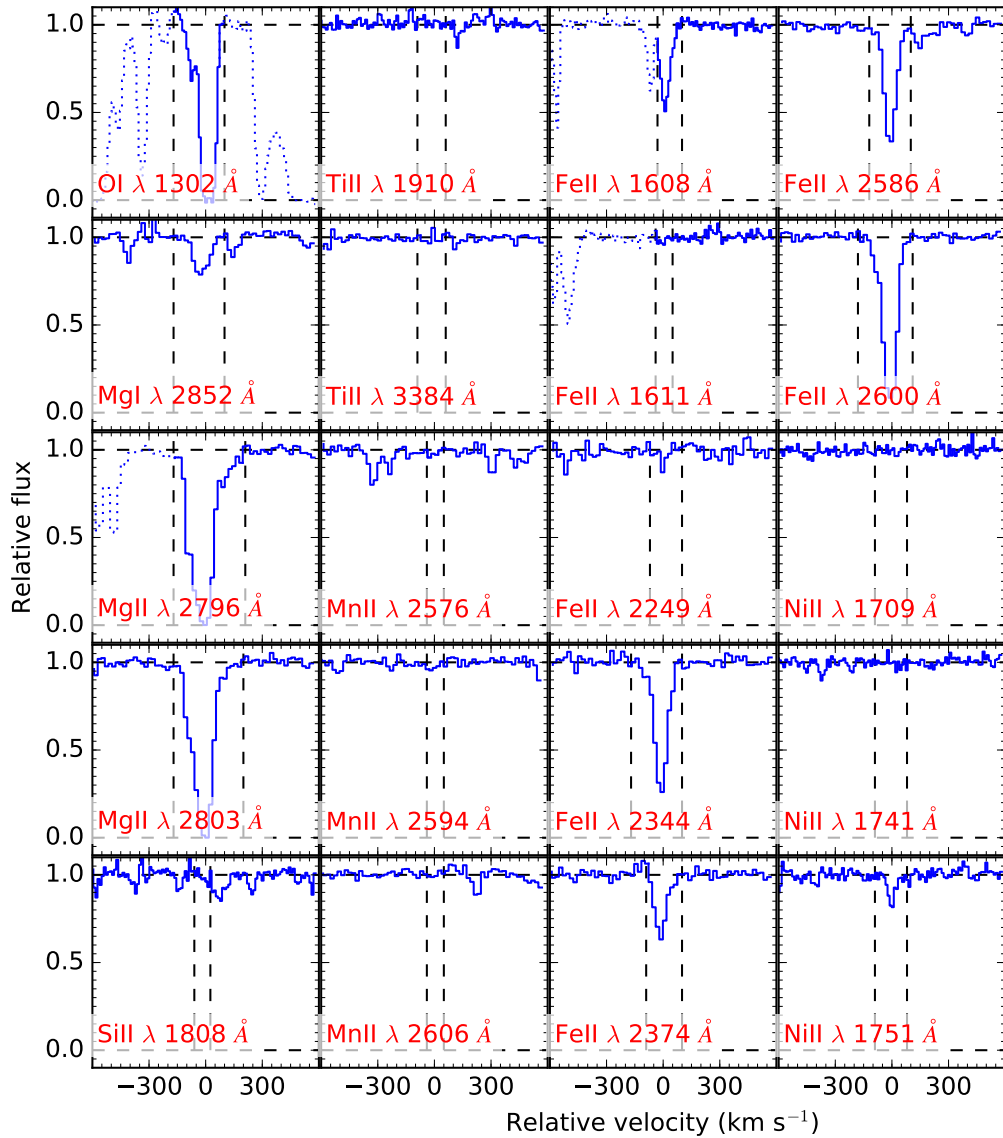


Figure A14. Velocity profile of the XQ100 spectrum towards J0307-4945 ($z_{\text{abs}}=3.591$).

Table A15. X-Shooter metal column densities for J0307–4945 ($z_{\text{abs}}=4.466$)

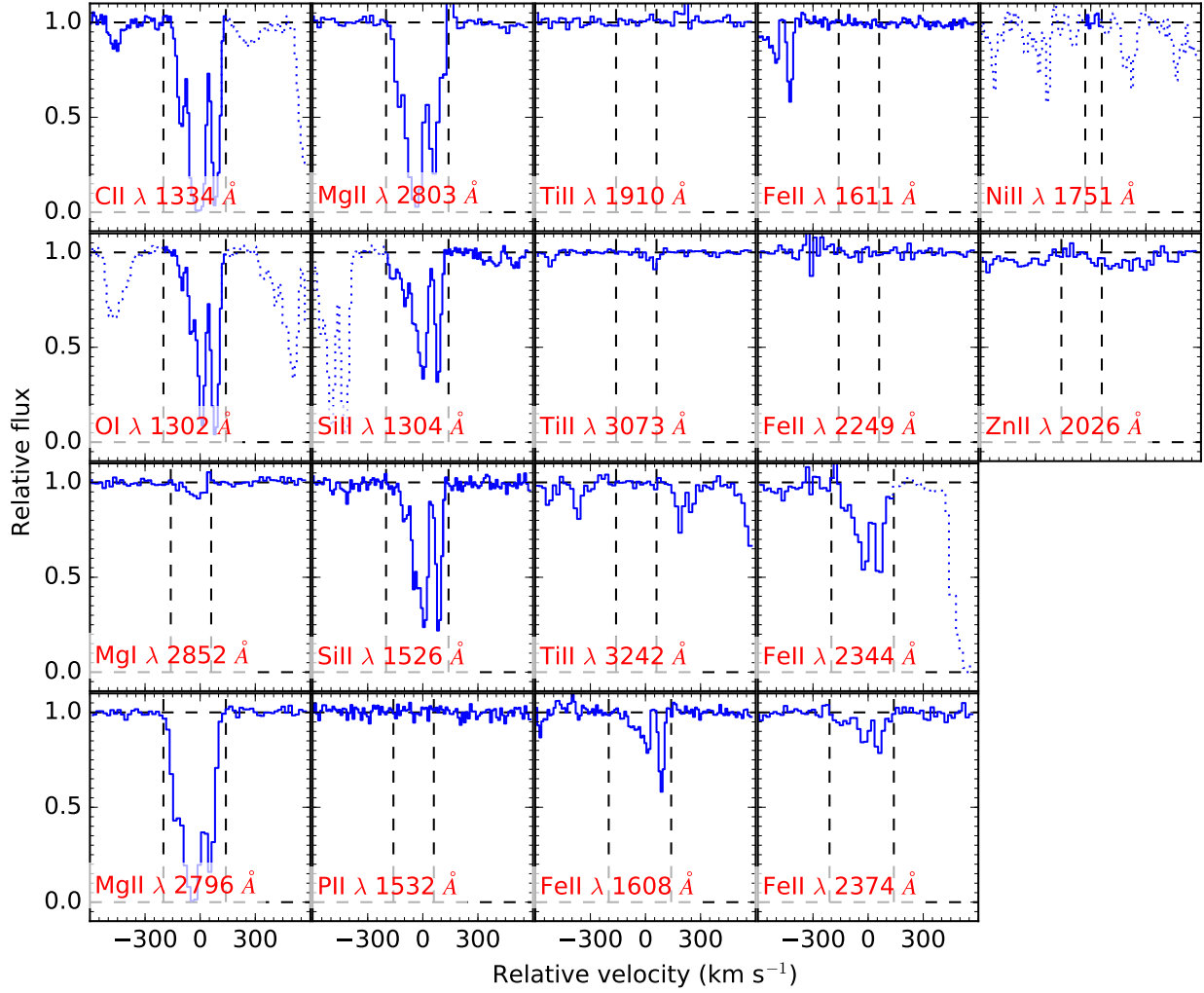


Figure A15. Velocity profile of the XQ100 spectrum towards J0307-4945 ($z_{\text{abs}}=4.466$).

Table A16. X-Shooter metal column densities for J0415–4357 ($z_{\text{abs}}=3.808$)

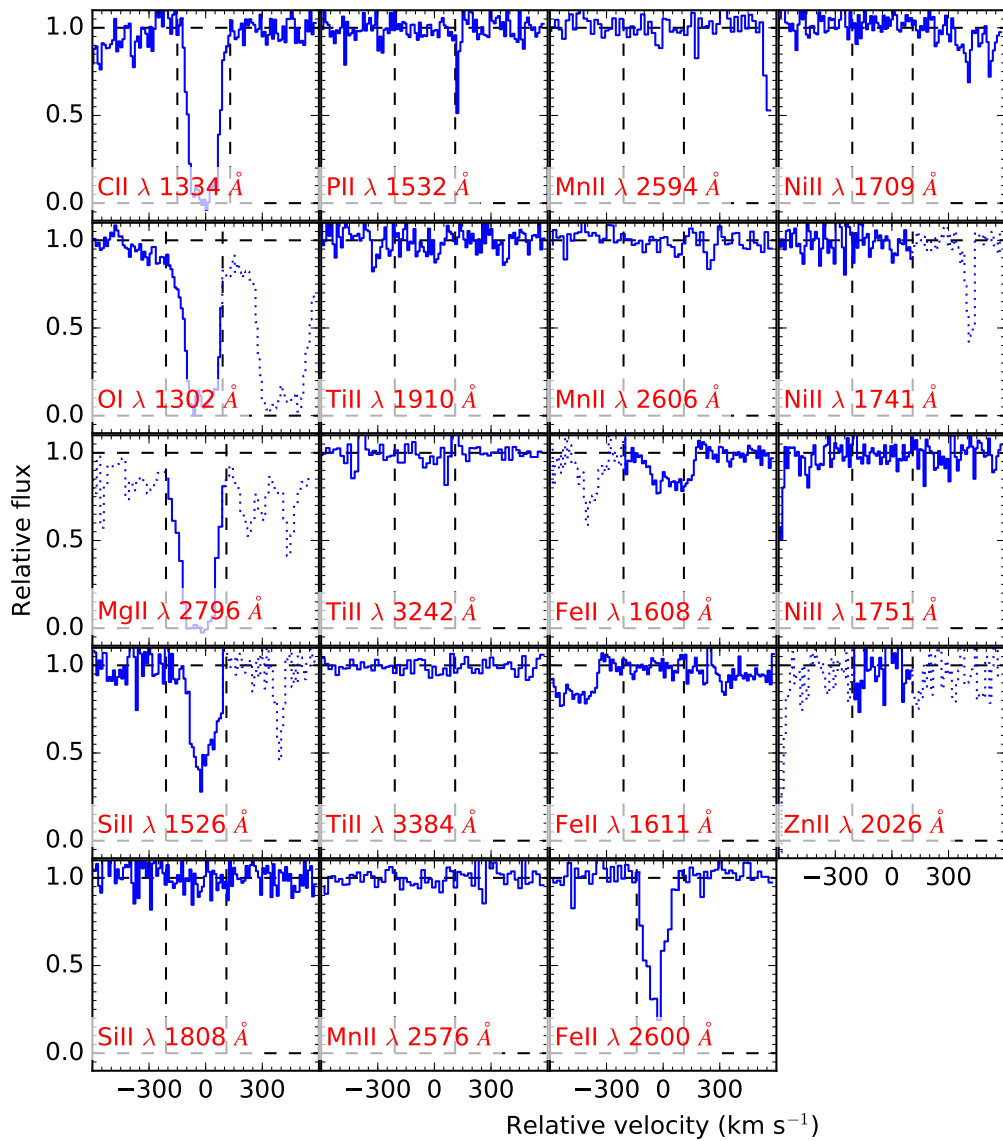


Figure A16. Velocity profile of the XQ100 spectrum towards J0415-4357 ($z_{\text{abs}} = 3.808$).

Table A17. X-Shooter metal column densities for J0424–2209 ($z_{\text{abs}}=2.982$)

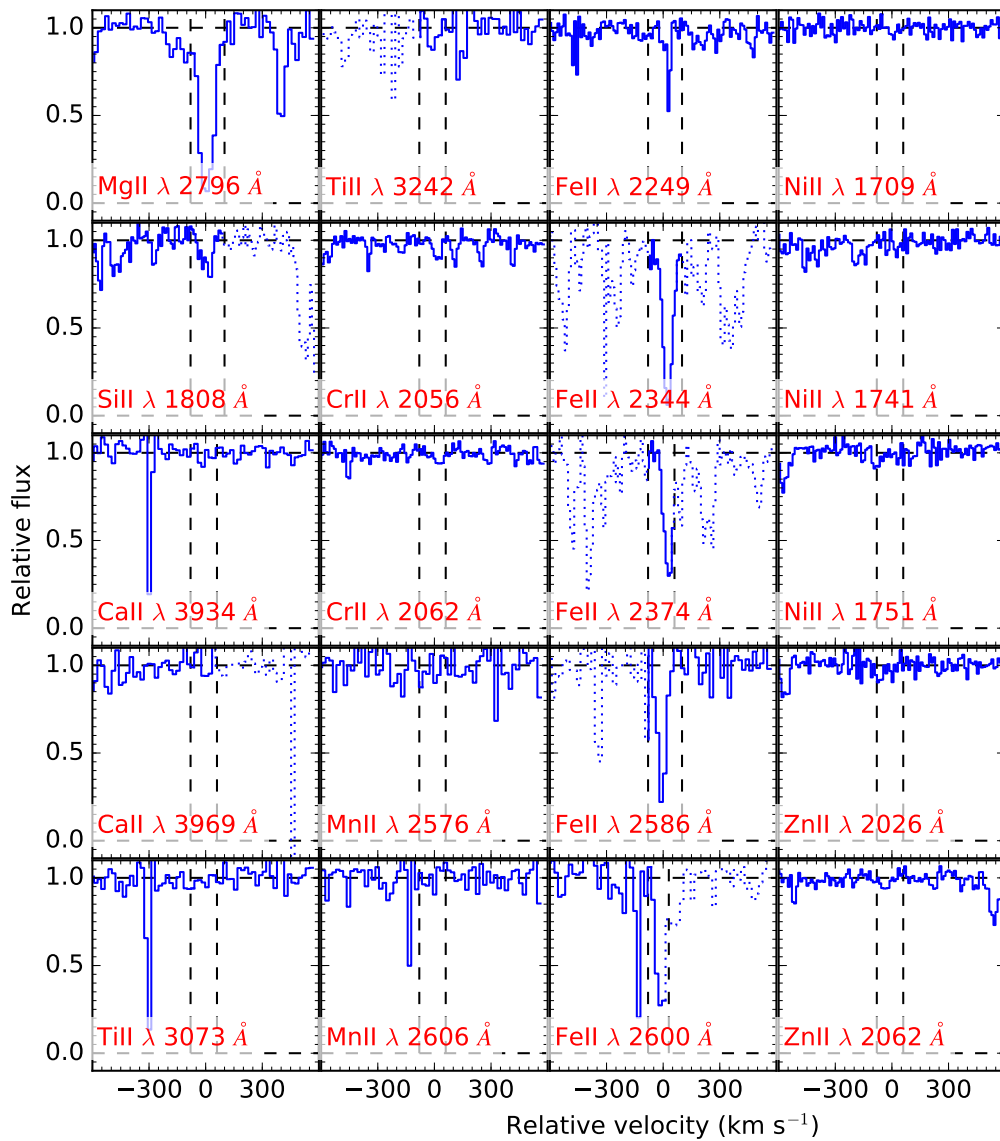


Figure A17. Velocity profile of the XQ100 spectrum towards J0424-2209 ($z_{\text{abs}}=2.982$).

Table A18. X-Shooter metal column densities for J0529–3552 ($z_{\text{abs}}=3.684$)

Ion	Line	λ Å	f	v_{min} km s $^{-1}$	v_{max} km s $^{-1}$	$\log N(X)$	Included	$\log N_{\text{adopt}}$
MgII	2796	2796.352	6.12E-01	-80	50	13.09 ± 0.03	Y	—
MgII	2803	2803.531	3.05E-01	-80	50	13.08 ± 0.07	Y	—
MgII								13.08 ± 0.08
SIII	1526	1526.707	1.27E-01	-80	50	13.53 ± 0.05	Y	—
SIII								13.53 ± 0.05
FeII	1608	1608.451	5.80E-02	-80	50	< 13.80	Y	—
FeII								< 13.80

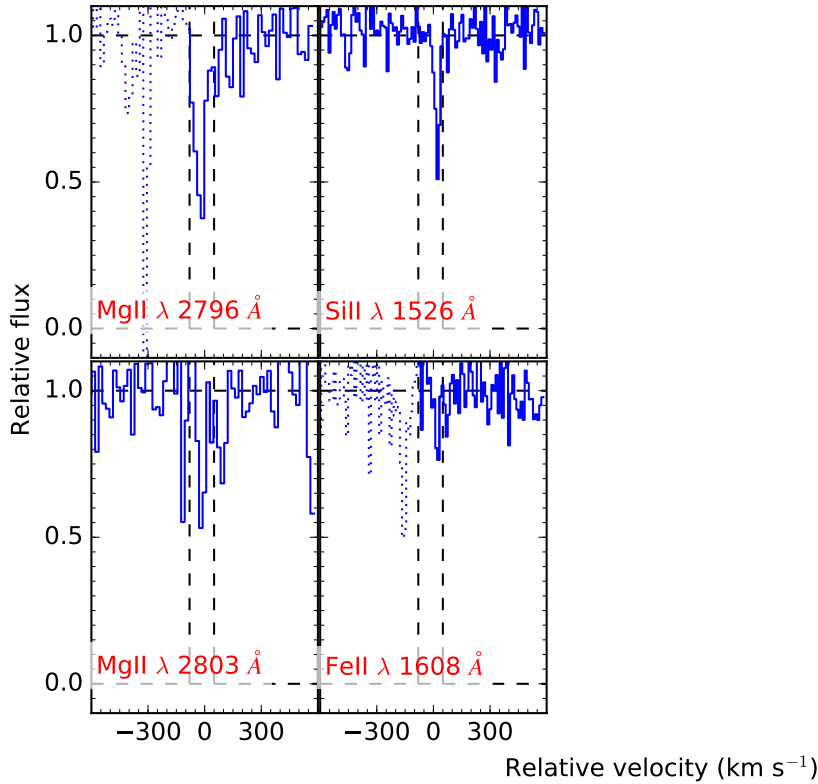
**Figure A18.** Velocity profile of the XQ100 spectrum towards J0529-3552 ($z_{\text{abs}}=3.684$).

Table A19. X-Shooter metal column densities for J0747+2739 ($z_{\text{abs}}=3.424$)

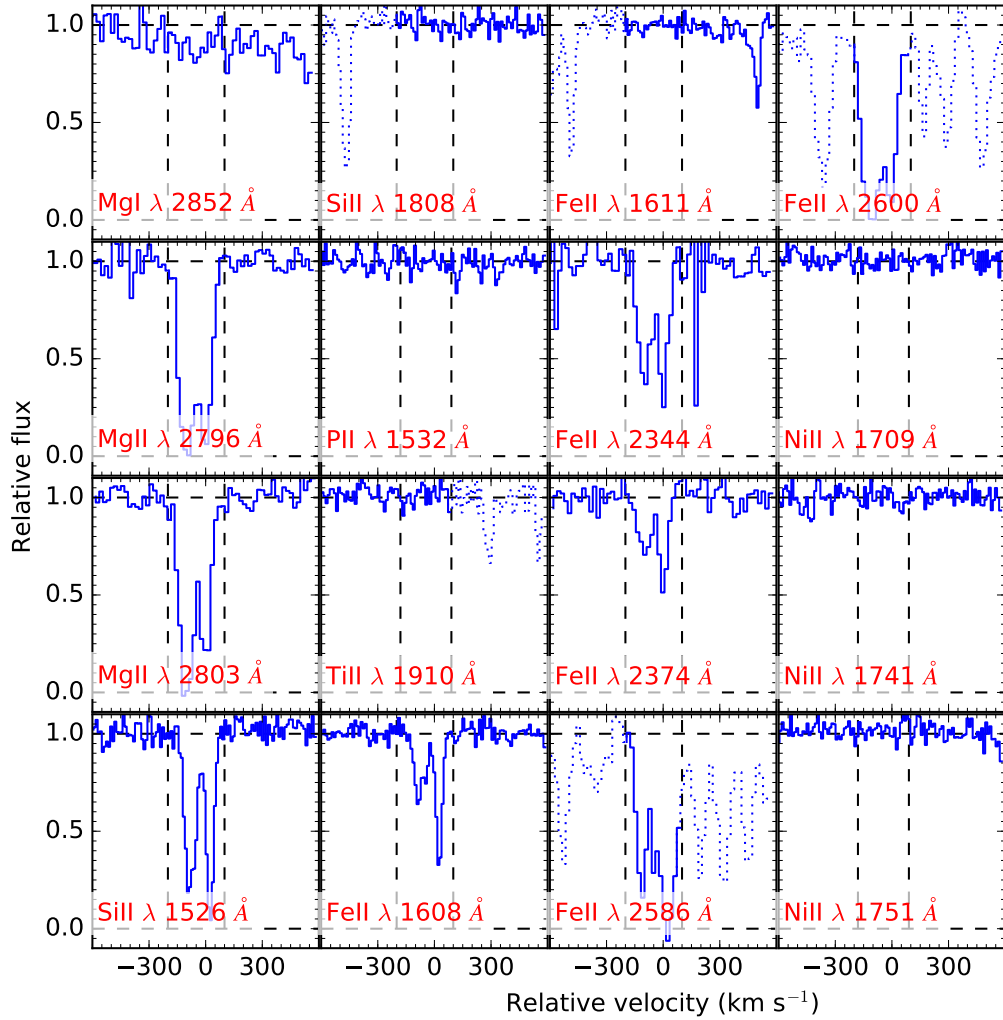


Figure A19. Velocity profile of the XQ100 spectrum towards J0747+2739 ($z_{\text{abs}}=3.424$).

Table A20. X-Shooter metal column densities for J0747+2739 ($z_{\text{abs}}=3.901$)

Ion	Line	λ Å	f	v_{min} km s $^{-1}$	v_{max} km s $^{-1}$	logN(X)	Included	logN $_{\text{adopt}}$
CII	1036	1036.337	1.23E-01	-220	50	14.31 ± 0.02	Y	—
CII	1334	1334.532	1.28E-01	-220	50	> 14.54	N	—
CII								14.31 ± 0.05
OI	1302	1302.168	4.89E-02	-220	50	> 14.90	Y	—
OI								> 14.90
SiII	1304	1304.370	9.40E-02	-220	50	14.07 ± 0.02	Y	—
SiII	1526	1526.707	1.27E-01	-220	50	14.08 ± 0.02	Y	—
SiII	1808	1808.013	2.19E-03	-220	50	14.98 ± 0.08	N	—
SiII								14.08 ± 0.05
TiIII	3073	3073.877	1.09E-01	-100	25	< 12.89	N	—
TiIII	3242	3242.929	2.32E-01	-220	50	< 12.43	N	—
TiIII	3384	3384.740	3.58E-01	-220	50	< 12.35	Y	—
TiIII								< 12.35
MnII	2576	2576.877	3.51E-01	-220	50	< 12.74	Y	—
MnII	2594	2594.499	2.71E-01	-220	-30	< 12.62	N	—
MnII	2606	2606.462	1.93E-01	-220	50	< 13.12	N	—
MnII								< 12.74
FeII	1608	1608.451	5.80E-02	-220	50	14.01 ± 0.03	Y	—
FeII	1611	1611.200	1.36E-03	-220	50	< 14.98	N	—
FeII	2249	2249.877	1.82E-03	-100	50	< 15.00	N	—
FeII	2344	2344.214	1.14E-01	-220	50	< 14.27	N	—
FeII	2374	2374.461	3.13E-02	-220	50	14.03 ± 0.00	Y	—
FeII	2586	2586.650	6.91E-02	-220	50	14.07 ± 0.00	Y	—
FeII	2600	2600.173	2.39E-01	-220	50	> 13.73	N	—
FeII								14.06 ± 0.05
NiII	1709	1709.604	3.24E-02	-220	50	< 13.60	N	—
NiII	1741	1741.553	4.27E-02	-220	50	< 13.45	Y	—
NiII								< 13.45

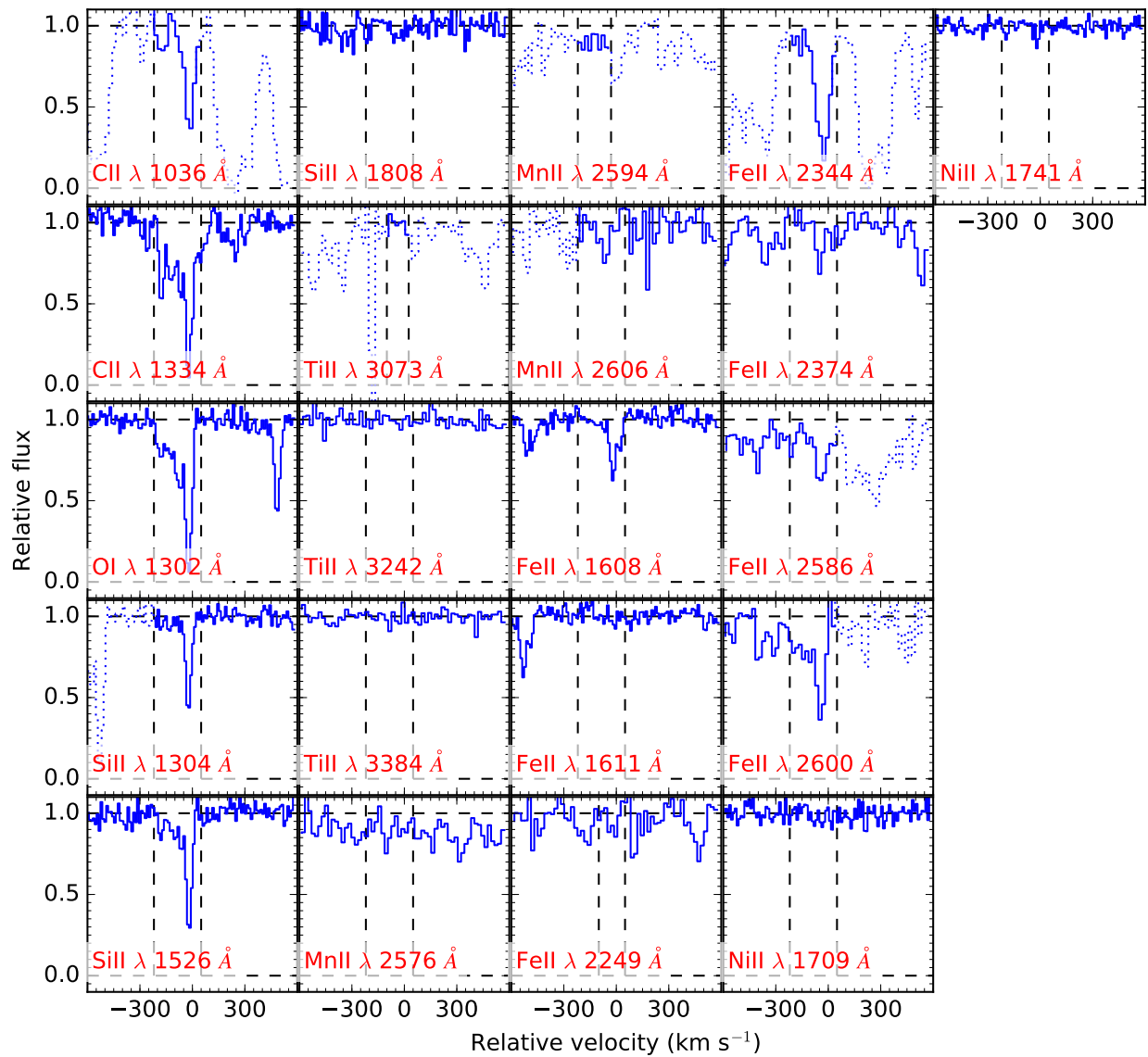


Figure A20. Velocity profile of the XQ100 spectrum towards J0747+2739 ($z_{\text{abs}}=3.901$).

Table A21. X-Shooter metal column densities for J0800+1920 ($z_{\text{abs}}=3.946$)

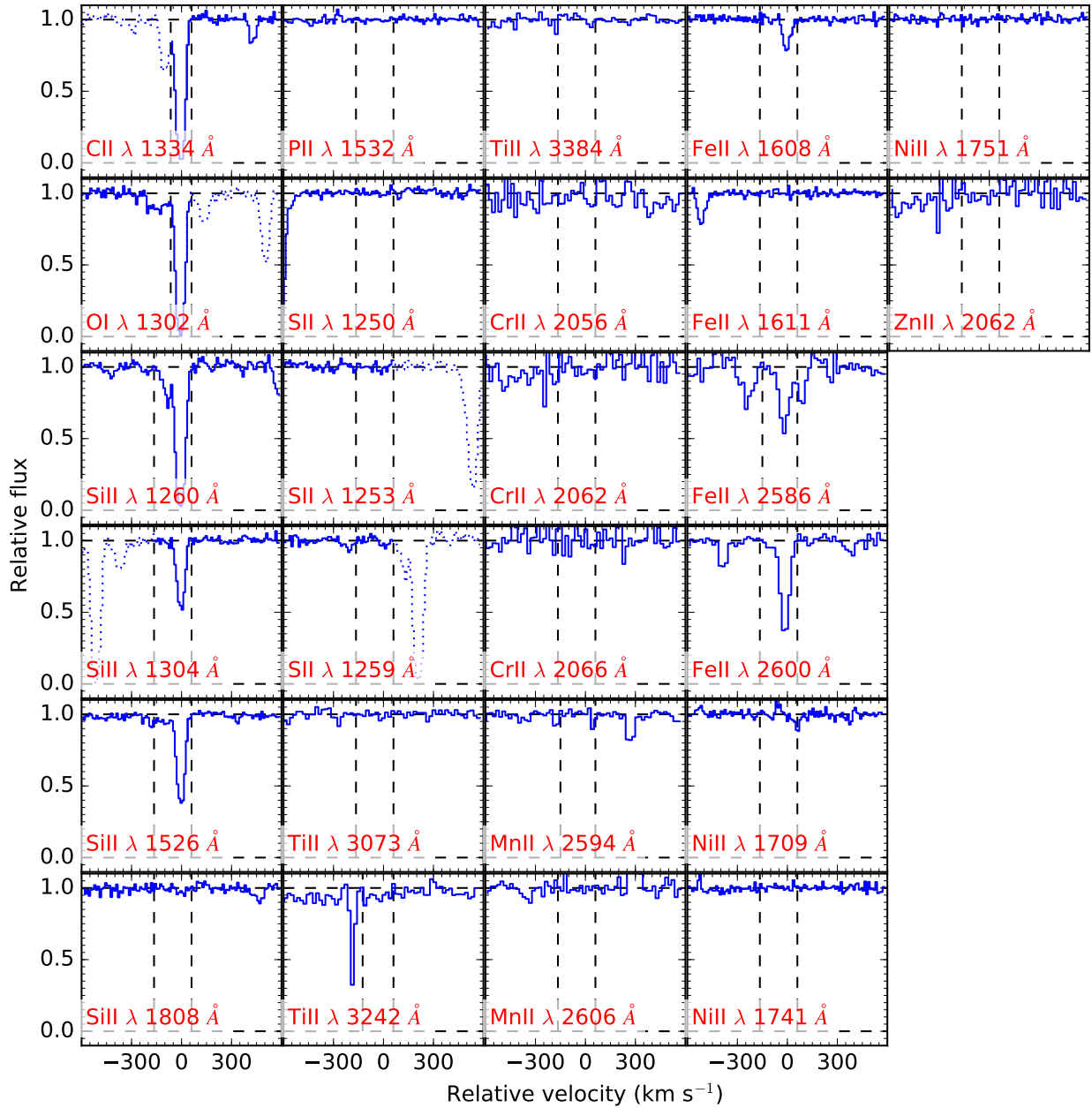


Figure A21. Velocity profile of the XQ100 spectrum towards J0800+1920 ($z_{\text{abs}}=3.946$).

Table A22. X-Shooter metal column densities for J0818+0958 ($z_{\text{abs}}=3.306$)

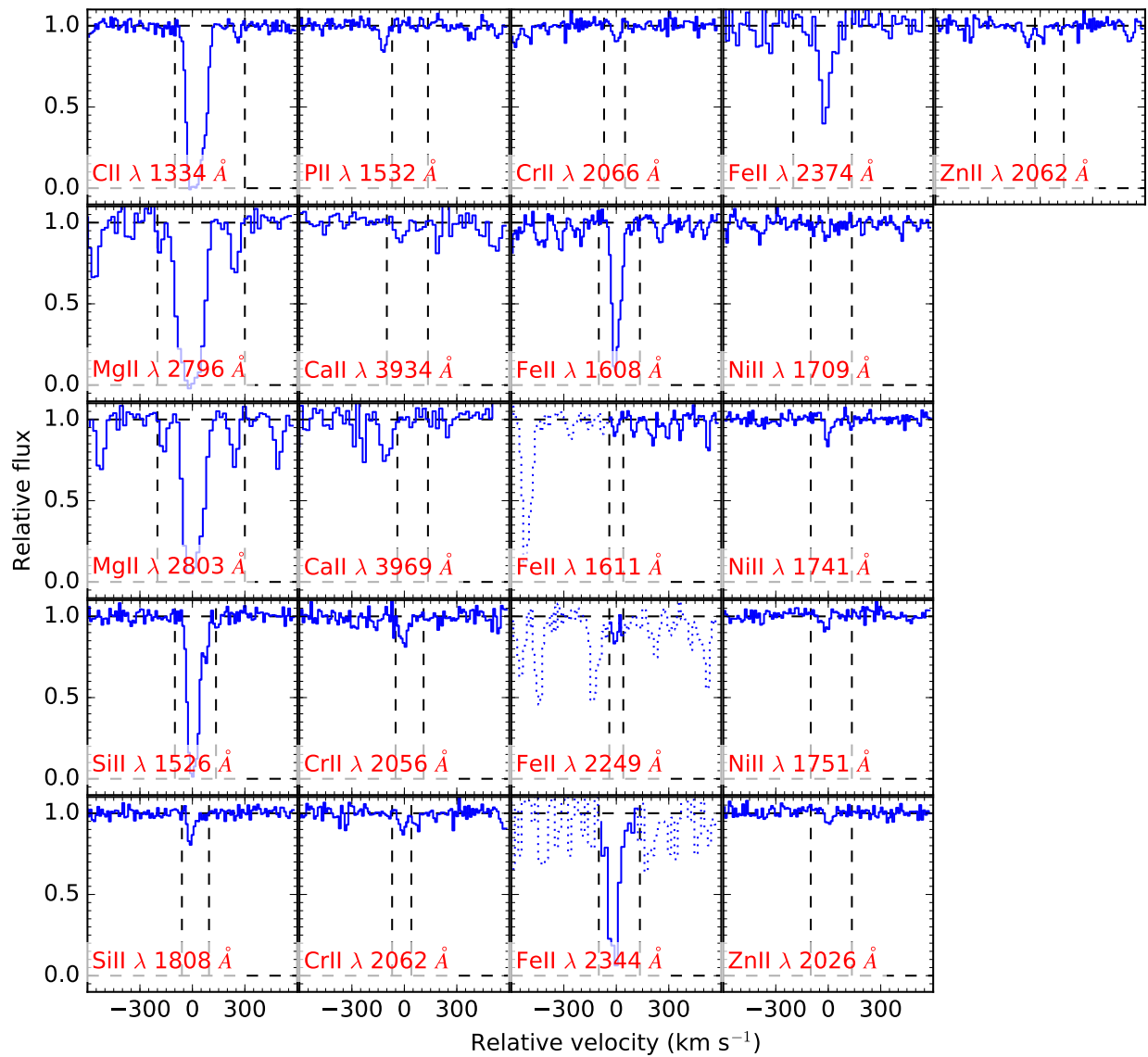


Figure A22. Velocity profile of the XQ100 spectrum towards J0818+0958 ($z_{\text{abs}}=3.306$).

Table A23. X-Shooter metal column densities for J0835+0650 ($z_{\text{abs}}=3.955$)

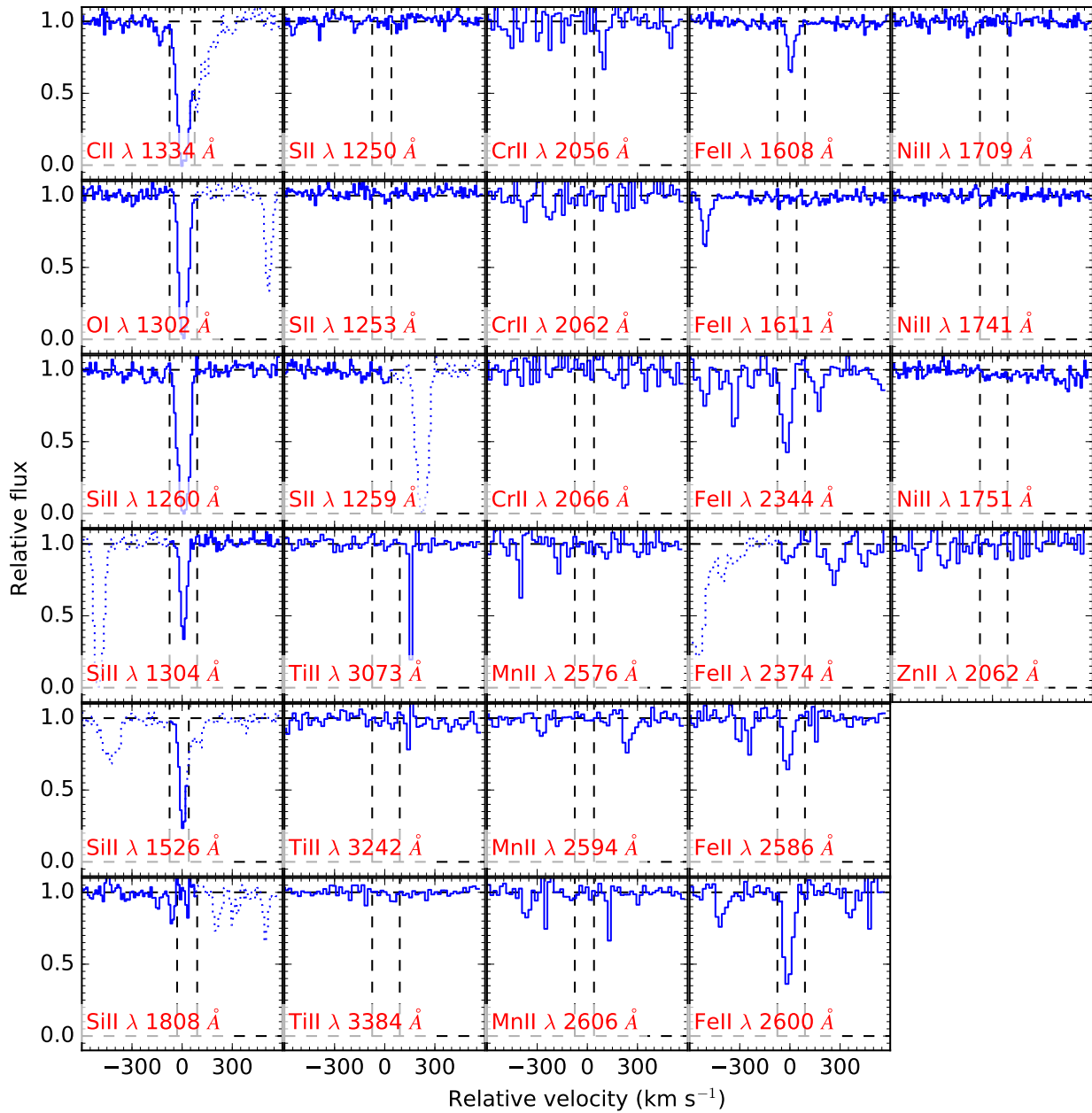


Figure A23. Velocity profile of the XQ100 spectrum towards J0835+0650 ($z_{\text{abs}}=3.955$).

Table A24. X-Shooter metal column densities for J0920+0725 ($z_{\text{abs}}=2.238$)

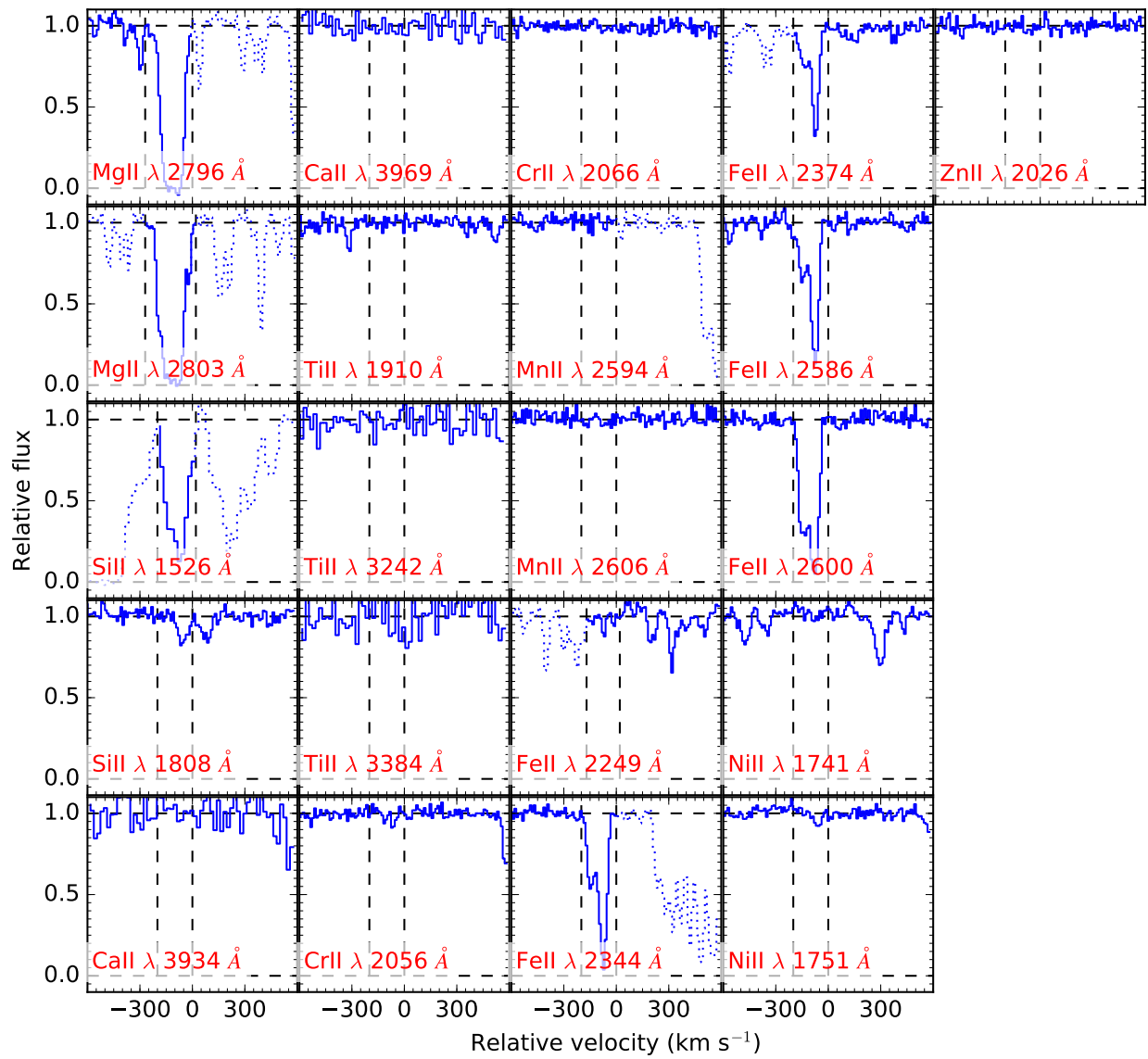


Figure A24. Velocity profile of the XQ100 spectrum towards J0920+0725 ($z_{\text{abs}}=2.238$).

Table A25. X-Shooter metal column densities for J0955–0130 ($z_{\text{abs}}=4.024$)

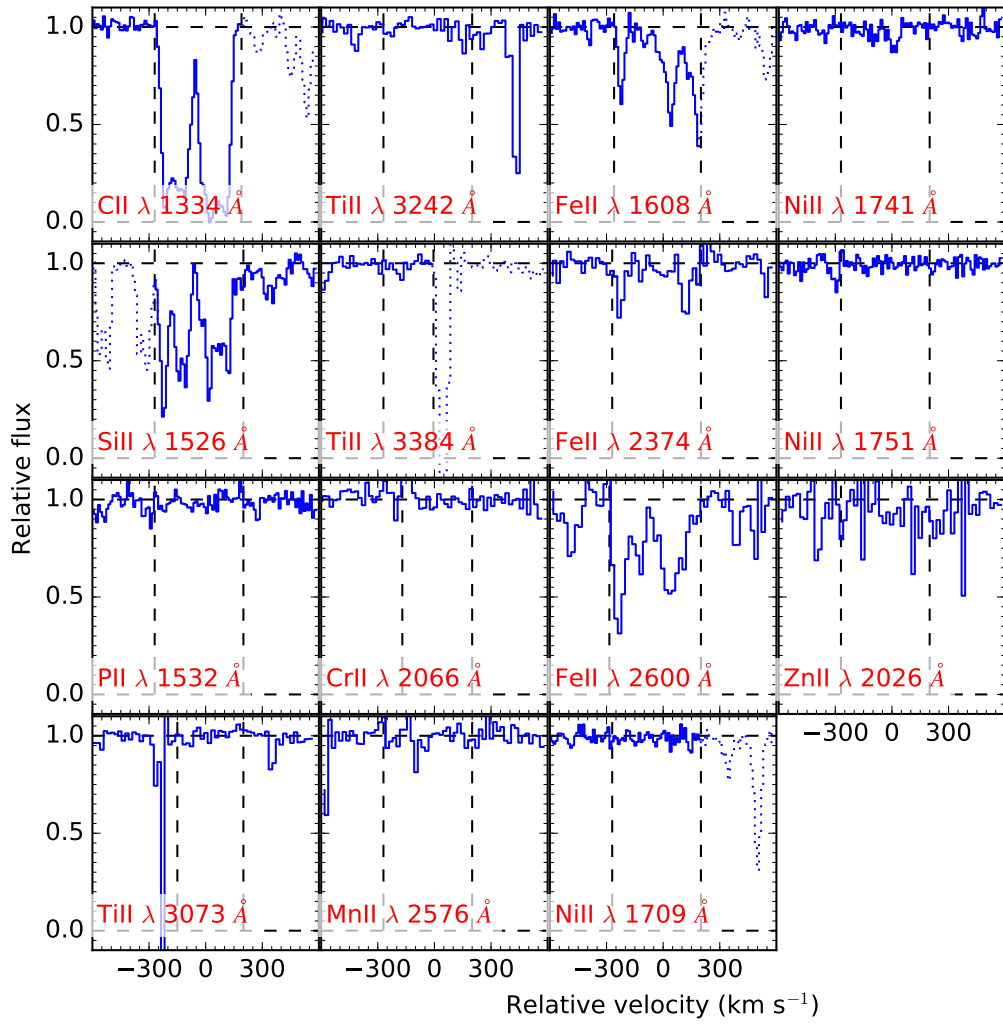


Figure A25. Velocity profile of the XQ100 spectrum towards J0955-0130 ($z_{\text{abs}}=4.024$).

Table A26. X-Shooter metal column densities for J1020+0922 ($z_{\text{abs}}=2.592$)

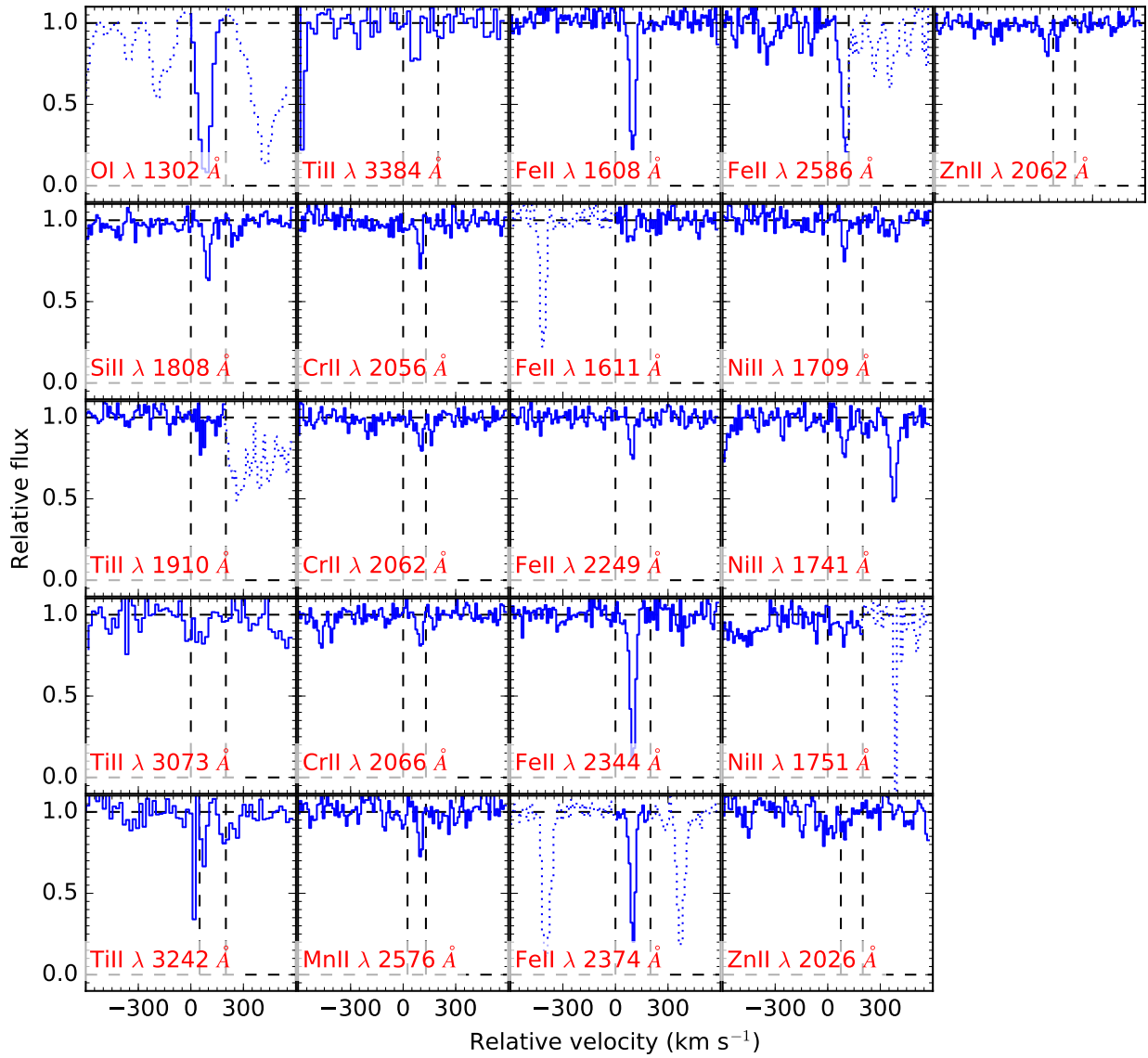


Figure A26. Velocity profile of the XQ100 spectrum towards J1020+0922 ($z_{\text{abs}}=2.592$).

Table A27. X-Shooter metal column densities for J1024+1819 ($z_{\text{abs}}=2.298$)

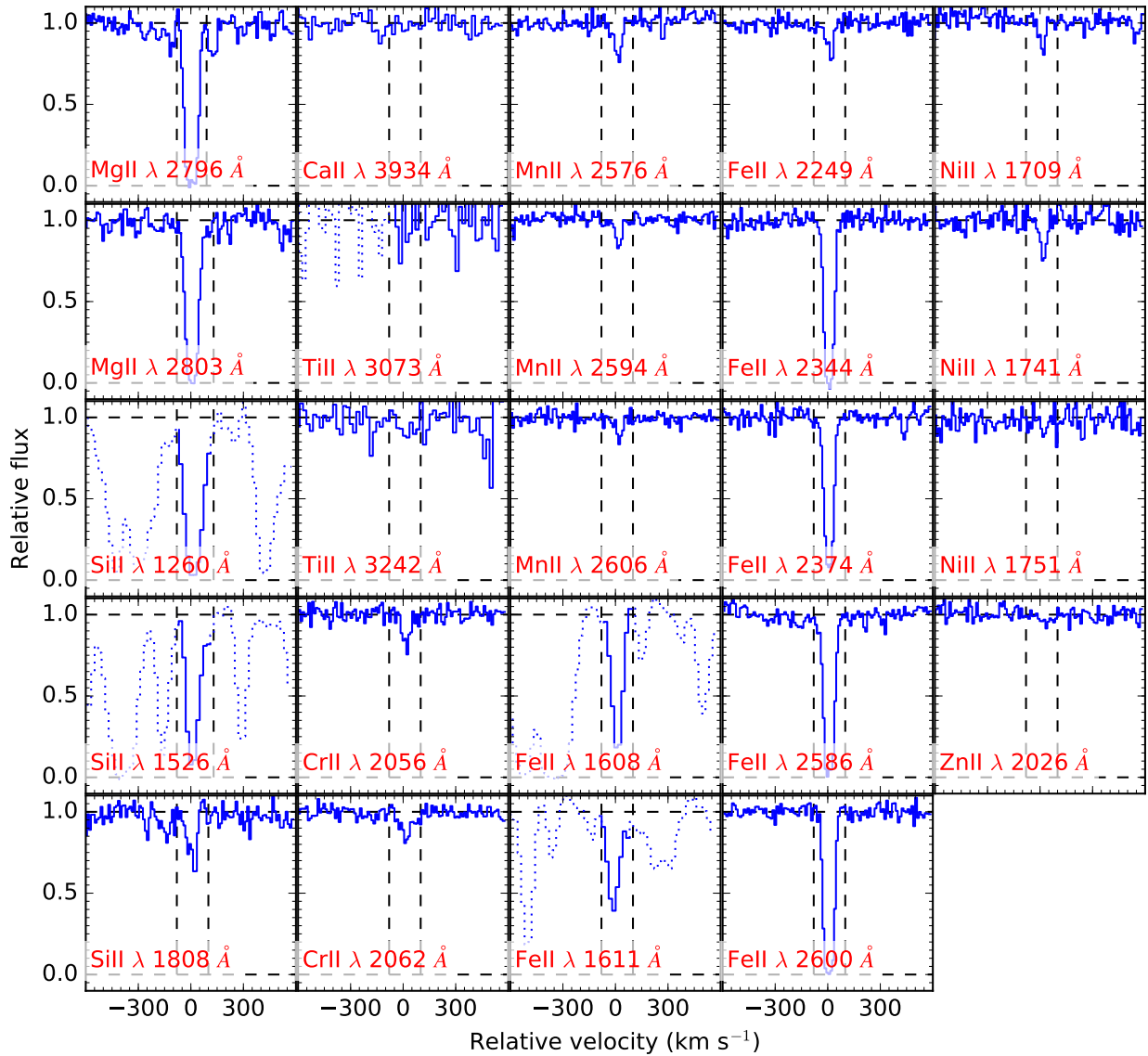


Figure A27. Velocity profile of the XQ100 spectrum towards J1024+1819 ($z_{\text{abs}}=2.298$).

Table A28. X-Shooter metal column densities for J1057+1910 ($z_{\text{abs}}=3.373$)

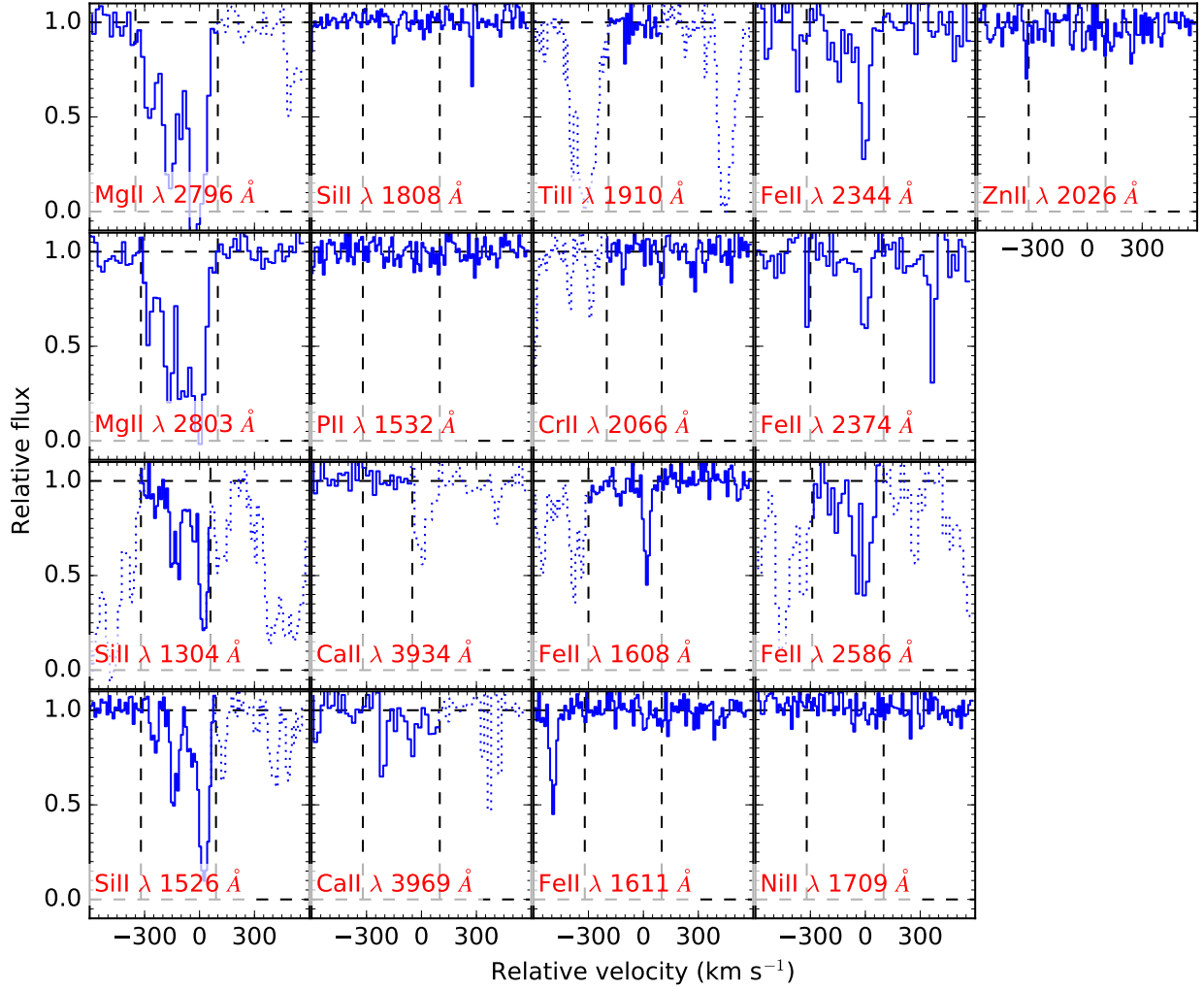


Figure A28. Velocity profile of the XQ100 spectrum towards J1057+1910 ($z_{\text{abs}}=3.373$).

Table A29. X-Shooter metal column densities for J1058+1245 ($z_{\text{abs}}=3.432$)

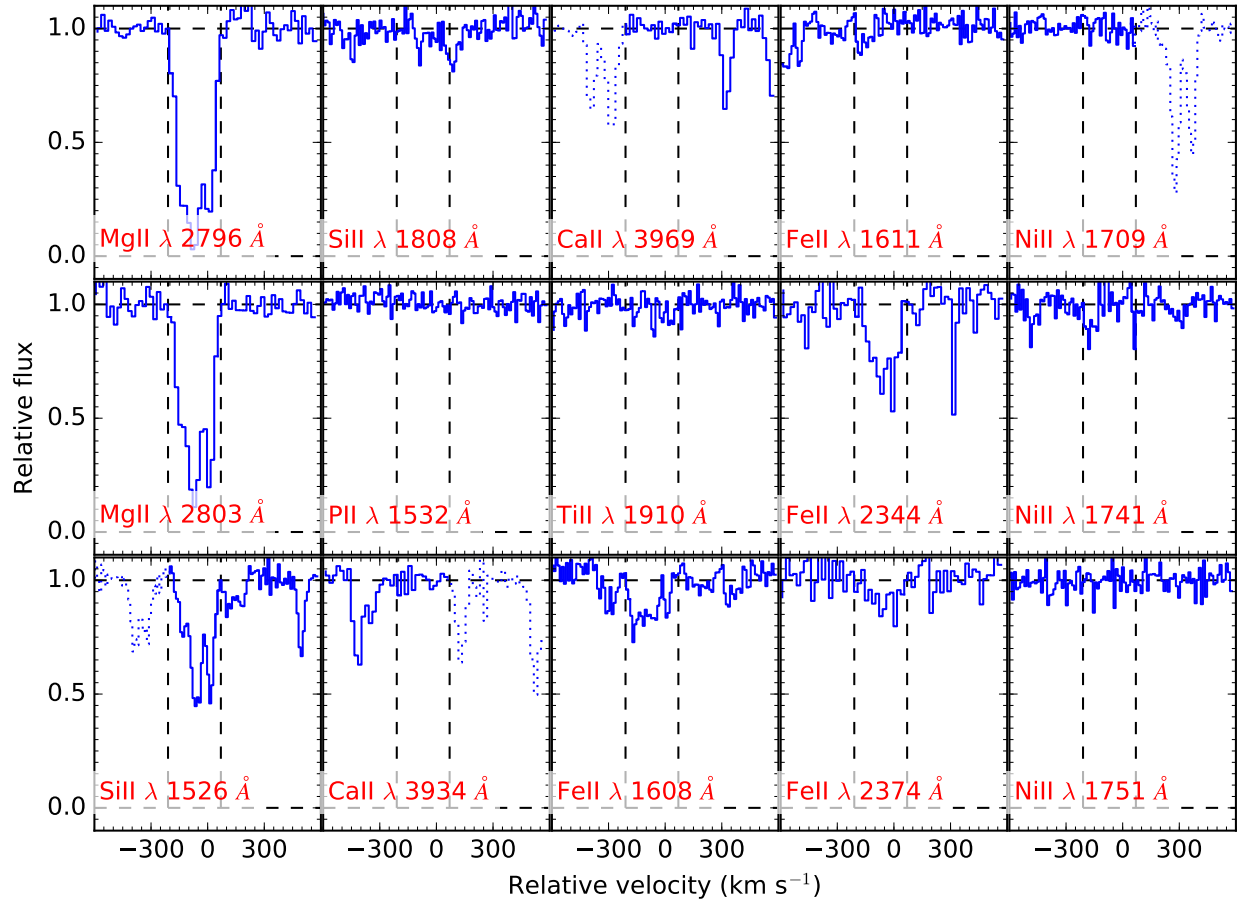


Figure A29. Velocity profile of the XQ100 spectrum towards J1058+1245 ($z_{\text{abs}}=3.432$).

Table A30. X-Shooter metal column densities for J1108+1209 ($z_{\text{abs}}=3.397$)

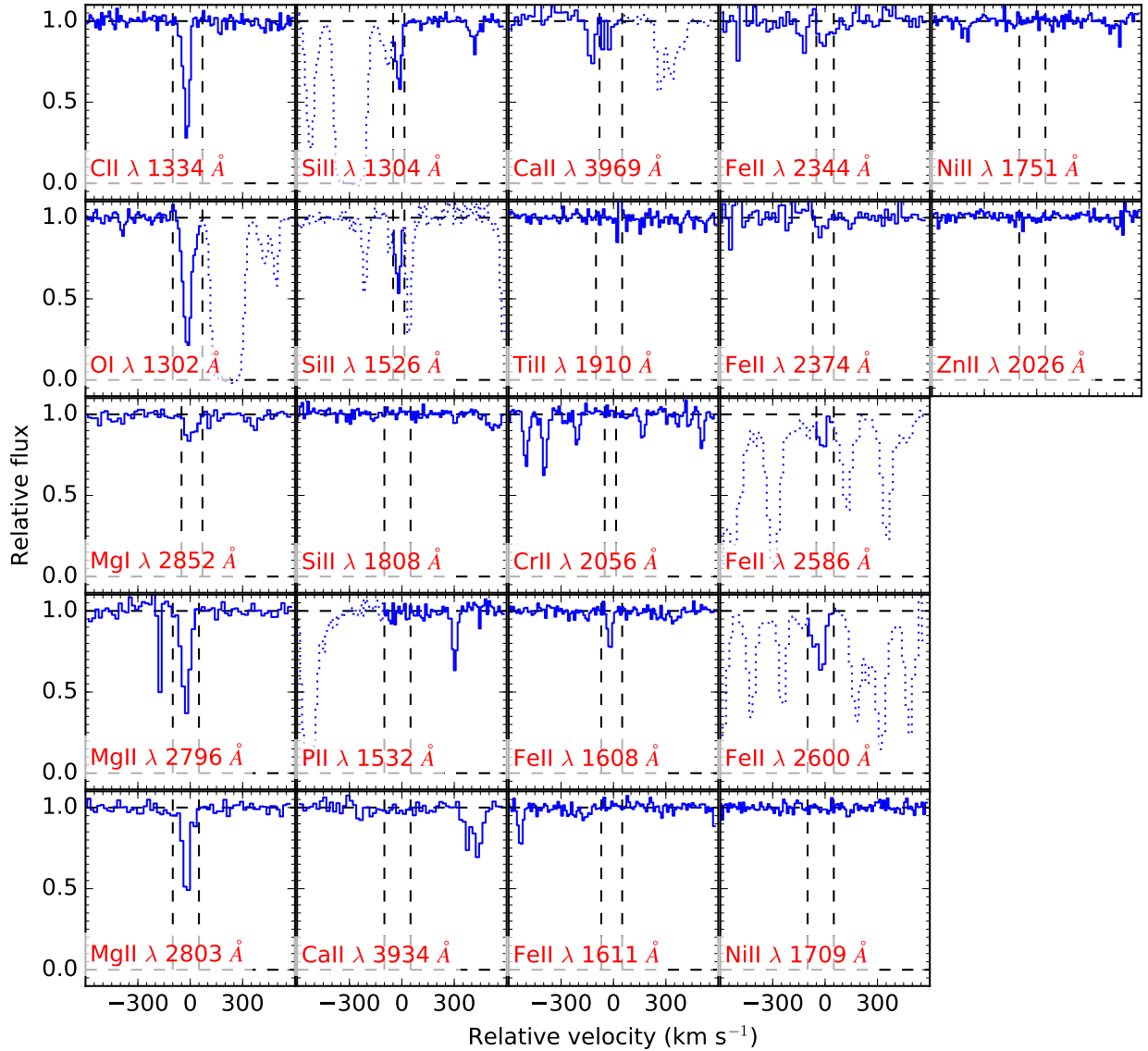


Figure A30. Velocity profile of the XQ100 spectrum towards J1108+1209 ($z_{\text{abs}}=3.397$).

Table A31. X-Shooter metal column densities for J1108+1209 ($z_{\text{abs}} = 3.546$)

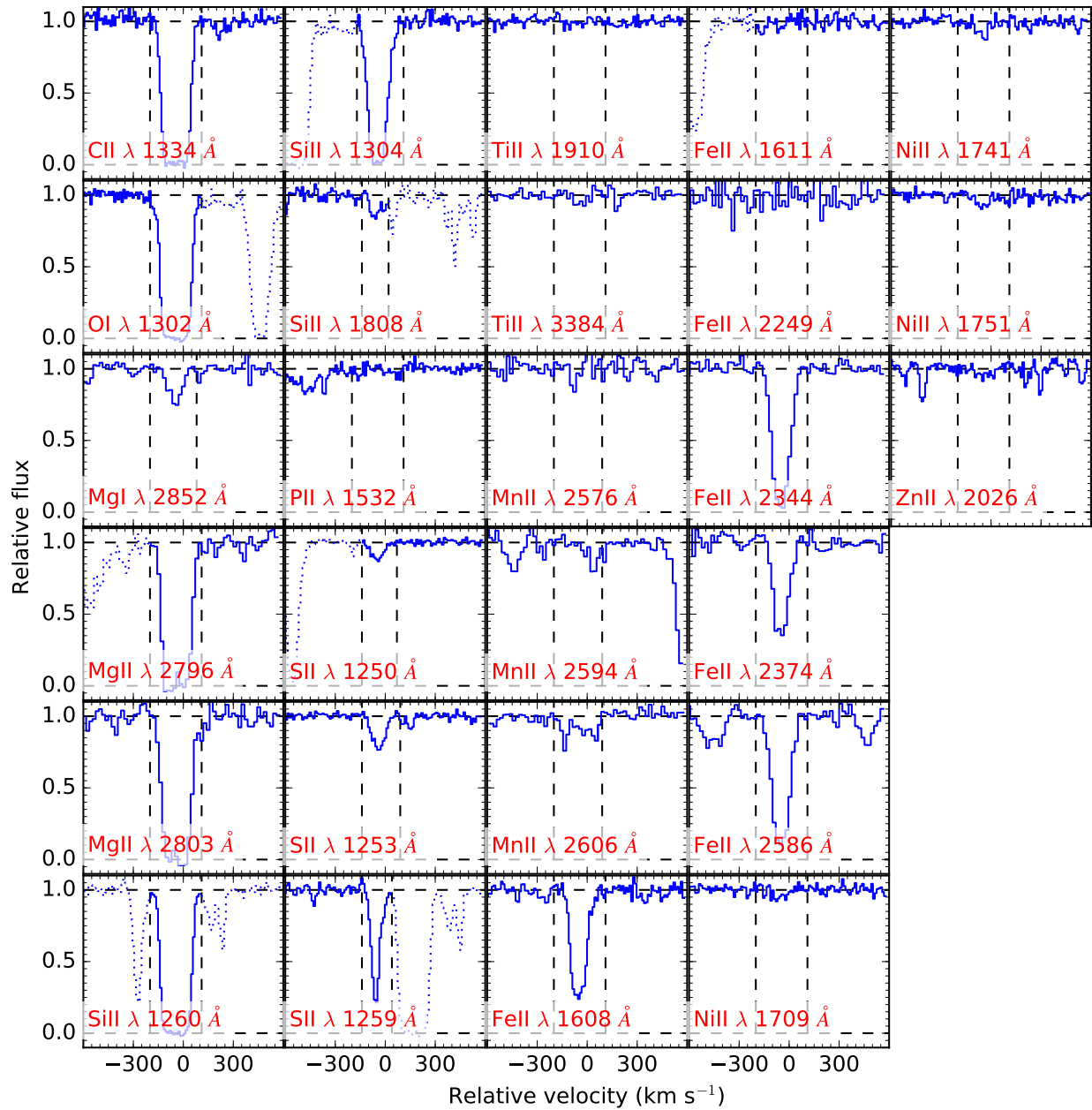


Figure A31. Velocity profile of the XQ100 spectrum towards J1108+1209 ($z_{\text{abs}}=3.546$).

Table A32. X-Shooter metal column densities for J1312+0841 ($z_{\text{abs}}=2.660$)

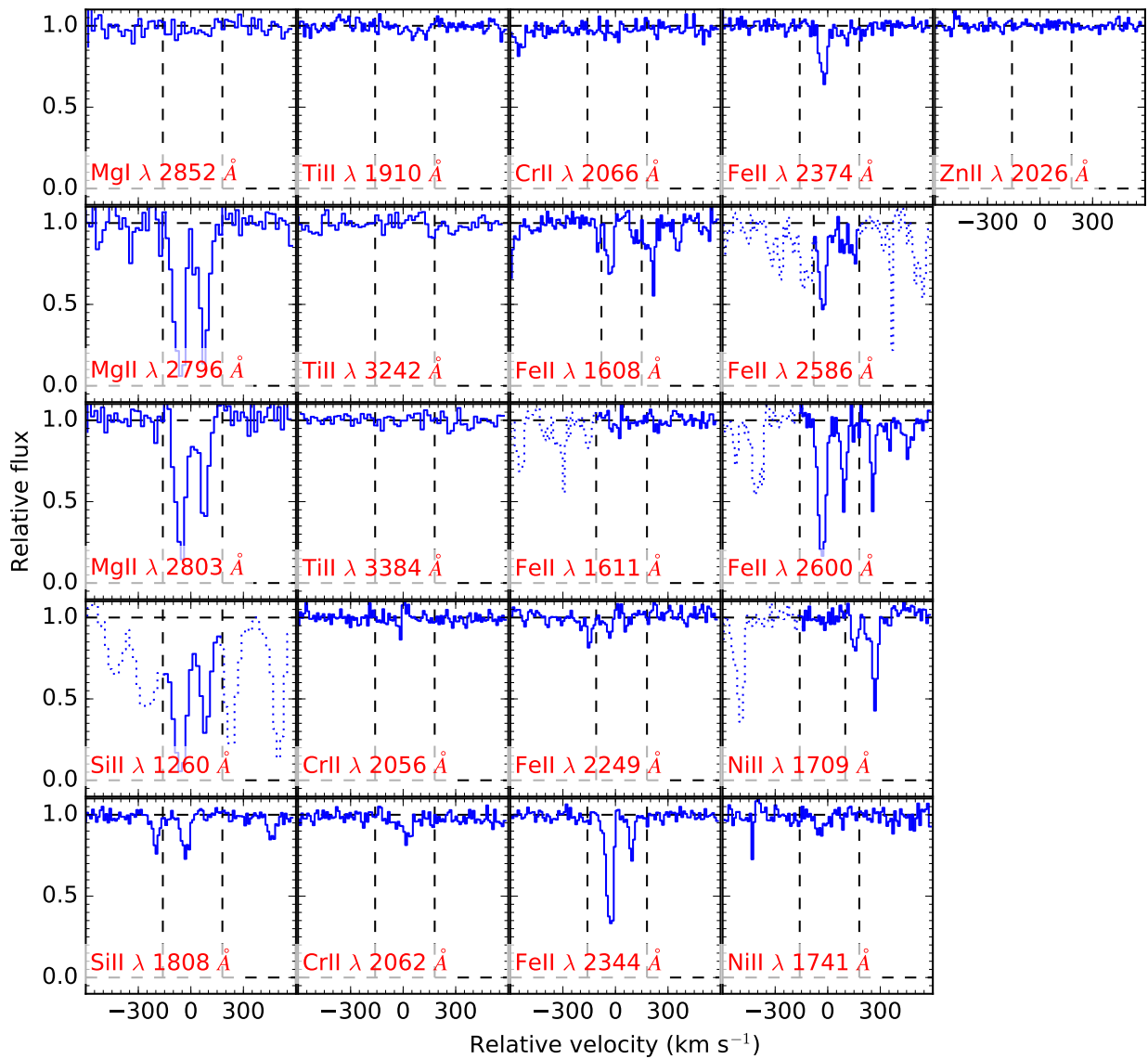


Figure A32. Velocity profile of the XQ100 spectrum towards J1312+0841 ($z_{\text{abs}}=2.660$).

Table A33. X-Shooter metal column densities for J1421–0643 ($z_{\text{abs}}=3.449$)

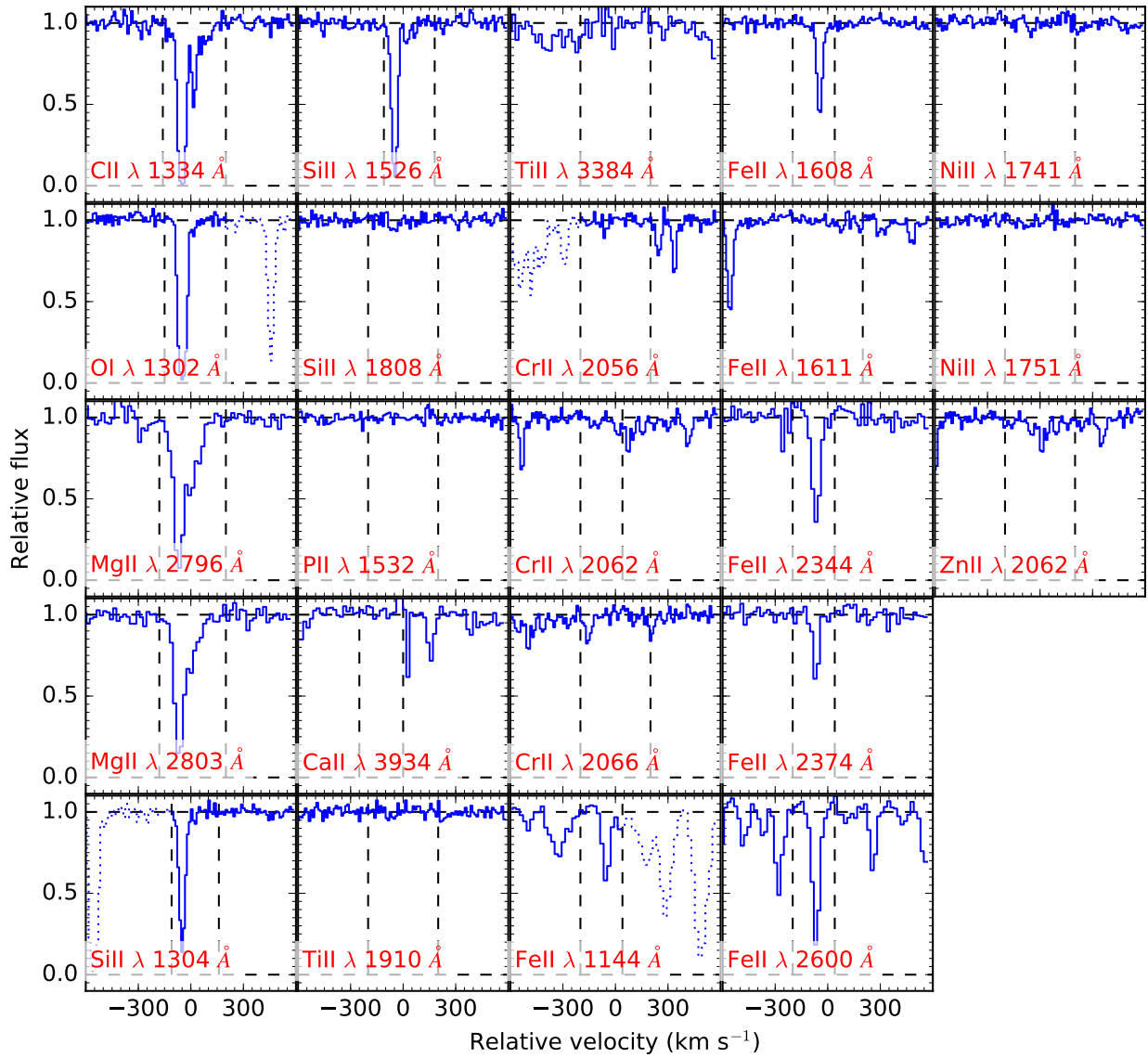


Figure A33. Velocity profile of the XQ100 spectrum towards J1421-0643 ($z_{\text{abs}}=3.449$).

Table A34. X-Shooter metal column densities for J1517+0511 ($z_{\text{abs}}=2.688$)

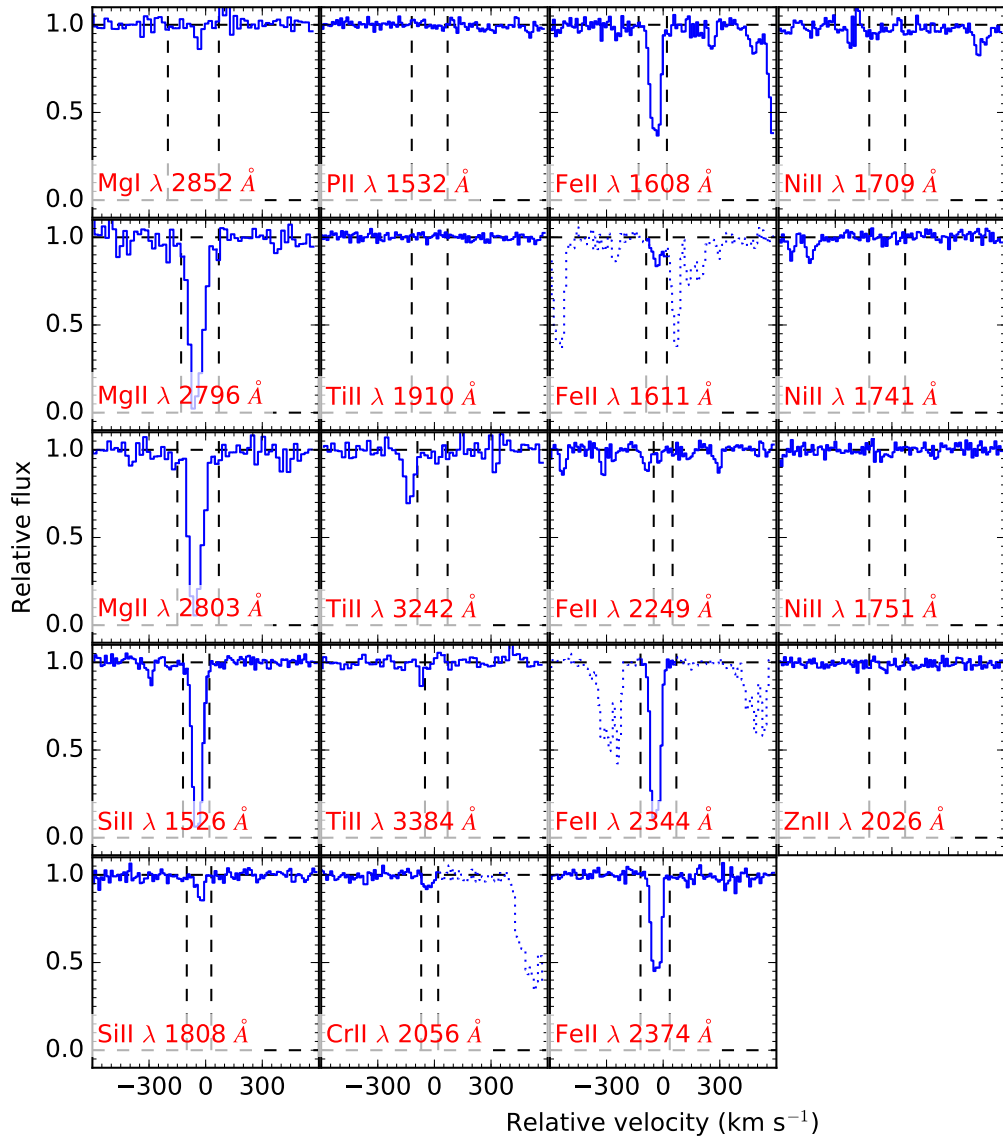


Figure A34. Velocity profile of the XQ100 spectrum towards J1517+0511 ($z_{\text{abs}}=2.688$).

Table A35. X-Shooter metal column densities for J1552+1005 ($z_{\text{abs}}=3.601$)

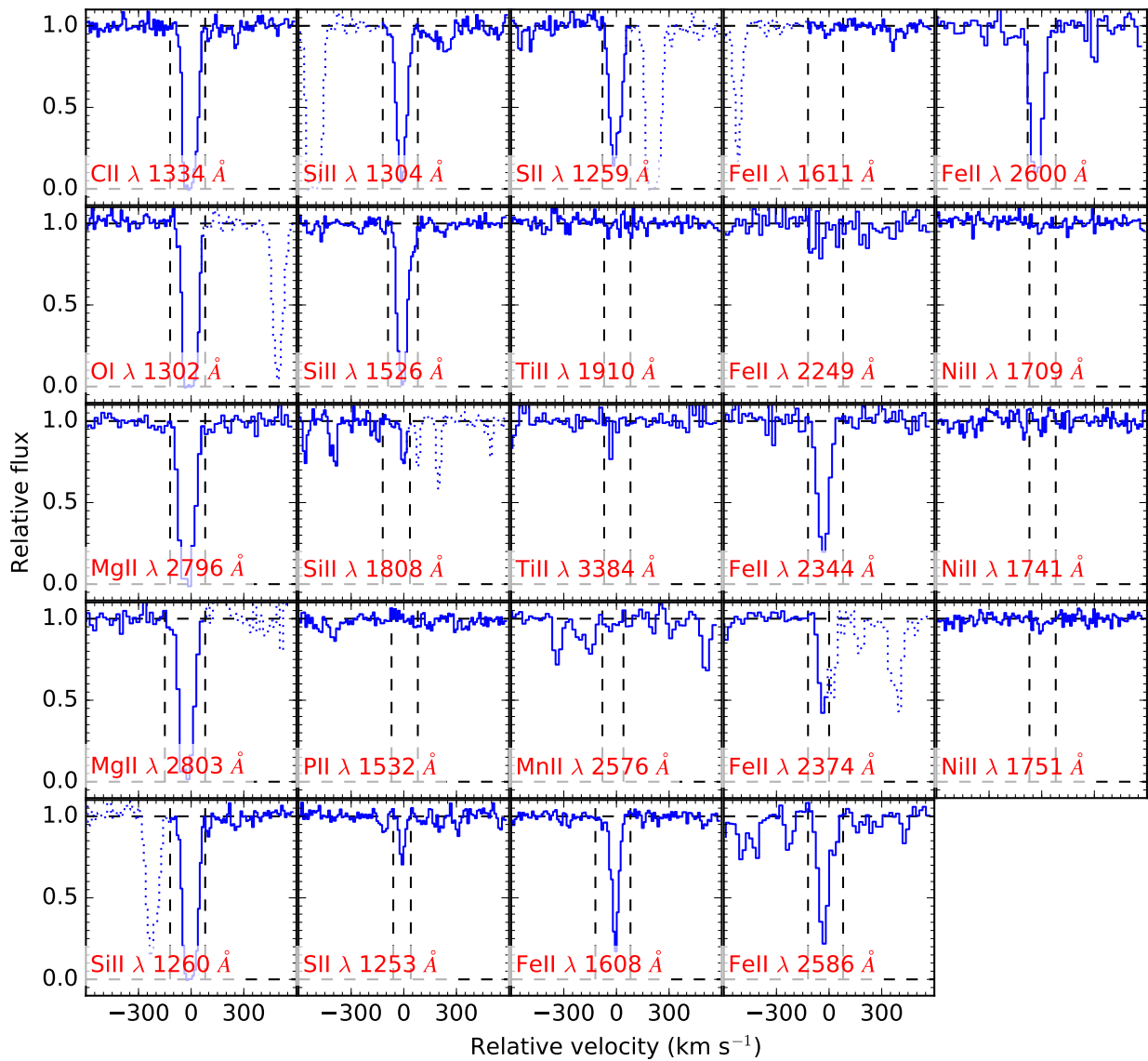


Figure A35. Velocity profile of the XQ100 spectrum towards J1552+1005 ($z_{\text{abs}}=3.601$).

Table A36. X-Shooter metal column densities for J1552+1005 ($z_{\text{abs}}=3.667$)

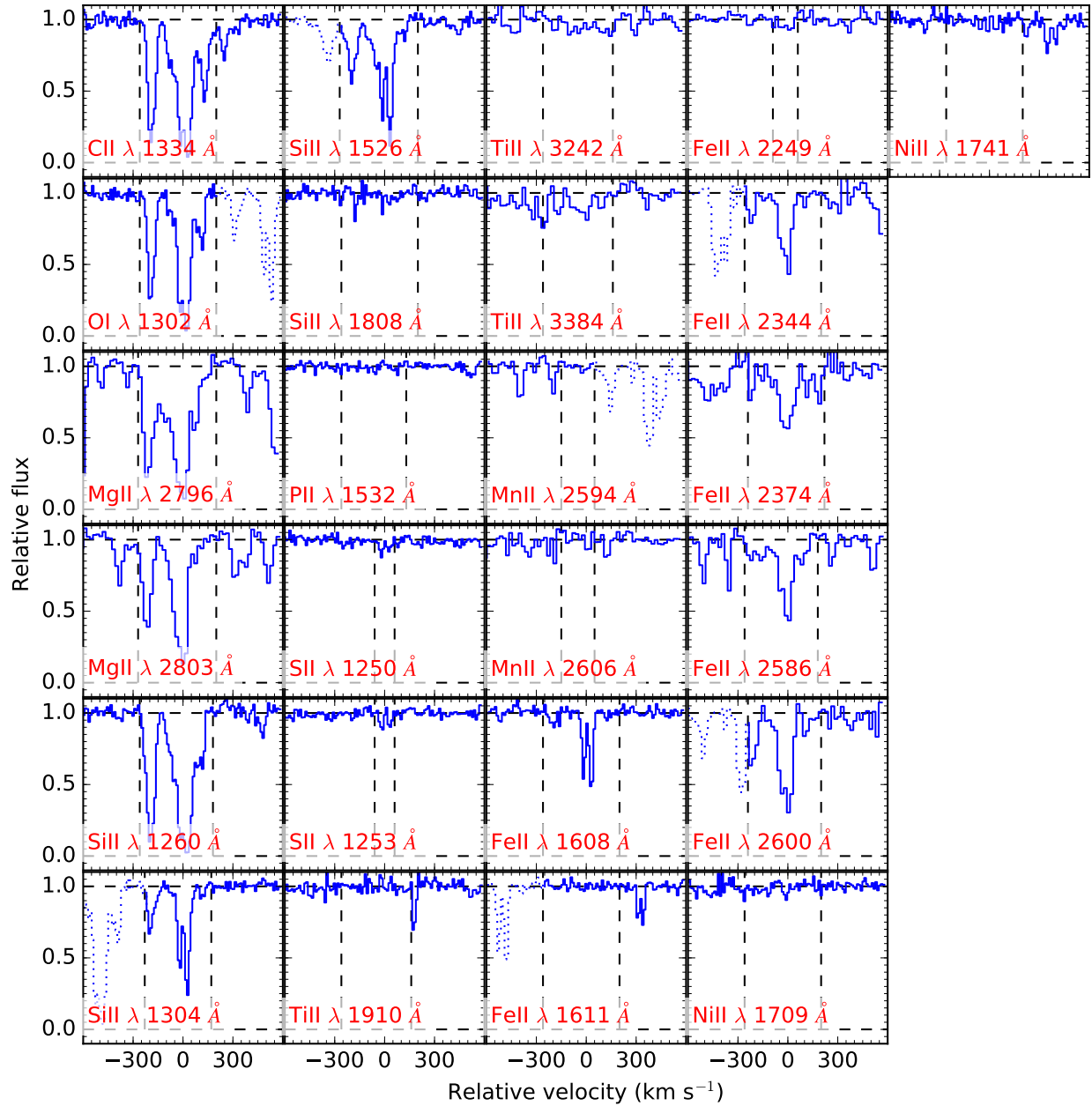


Figure A36. Velocity profile of the XQ100 spectrum towards J1552+1005 ($z_{\text{abs}}=3.667$).

Table A37. X-Shooter metal column densities for J1633+1411 ($z_{\text{abs}}=2.882$)

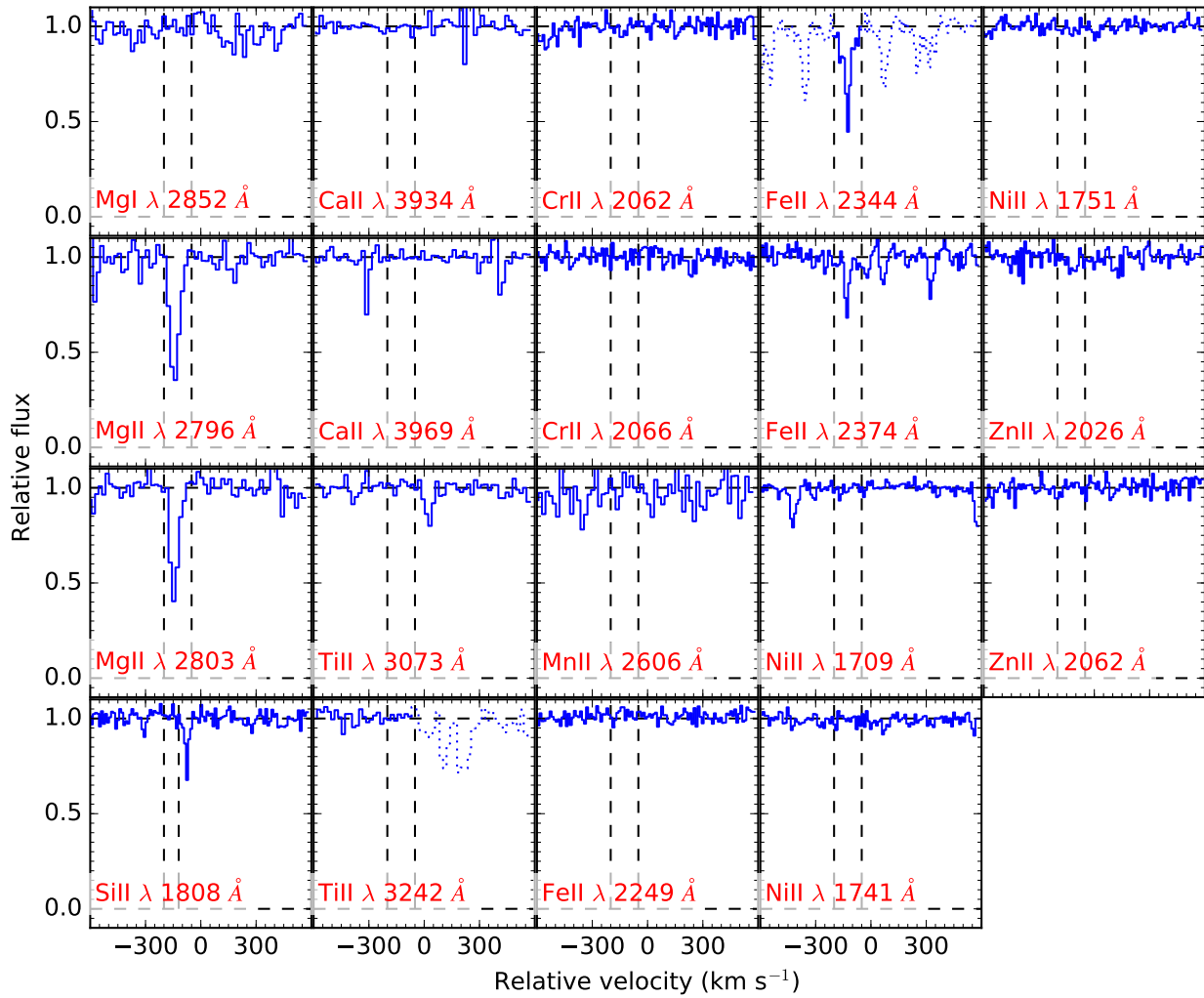


Figure A37. Velocity profile of the XQ100 spectrum towards J1633+1411 ($z_{\text{abs}}=2.882$).

Table A38. X-Shooter metal column densities for J1723+2243 ($z_{\text{abs}} = 3.698$)

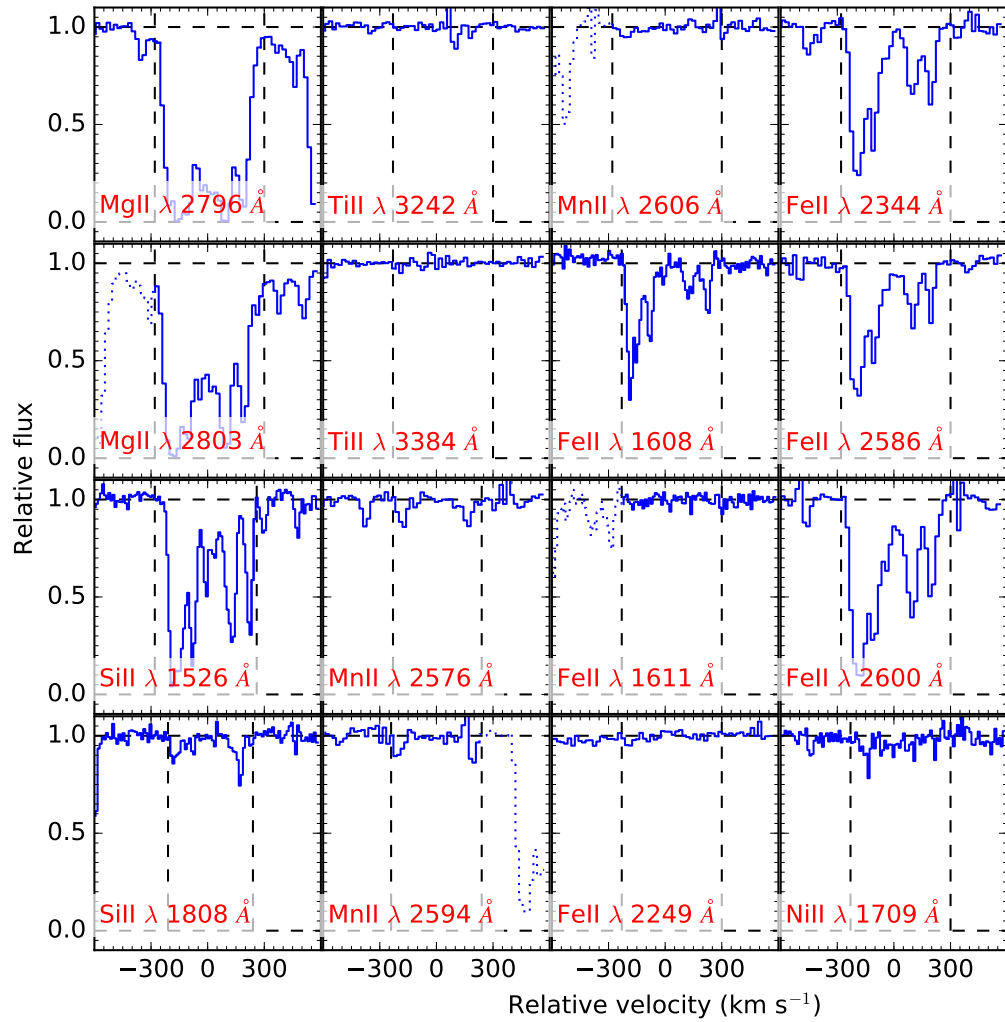


Figure A38. Velocity profile of the XQ100 spectrum towards J1723+2243 ($z_{\text{abs}}=3.698$).

Table A39. X-Shooter metal column densities for J2239–0552 ($z_{\text{abs}}=4.080$)

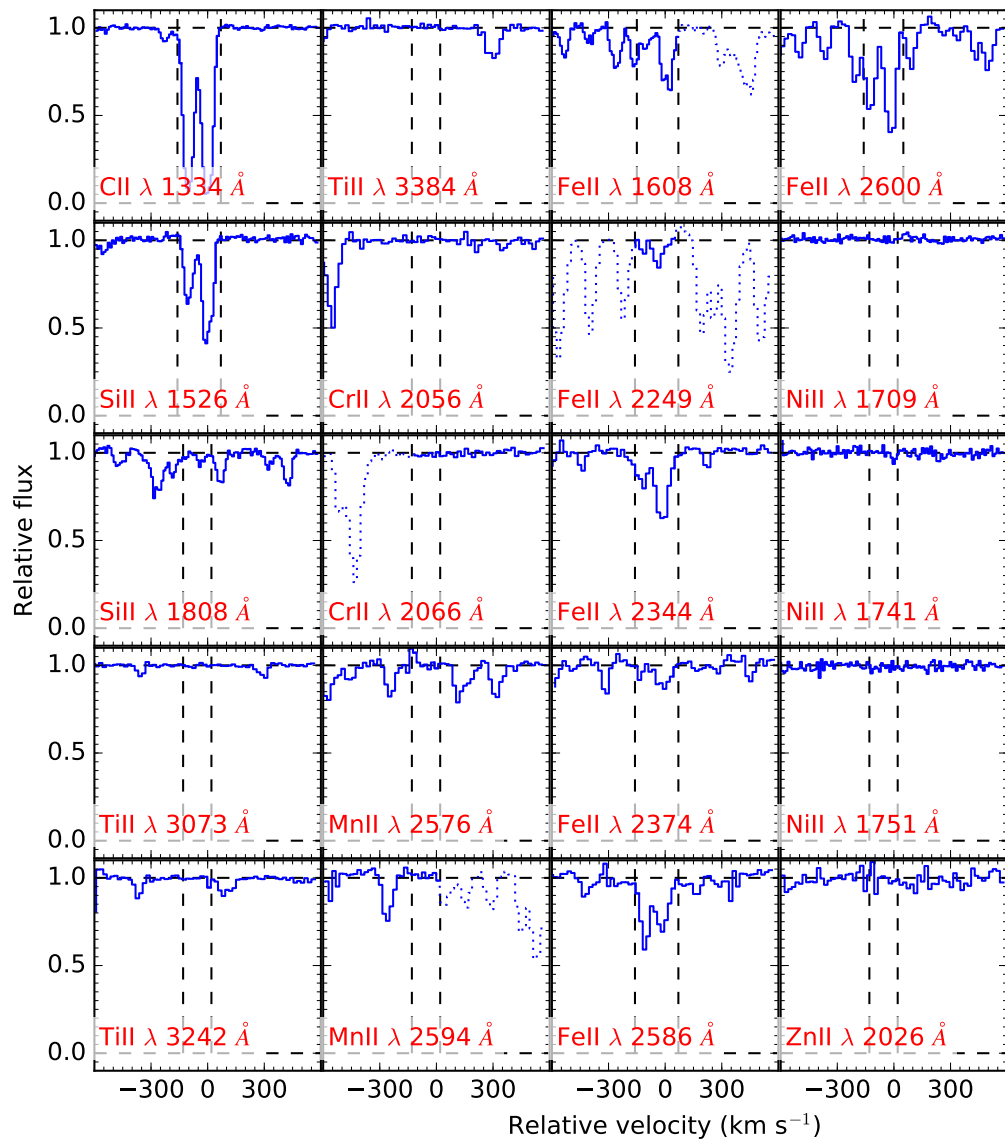


Figure A39. Velocity profile of the XQ100 spectrum towards J2239-0552 ($z_{\text{abs}}=4.080$).

Table A40. X-Shooter metal column densities for J2344+0342 ($z_{\text{abs}}=3.220$)

Ion	Line	λ Å	f	v_{min} km s $^{-1}$	v_{max} km s $^{-1}$	logN(X)	Included	logN $_{\text{adopt}}$
MgI	2852	2852.964	1.81E+00	-70	80	12.56 ± 0.01	Y	—
MgI								12.56 ± 0.05
MgII	2796	2796.352	6.12E-01	-210	205	> 13.74	N	—
MgII	2803	2803.531	3.05E-01	-170	205	> 14.18	Y	—
MgII								> 14.18
CaII	3934	3934.777	6.50E-01	-90	90	< 11.78	Y	—
CaII	3969	3969.591	3.22E-01	-90	90	< 12.07	N	—
CaII								< 11.78
TiII	1910	1910.750	2.02E-01	-90	90	< 12.53	Y	—
TiII	3073	3073.877	1.09E-01	-90	90	< 12.97	Y	—
TiII								< 12.53
CrII	2056	2056.254	1.05E-01	-70	90	13.38 ± 0.03	Y	—
CrII	2062	2062.234	7.80E-02	-70	90	< 13.28	Y	—
CrII	2066	2066.161	5.15E-02	-70	90	< 13.29	Y	—
CrII								13.38 ± 0.05
MnII	2576	2576.877	3.51E-01	-90	40	12.69 ± 0.05	Y	—
MnII	2594	2594.499	2.71E-01	-90	60	12.88 ± 0.05	Y	—
MnII	2606	2606.462	1.93E-01	-90	90	13.05 ± 0.04	N	—
MnII								12.79 ± 0.07
FeII	1608	1608.451	5.80E-02	-90	90	> 14.76	Y	—
FeII	1611	1611.200	1.36E-03	-90	90	< 15.29	Y	—
FeII	2374	2374.461	3.13E-02	-90	90	> 14.62	N	—
FeII	2586	2586.650	6.91E-02	-90	90	> 14.55	N	—
FeII	2600	2600.173	2.39E-01	-90	90	> 14.33	N	—
FeII								$14.75-15.29$
NiII	1709	1709.604	3.24E-02	-90	90	13.70 ± 0.05	Y	—
NiII	1741	1741.553	4.27E-02	-90	90	13.81 ± 0.03	Y	—
NiII	1751	1751.916	2.77E-02	-90	90	13.65 ± 0.06	Y	—
NiII								13.76 ± 0.08
ZnII	2026	2026.136	4.89E-01	-90	90	12.27 ± 0.08	N	—
ZnII	2062	2062.664	2.56E-01	-90	90	< 12.85	Y	—
ZnII								< 12.85

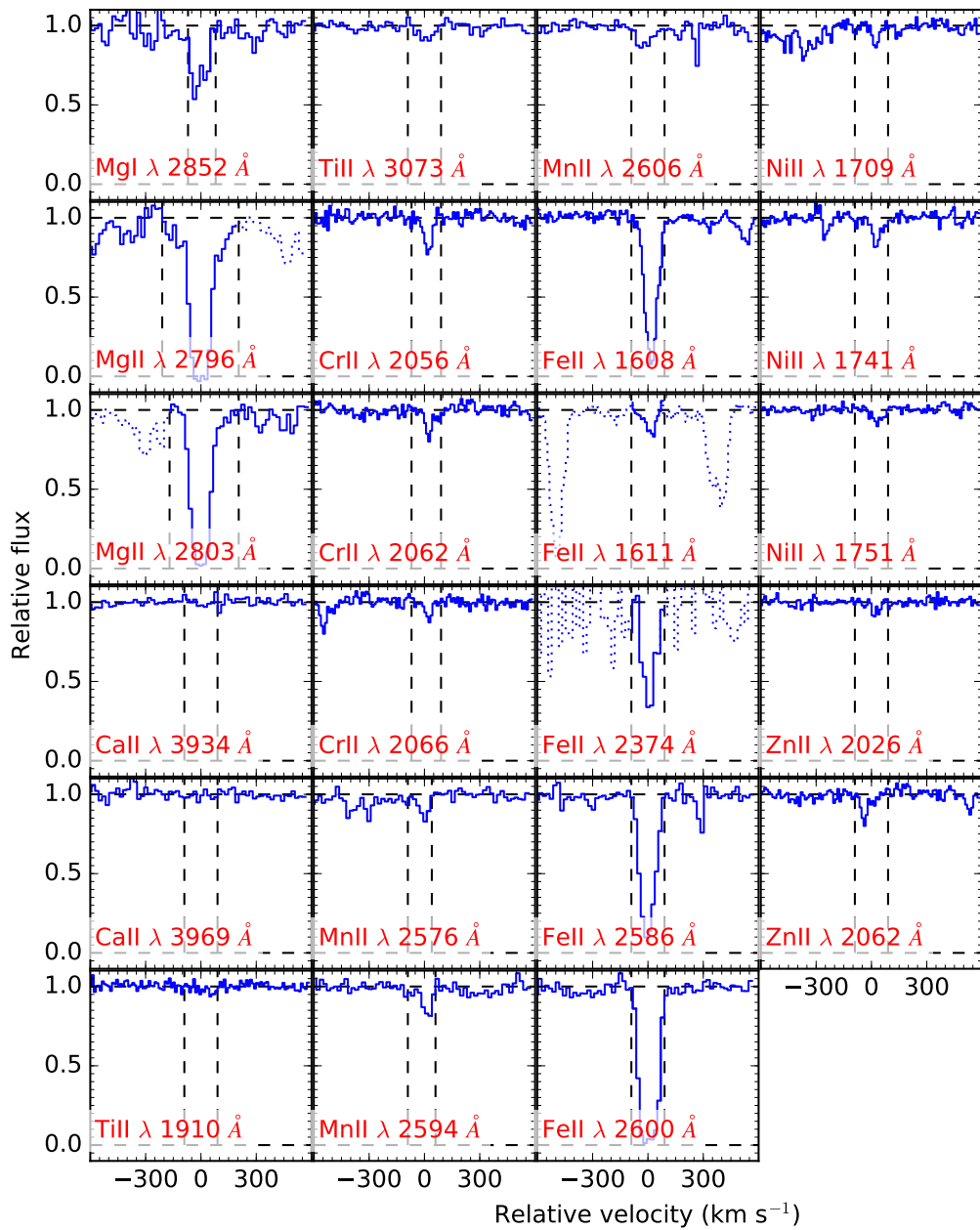


Figure A40. Velocity profile of the XQ100 spectrum towards J2344+0342 ($z_{\text{abs}}=3.220$).

A2 UVES data J0034+1639

APPENDIX B: ABUNDANCE DISCREPANCIES FROM LITERATURE

J0003–2603 ($z_{\text{abs}} = 3.39$)

The FeII literature column density was taken from Molaro et al. (2000). The discrepancy with the XQ-100 derived column density of 0.12 dex is the result of a difference in the adopted oscillator strengths. Molaro et al. (2000) uses an FeII 1611 Å oscillator strength 33% higher than the value adopted from Morton (2003); matching the size of the discrepancy in column densities. We continue using the XQ-100 column density as the adopted value.

J0134+0400 ($z_{\text{abs}} = 3.77$)

The literature data is primarily taken from Prochaska et al. (2003), and was obtained with ESI. Both the literature and XQ-100 spectra show SiIII 1808 lines free from contamination, and provide abundances that are consistent with a saturated SiIII 1526 lines. We suspect that our SiIII 1808 measurement is more reliable as it reproduces the same velocity profile of other metal lines, whereas there appears to be an additional blue component ($\sim -75 \text{ km s}^{-1}$) in the Prochaska et al. (2003) profile.

The 0.14 dex discrepancy in the $\log N(\text{NIII})$ is likely due to inaccurate oscillator strengths of many NiIII lines (e.g. Jenkins & Tripp 2006). Prochaska et al. (2003) use the NiIII 1370Å line, whereas our value uses a combination of NiIII 1741 and 1751 Å lines. Given that adopted NiIII 1370Å line from Prochaska et al. (2003) is also similarly higher (~ 0.12 dex) than from Morton (2003, our source of oscillator strengths), we believe accounting for this discrepancy in oscillator strengths would place the two column densities in agreement. We continue to adopt the XQ-100 derived column density.

J0255+0048 ($z_{\text{abs}} = 3.25$ and 3.91)

For both DLAs towards J0255+0048, we find discrepant NiIII from the values derived in Prochaska et al. (2001). For the DLA at $z_{\text{abs}} = 3.25$, Prochaska et al. (2001) claim a detection of the NiIII 1709 line, whereas we do not see any significant absorption in the XQ-100 spectra for the NiIII 1709 line. As our 3σ limit in column density is consistent with the detection by Prochaska et al. (2001), it is unclear whether the NiIII 1709 line is actually detected. We therefore conservatively adopt our $\log N(\text{NiIII})$ limit.

The large discrepancy in the $\log N(\text{NiIII})$ in the DLA at $z_{\text{abs}} = 3.91$ is likely due to inaccurate oscillator strengths of many NiIII lines. For the NiIII 1709, 1741, and 1751 lines; the oscillator strengths adopted in both works agree. However for NiIII 1317 and 1370, the oscillator strengths adopted in Prochaska et al. (2001) are ~ 0.15 dex higher than ours. Accounting for this discrepancy in oscillator strength, our derived column density would be consistent with that measured by Prochaska et al. (2001). Jenkins & Tripp (2006) focused on independently measuring the oscillator strengths of Ni. The oscillator strengths from Morton (2003) (which we adopt) are consistent with those measured by Jenkins &

Tripp (2006). We therefore adopt the XQ-100 column densities.

J1421–0643 ($z_{\text{abs}} = 3.45$)

The FeII abundance was taken from Akerman et al. (2005), and is 0.09 dex higher than what we have measured. The discrepancy in column density is driven by the inclusion of the FeII 1144Å and 2374Å lines in the XQ-100 value, as the lower FeII 1608Å column density agrees with the measured value of the 1608Å line from the literature (Akerman 2005; Akerman et al. 2005). As multiple FeII lines should provide a better estimate of the true column density, we continue to use the XQ-100 adopted column density.

Table A41. UVES metal column densities for J0034+1639 ($z_{\text{abs}} = 3.752$)

Table A42. UVES metal column densities for J0034+1639 ($z_{\text{abs}}=4.283$)

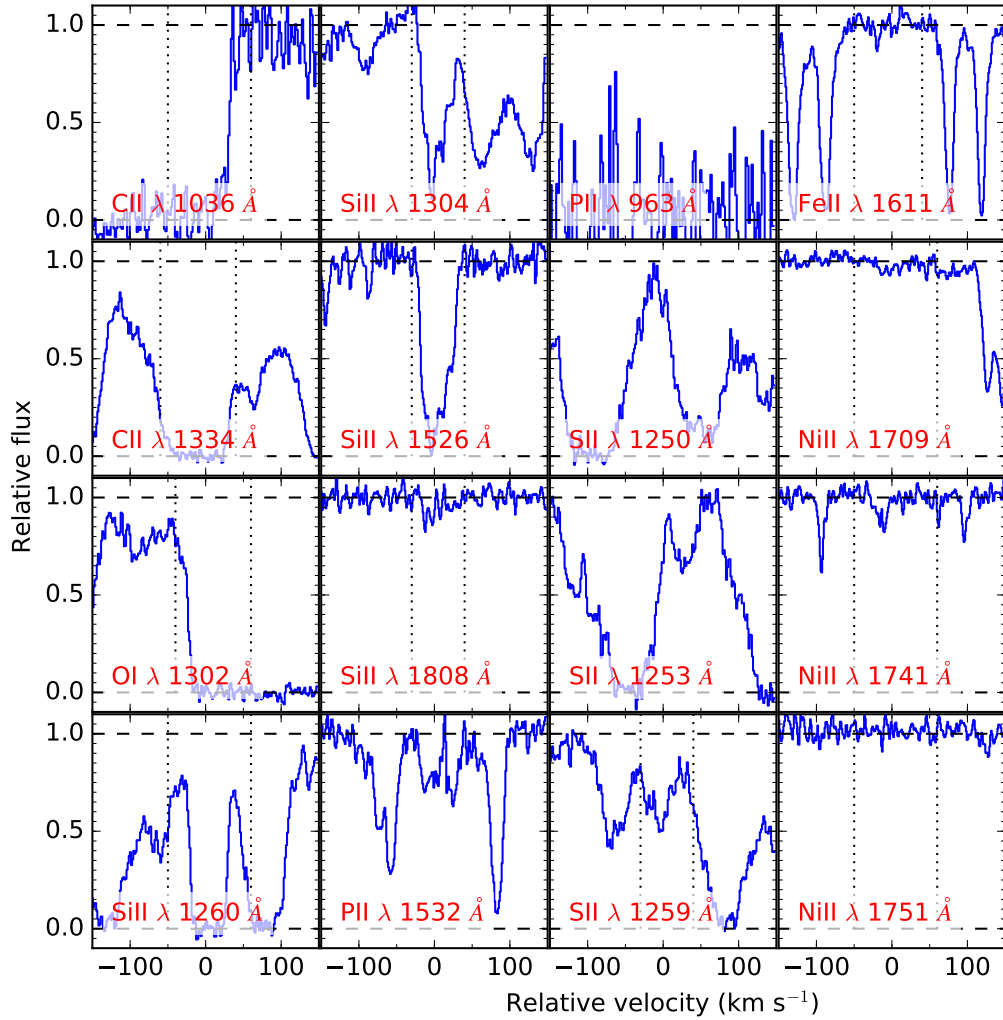


Figure A41. Velocity profile of the UVES spectrum towards J0034+1639 ($z_{\text{abs}}=3.752$).

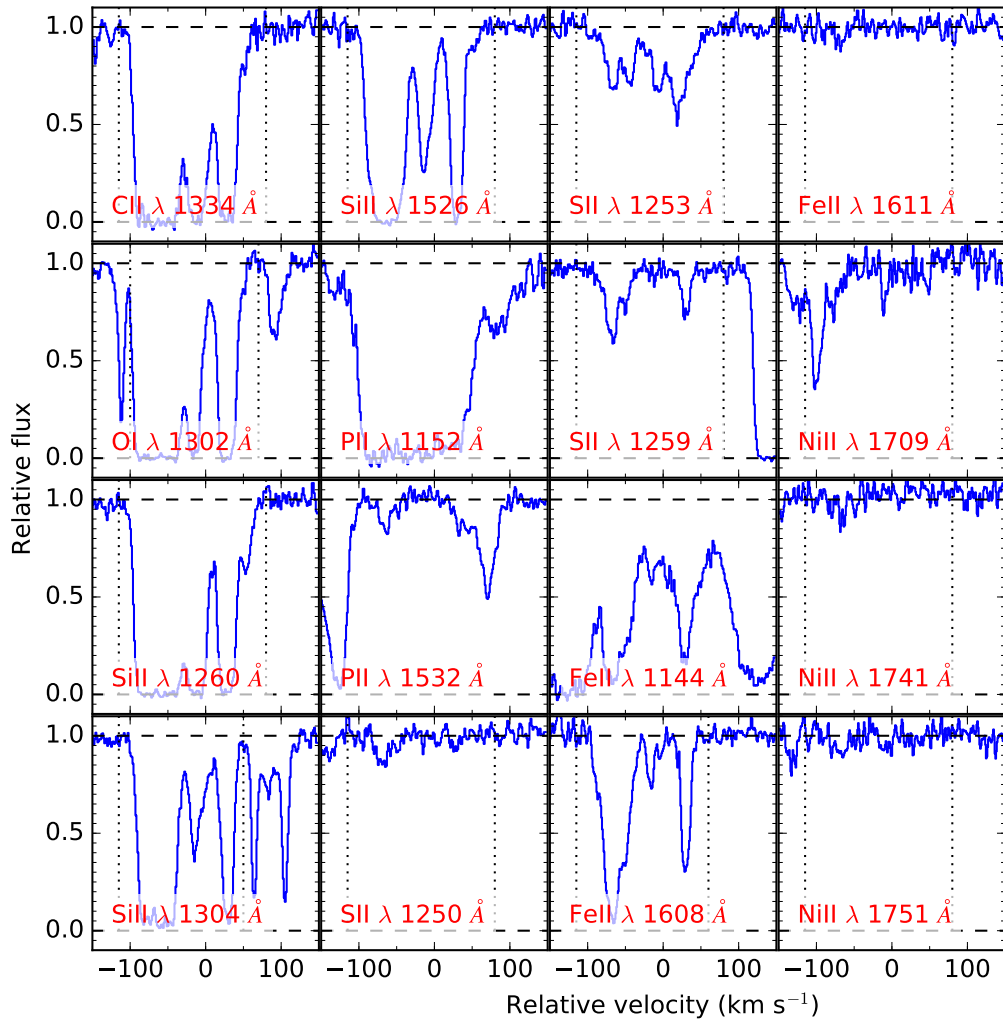


Figure A42. Velocity profile of the UVES spectrum towards J0034+1639 ($z_{\text{abs}}=4.282$).